Supramolecular organisation, assembly, and regulation of cyanobacterial thylakoid membrane

Zimeng Zhang

This thesis is submitted for the degree of Doctor of Philosophy

June 2021

Declaration

This thesis results from my own work and includes nothing that is the outcome of work done in collaboration except as declared in the preface and specified in the text.

It is not substantially the same as any work that has already been submitted before for any degree or other qualification except as declared in the preface and specified in the text.

The data in Chapter Three, "Characterising the supercomplex association of photosynthetic complexes in cyanobacteria", was included in a published paper (Zhang et al., 2021). The data in Chapter Four is unpublished. The work in Chapter Five, "Roles of Curvature Thylakoid 1 protein in mediating thylakoid membrane structure and photosynthetic function", will make up a future manuscript.

I acknowledge the contributions from the following collaborators to the results described in this thesis.

Dr Catarina Franco	Mass spectrometry of pull-down samples in Chapter 3
Dr Longsheng Zhao	Atomic force microscopy imaging of thylakoid membrane complexes (Figure 3-3AB, Figure 3-8EFGH, Figure 3-9B)
Mr Gregory Dykes	Transmission electron microscopy imaging of cyanobacterial cells (Figure 5-5A)
Dr Tuomas Huokko	Confocal microscopy imaging of cyanobacterial cells (Figure 5-7A, Figure 5-8A)
Prof Yin Chen	Lipid mass spectrometry (Figure 5-9)
Dr Gareth Wright	Instructions for protein crystallography and high-performance liquid chromatography (Figure 5-10B)

This thesis is submitted in accordance with the requirements of the University of Liverpool for the degree of Doctor in Philosophy by Zimeng Zhang.

Acknowledgement

First and foremost, I am incredibly grateful to my supervisors, Prof Luning Liu and Prof Rob Beynon, for their invaluable tutelage, constant support, and great patience during my PhD study. Their immense knowledge and considerable experience have inspired and encouraged me continuously in my academic research and daily life.

I would like to acknowledge the sponsorship from the University of Liverpool, Graduate Association Hong Kong, and Prof Luning Liu.

My gratitude extends to my academic assessors, Dr James Hartwell and Prof Claire Eyers, for their precious advice; along with my thanks to Dr Meriel Jones, Dr Igor Barsukov, and Prof Mark Caddick for their careful guidance.

I would like to express my sincere gratitude to Dr Tuomas Huokko, Dr Selene Casella, Dr Yi Fang, Dr Gareth Wright, Dr Longsheng Zhao, Mr Gregory Dykes, Dr Catarina Franco, etc. for their teaching and instructions or direct contributions to this work.

I am deeply grateful to everyone in our lab, students and staff, for the constructive conversations and a cherished time we had together in the lab and in social settings.

I would like to offer my special thanks to my family, friends, and mentors. I have had some challenging and overwhelming times in the past few years, and you are the reason I have soldiered on. I cannot list all of your names here, but if you are smiling reading this, you are one of them.

Abstract

The light reactions of photosynthesis occur in thylakoid membranes that are densely packed with a series of photosynthetic complexes, including Photosystem I (PSI), Photosystem II (PSII), cytochrome b_6f (Cyt b_6f) and ATP synthase (ATPase) complexes. Thylakoid membranes also harbour respiratory complexes such as type-I NAD(P)H dehydrogenase (NDH-1), succinate dehydrogenase (SDH) and cytochrome oxidase. The lateral organisation and association of photosynthetic complexes in native thylakoid membranes are vital for efficient light-harvesting and energy transduction. In this work, firstly, a method was reported by integrating immunoprecipitation, mass spectrometry and atomic force microscopy to identify the inter-complex associations of photosynthetic complexes in thylakoid membranes from the cyanobacterium *Synechococcus elongatus* PCC 7942. The possible associations between individual photosynthetic complexes and binding proteins involved in the complex-complex interfaces were characterised, and the structural models of photosynthetic supercomplexes were proposed. Other potential binding proteins of the photosynthetic complexes were also identified, suggesting highly connecting networks associated with thylakoid membranes. Secondly, using a combination of fluorescent dual-labelling and confocal fluorescence microscopy, a study was designed to determine how the distribution of photosynthetic and respiratory complexes was related to that of PSI. Multiple regression analyses revealed that the studied thylakoid membrane protein complexes, including PSII, ATPase, NDH-1 and cytochrome c oxidase, all appeared to have a tendency to colocalise with PSI. The functionally related pairs, such as PSI–PSII in the light, and PSI–NDH-1, showed a higher covariance in terms of colocalisation. Thirdly, Curvature Thylakoid 1 (CURT1) protein was studied. Using genetic engineering, physiological measurements, protein quantification, transmission electron microscopy, fluorescence microscopy and structural characterisation, it was revealed that CURT1 introduced natural curvatures, changed the overall morphology of thylakoid membranes and the densities of photosynthetic complexes in thylakoid membranes.

These studies shed light on the distribution of photosynthetic complexes in thylakoid membranes, provide mechanistic insights into the physical interconnections of photosynthetic complexes and potential partners, and extend knowledge of how the thylakoid membranes are maintained and regulated. Advanced understanding of the protein organisation and interplay of the photosynthetic machinery will inform the rational design and engineering of artificial photosynthetic systems to boost energy production.

Abbreviations

AGC	automatic gain control
ATP	adenosine triphosphate
ATPase	ATP synthase
CAN	Acetonitrile
CFP	cyan fluorescent protein
Chl	chlorophyll
COX	cytochrome oxidase
cryo-EM	cryogenic electron microscopy
cryo-ET	cryogenic electron tomography
cryo-FIB	cryogenic focused ion beam
CURT1	Curvature Thylakoid 1
Cyt b_6f	cytochrome b_6f
Cyt oxidase	cytochrome oxidase
DDM	n-dodecyl β-D-maltoside
DGDG	digalactosyldiacylglycerol
eGFP	enhanced green fluorescent protein
FA	formic acid
Fd	ferredoxin
FDR	false discovery rate
FRAP	fluorescence recovery after photobleaching
FRET	fluorescence resonance energy transfer
Fv/Fm	variable fluorescence / maximum fluorescence
GFP	green fluorescent protein
HPLC	high-performance liquid chromatography
ICM	intracytoplasmic membrane
IPTG	isopropyl β-D-1-thiogalactopyranoside
KD	knockdown
knockout	knockout
LB broth	Lysogeny Broth
LC-MS	liquid chromatography–mass spectrometry
LHCII	light-harvesting complex
MES	2-(N-morpholino)ethanesulphonic acid
MGDG	monogalactosyldiacylglycerol

MS	mass spectrometry
MS/MS	tandem mass spectrometry
NADPH	nicotinamide adenine dinucleotide phosphate
NDH-1	type-I NAD(P)H dehydrogenase
OD	optical density
PAGE	polyacrylamide gel electrophoresis
PBS	phycobilisome
PCC	Pasteur Culture collection of Cyanobacteria
PDM	PratA-defined membrane
PEG	polyethene glycol
PG	phosphatidylglycerol
PQ	plastoquinone
PSI	Photosystem I
PSII	Photosystem II
RC	reaction centre
RuBisCO	ribulose-1,5-bisphosphate carboxylase-oxygenase
RuBP	ribulose-1,5-bisphosphate
SANS	small-angle neutron scattering
SbPase	sédoheptulose-1,7-bisphosphate
SDH	succinate dehydrogenase
SDS	sodium dodecyl sulfate
sp.	species
SQDG	sulfoquinovosyldiacylglycerol
Syn6803	*Synechocystis* sp. PCC 6803
Syn7942	*Synechococcus elongatus* PCC 7942
TBS	Tris-buffered saline
TEM	transmission electron microscopy
TFA	trifluoroacetic acid
TMP14	thylakoid membrane phosphoprotein of 14 kDa
Tris	trisaminomethane
v/v	volume / volume
w/v	weight / volume
WT	wild-type
YFP	yellow fluorescent protein
ΦCO_2	carbon dioxide uptake

Contents

List of figures

List of tables

1 Chapter 1 Introduction

1.1 Photosynthesis

Photosynthesis is a process performed by organisms such as plants, algae and cyanobacteria to convert light energy into chemical energy stored in biomass, which acts as the ultimate energy supply for almost every organism in the biosphere. Photosynthesis, in most cases, is a reaction synthesising carbohydrates and oxygen as a by-product, normally from carbon dioxide and water. The equation of oxygenic photosynthesis was proposed as follows (Singhal et al., 2012).

$$CO_2 + 2H_2O + \text{photons} \rightarrow [CH_2O] + O_2 + H_2O$$

Anoxygenic photosynthesis uses other electron sources instead of water. Anoxygenic photosynthetic organisms include *Chlorobi* (green sulphur bacteria), *Firmicutes* (Heliobacteria) and *Acidobacteria,* which possess Fe-S type reaction centres (RC1) and utilise reducing agents such as H_2S or other sulphates as a proton source.

$$CO_2 + H_2S + \text{photons} \rightarrow [CH_2O] + S + H_2O$$

Other anoxygenic photosynthetic organisms such as *Proteobacteria* (purple bacteria), red and green filamentous phototrophs, e.g. *Chloroflexi* (green non-sulphur bacteria), have pheophytin–quinone type reaction centres (RC2) (Xiong and Bauer, 2002, Bryant et al., 2007, Hohmann-Marriott and Blankenship, 2011, Atamna-Ismaeel et al., 2012). Unlike sulphur bacteria, non-sulphur bacteria are mostly photoheterotrophs that obtain electrons from organic molecules such as sugar, amino acids, organic acids etc. Anoxygenic photosynthesis is believed to have been adopted by the early photosynthetic organisms before the atmospheric oxidation, and the participation of such electron donors is in accordance with the highly reductive primary atmosphere (Gale, 2009, Basak and Das, 2007).

There are two phases in the whole photosynthesis process—in the light-dependent reactions of the first stage, solar energy is captured and triggers chlorophylls to emit one electron, and eventually reduces NADP to produce NADPH. Meanwhile, a gradient of protons is generated through the photolysis of water molecules, and the energy is ultimately stored in ATP molecules by ATP synthase.

$$2H_2O + 2NADP^+ + 3ADP + 3Pi + \text{photons} \rightarrow 2NADPH + 2H^+ + 3ATP + O_2$$

In the second stage, light-independent or dark reactions, the enzyme Ribulose-1,5-bisphosphate carboxylase-oxygenase (RuBisCO) obtains carbon dioxide and fixes it into carbohydrates through the Calvin cycle. This process uses the energy from NADPH and ATP that are generated from light reactions and creates glyceraldehyde 3-phosphates which are later catalysed into polysaccharides. The chemical equation for these reactions can be simplified as follows.

$$3CO_2 + 9ATP + 6NADPH + 6H^+ \rightarrow C_3H_6O_3\text{-phosphate} + 9ADP + 8Pi + 6NADP^+ + 3\ H_2O$$

It is believed that the ability to perform photosynthesis of higher plants comes from cyanobacteria by endosymbiosis, and oxygenic photosynthesis most likely evolved billions of years ago from anoxygenic photosynthetic bacteria (Xiong et al., 2000).

In bacteria, photosynthesis takes place in specialised cellular membranes. In the simplest form of photosynthetic cells, such as cyanobacteria, electron transfer chains and enzymes are embedded in cytoplasmic membranes (Tavano and Donohue, 2006). Purple non-sulphur bacteria employ distinctive subcellular compartments called intracytoplasmic membranes (ICM) that are formed from the invagination of the cytoplasmic membranes and appear as different structures ranging from vesicles to lamellae (LaSarre et al., 2018, Şener et al., 2007). The equivalent in most cyanobacterial species is the thylakoid membranes, which come in a great variety of structures. In contrast to that, photosynthesis in green plants happens in chloroplasts, and the thylakoid membranes in them have quite analogous arrangements—as stacked cylindrical sheets. All these intracellular membrane structures permit membrane systems to increase in grana stacks and have advantages in capturing more light (Mullineaux, 1999).

Photosynthetic organisms use pigments to capture light. The most common pigment employed is chlorophyll *a*. Higher plants synthesise additional pigments such as chlorophyll *b* and carotenoids, which are divided into hydrocarbon carotenes and xanthophylls (Jaleel et al., 2009). Cyanobacteria contain water-soluble chromoproteins—pigment–protein complexes that form phycobilisomes, such as phycocyanin, allophycocyanin and phycoerythrin or erythrophycocyanin, dependent on the species of cyanobacteria. Other pigments found in cyanobacteria include β-carotene, xanthophylls, zeaxanthin and echinenone (Sukenik et al., 2009). The reason for the existence of supplementary pigments is to capture light from a wider range of wavelengths; the mechanism is that pigments pass the captured light through resonance energy transfer until it reaches the chlorophyll *a* molecules in the reaction centre (McCree, 1981).

1.2 Significance of photosynthesis

Several parameters determine the photosynthetic efficiency. According to estimations, the equation of crop yield potential could be calculated with an equation (Monteith, 1977, Long et al., 2006).

$$Y_p = \eta \cdot S_t \cdot \varepsilon_i \cdot \varepsilon_c / k$$

In this equation, Yp is the yield potential to be calculated; η stands for the proportion of biomass harvested, which is hard to take beyond 0.6; k is the energy content of the plant mass which is approximately 17.5 MJ g^{-1} for most plant organs; S_t is the annual integral of incident solar radiation (MJ m^{-2}) that is determined by location and time; ε_i designates the efficiency of light capture which is around 0.9 due to technical limitations; ε_c represents the efficiency in converting sunlight into biomass, regulated by photosynthesis and respiration and is the remaining main prospect for improving crop yield (Long et al., 2006).

Several potential approaches have been proposed to boost photosynthetic efficiency. A primary aspect to consider is the efficiency of light-harvesting. It has been estimated that photosynthetic organisms harvest only 25% of the solar energy, and the rest is wasted in the form of reflection, heat and exclusion from the absorbance spectra (Cotton et al., 2015). It was found that with decreased antenna size, tobacco accumulated 25% more leaf and stem biomass compared to wild type due to reduced shading (Kirst et al., 2017). Researchers also proposed that introducing new antennae and synthesising new pigments might potentially boost light-harvesting efficiency (Cardona et al., 2018). Photoprotection is another factor that impairs photosynthetic efficiency. The mechanism is that photosynthetic organisms form epoxidated xanthophylls to dissipate thermal energy as a means to avoid the damage caused by excess light to apparatus such as Photosystem II (Long et al., 1994, Baroli and Niyogi, 2000, Havaux and Niyogi, 1999). By reducing the maximum quantum yield of PSII (Fv/Fm) and carbon dioxide uptake (ΦCO_2), carbon gain in high light is inhibited and it takes time to recover (Zhu et al., 2004). During dark reactions, the main aspect that causes energy waste in photosynthesis is photorespiration, which adds oxygen to ribulose 1,5-bisphosphate (RuBP) instead of carbon dioxide by ribulose-1,5-bisphosphate carboxylase-oxygenase (RuBisCO), leading to side reactions off the main Calvin cycle. The ratio of photorespiration to photosynthesis in C3 plants is estimated to be 25% without interference (Sharkey, 1988). By contrast, C4 plants inhibit photorespiration by separating CO_2 fixation and Calvin cycles into mesophyll cells and bundle-sheath cells; while Crassulacean acid metabolism (CAM) plants do so by only allowing CO2 to enter during the night. In summary, current studies focus on enhancing light-harvesting efficiency, promoting fast-recovery from photoprotection, inducing C4 and CAM photosynthesis into other species, RuBisCO engineering, suppressing the oxygenase activity of RuBisCO and accelerating the restoring of RuBP by sedoheptulose-1,7-bisphosphatase (SbPase) etc.(Long et al., 2006).

Studying photosynthesis has huge potential to bring benefits. As the very basis of agriculture, enhancing the efficiency of photosynthesis will substantially benefit the production of food, natural fibres, biofuels such as ethanol, and general energy. Furthermore, it provides theoretical support for the potential future creation of artificial photosynthetic membranes or devices. The principles underlying photosynthesis could inspire the design of electronic circuits and electronic devices, as the dimensions of photosynthetic apparatus are around nanometres, which is close to those of the finest integrated circuit-creating mask aligners. In addition, the photoprotective mechanisms of plants could possibly enlighten approaches to treating photodamage in humans and animals.

1.3 Chloroplasts and cyanobacteria

As discussed above, the chief organisms able to conduct photosynthesis include plants, algae, cyanobacteria and other anoxygenic photosynthetic bacteria. In addition, the unicellular *Euglena* is believed to be another genus with the photosynthetic ability (Stern et al., 1964, Zakryś et al., 2017). Cyanobacteria are often regarded as a good model organism to study photosynthesis, given their short life cycle and accessibility to genetic modifications.

The evolutionary precursor of chloroplasts is assumed to be an organism close to cyanobacteria, and the current theory proposes that there is only one origin for all plastids (Palmer, 2003). As illustrated in Figure 1-1, the antecedent cyanobacteria have phycobilisomes as light-harvesting antennae, which were retained in red algae but are absent from all land plants. The reason for this has been proposed to be due to the fact that when photosynthetic organisms started to inhabit the land, the high intensity of light obviated the necessity to have big light-harvesting antennae, as they incur a biochemical cost. However, when plants started to occupy shaded terrestrial habitats, they developed the grana and Photosystem II (PSII) light-harvesting antennae to concentrate the light energy that can be received in PSII (Mullineaux, 2005).

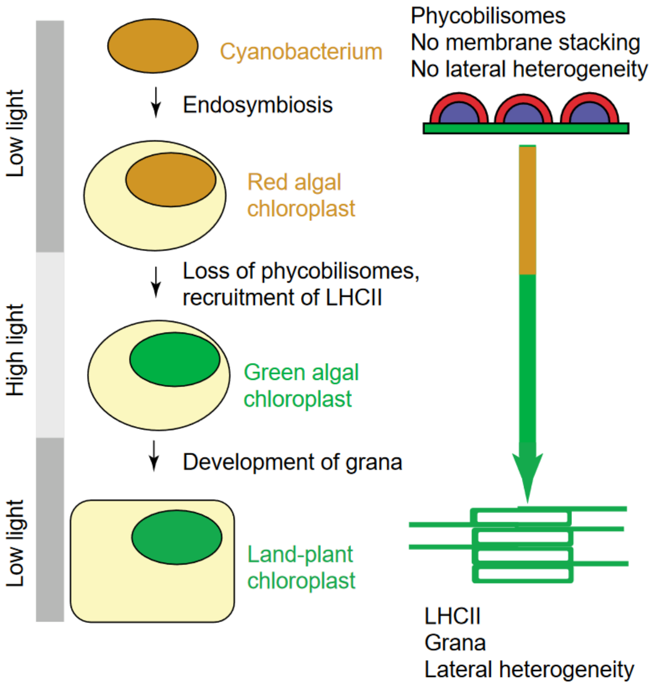

Figure 1-1 A hypothesis of the evolution of cyanobacteria to chloroplasts (Mullineaux, 2005).

Red algae were the first eukaryotic organisms able to perform photosynthesis, with the organisation of thylakoid and pigments similar to cyanobacteria. It was proposed that to adapt to higher light conditions, the functions of phycobilisomes were replaced with the light-harvesting complex (LHCII).

1.4 Thylakoids

The thylakoid membranes are a compartment where the light reactions of photosynthesis are localised and carried out. The difference in the thylakoid structure and organisation between species is remarkable. Patterns of the thylakoid architecture exhibit an immense diversity among different cyanobacterial strains (further discussed in Section 1.4.3); *Synechococcus elongatus* PCC 7942 has parallel thylakoid membranes (Figure 1-2A). As demonstrated in a model shown in Figure 1-2B, chloroplasts in land plants generally possess a unique structure called grana, which are normally 300–600 nm in size with 10–20 layers of thylakoid membranes stacked together, with the adjacent stromal sides only having a spacing of 2.5 nm in between (Mullineaux, 2005, Kirchhoff et al., 2004). Granal stacks are surrounded by stromal lamellae that are loosely organised. The protein composition of thylakoid membranes displays pronounced heterogeneity, with PSII and LHCII distributed overwhelmingly in the stacked grana regions, while PSI, cytochrome b_6f and ATP synthase locate dominantly in the membrane exposed to the stroma (Dekker and Boekema, 2005).

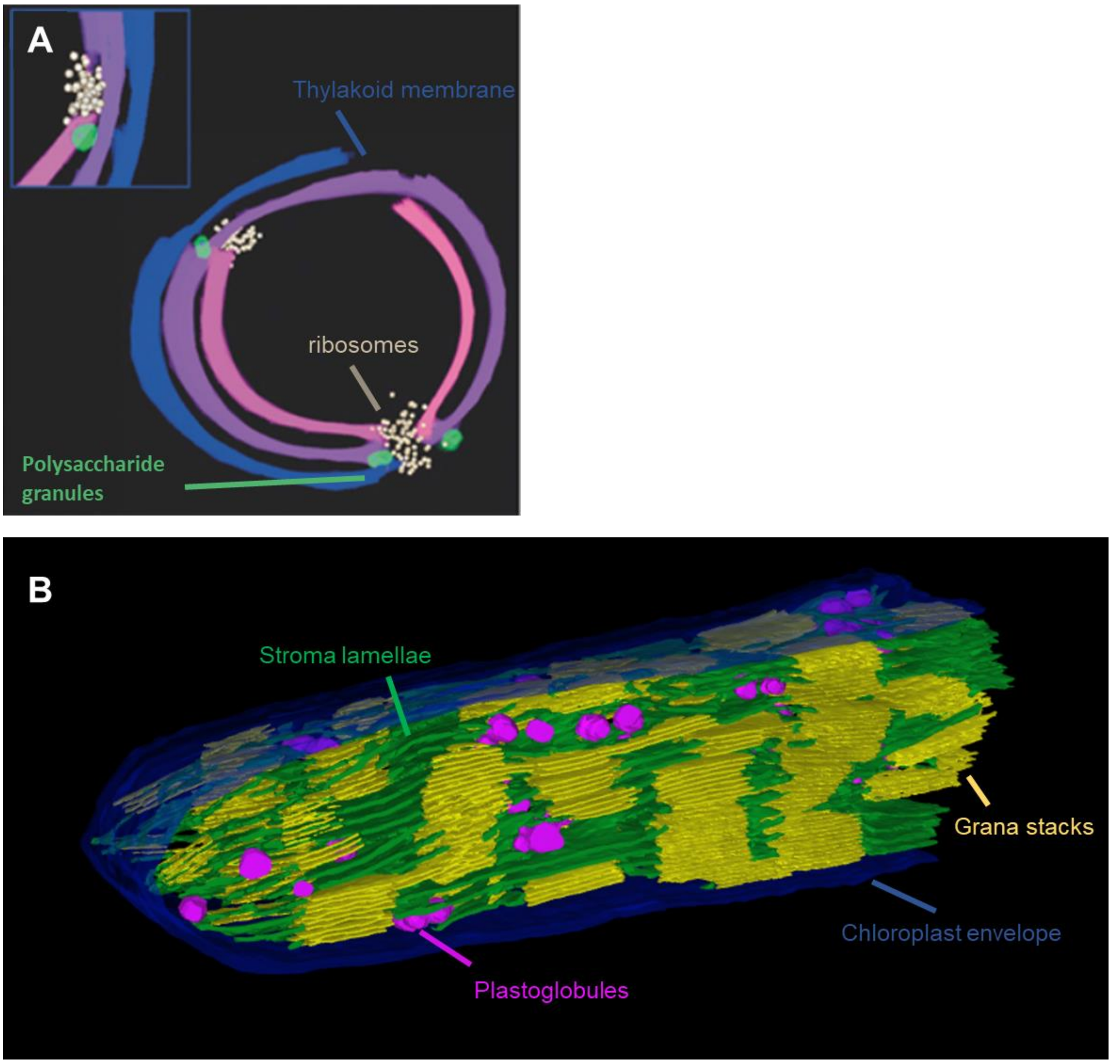

Figure 1-2 Models of the thylakoid membranes of cyanobacteria and plants.

(A) Model of the thylakoid membranes in *Synechococcus elongatus* PCC 7942 processed from cryo-immobilised, freeze-substituted electron microscope tomography. The thylakoid membranes (blue, purple and pink), ribosome (beige) and polysaccharide granules (green) are labelled (Nevo et al., 2007).

(B) Model of the chloroplast of *Lactuca sativa L.* (lettuce) by tomographic reconstruction by transmission electron microscopy. Stroma lamellae (green), grana (yellow), chloroplast envelope (blue) and plastoglobules (magenta) are labelled (Bussi et al., 2019).

1.4.1 Electron transfer chains

In cyanobacteria, most electron transfer chains for energy generation are located in the thylakoid membrane. These include the photosynthetic linear and cyclic electron transfer pathway and respiratory electron transfer pathway. Figure 1-3 portrays the electron transfer between the protein complexes within and associated with the thylakoid membranes. Photosystem II (PSII) splits the H_2O molecules to produce O_2; an electron is donated to a plastoquinone by PSII and then transferred to the cytochrome b_6f complex, plastocyanin, and Photosystem I (PSI), where it reduces $NADP^+$ to NADPH and provides reducing power for biosynthetic reactions.

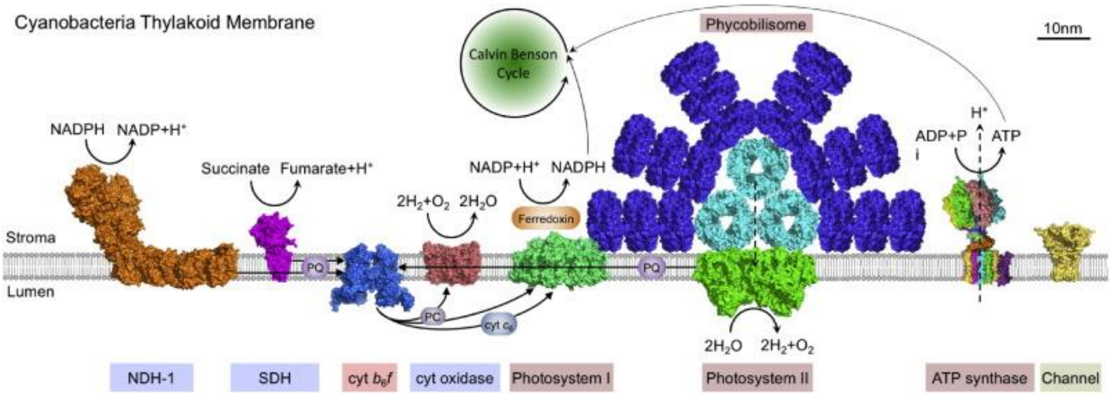

Figure 1-3 Representation of the electron transport pathways in the thylakoid membrane (Liu, 2016).

Photosystem II donates an electron to a plastoquinone; the electron is subsequently transferred to the cytochrome b_6f complex, plastocyanin, and photosystem Photosystem I, where the electron provides reducing power for NADPH generation biosynthetic reactions.

1.4.2 Photosynthetic complexes

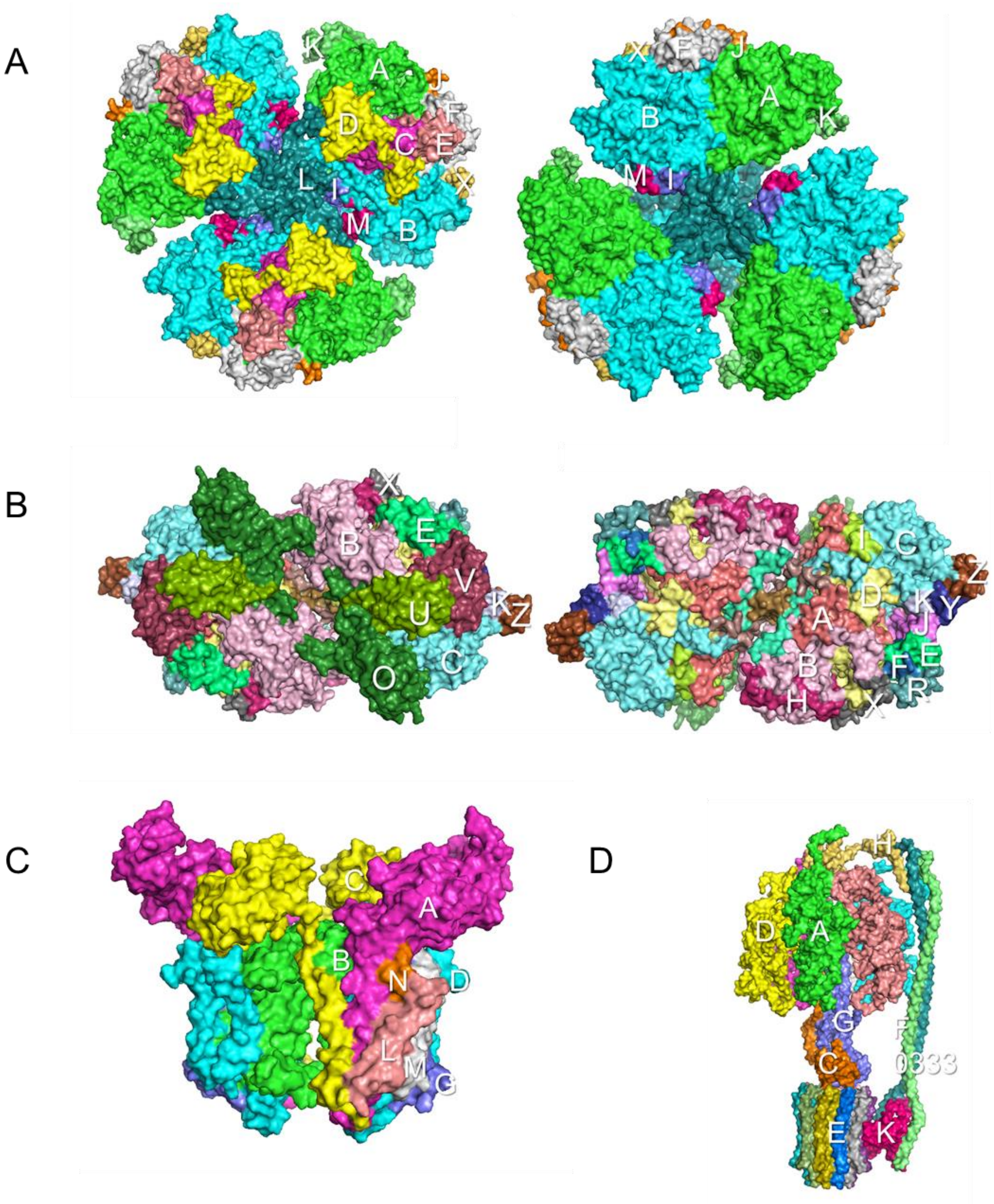

Figure 1-4 Structure of photosynthetic complexes with protein subunits labelled. Protein structures were obtained from PDB (PSI: 1JB0; PSII: 3WU2, Cyt b$_6$f: 4H13, ATPase: 6FKF).

(A) Cytoplasmic side and lumenal side view of PSI. The structure was generated with X-ray crystallography (Jordan et al., 2001).

(B) Lumenal and cytoplasmic side view of PSII. The structure was generated with X-ray crystallography (Umena et al., 2011).

(C) Side view of cytochrome b_6f with the lumenal side facing the top. The structure was generated with X-ray crystallography (Hasan et al., 2013).

(D) Side view of ATPase with the cytoplasmic side facing the top. The structure was generated with X-ray crystallography (Hahn et al., 2018).

PSI (Figure 1-4A) can exist as either monomers or trimers in cyanobacteria. A monomer of PSI is made of these listed subunits: PsaA, PsaB, PsaC, PsaD, PsaE, PsaF, PsaI, PsaJ, PsaK, PsaL, PsaM and PsaX. PSI has more than 110 co-factors, e.g. an electron donor P-700 (chlorophyll dimer) and five electron acceptors: A0 (chlorophyll), A1 (a phylloquinone) and three 4Fe-4S iron-sulphur centres—Fx, Fa, and Fb (Schaechter, 2009). The electron is eventually transferred to ferredoxin and ferredoxin-NADP oxidoreductase, where $NADP^+$ is reduced to NADPH.

PSII (Figure 1-4B) normally exists as dimeric complexes in cyanobacteria. The reaction centre (RC) core is where light energy is transformed into electrochemical potential energy and where the water-splitting reaction occurs. The RC is attached to the light-harvesting systems composed of phycobilins. Typically, 200–300 light-harvesting pigment molecules supply energy to one PSII RC (Barber, 2006). The RC core consists of two homologous proteins—the D1 protein (PsbA) and D2 protein (PsbD); both of them have five transmembrane α-helices. The CP43 (PsbC) and CP47 (PsbB) subunits are connected with RC, each having six transmembrane α-helices. PSII has some intrinsic protein subunits (e.g. PsbE and PsbF) and extrinsic subunits (e.g. PsbO).

The cytochrome b_6f complex (Figure 1-4C) is vital in both the respiratory and the photosynthetic electron transport chains. Its role is plastoquinol oxidation and electron transfer to plastocyanin. Cytochrome b_6f is composed of four major subunits and four minor subunits. The four major ones include cytochrome f (PetA), cytochrome b_6 (PetB), a Rieske iron-sulfur protein (PetC) and subunit IV (PetD); The small subunits are PetG, PetL, PetM and PetN. However, the petL gene cannot be found in *Synechococcus elongatus* PCC 7942 and is not essential in *Synechocystis* sp. PCC 6803 (Schneider et al., 2007).

ATP synthase (Figure 1-4D), also called F-type ATPase, is an enzyme that performs oxidative and photosynthetic phosphorylation, transforming both respiratory and photosynthetic energy into the energy of the chemical bond in ATP. F_0 complex (proton channel) and F1 complex (catalytic site) constitute ATP synthase. The F_0 complex comprises three types of subunits—a, b, and c that make up the 14-subunit ring. The F1 complex is made of 5 types of subunits—alpha, beta, gamma, delta, and epsilon. In cyanobacteria, the F1 complex faces the stroma.

1.4.3 Variety of photosynthetic membrane structures

The organisation of the thylakoid membranes between different cyanobacterial strains varies (Mareš et al., 2019). The thylakoid membranes can be absent in organisms such as *Gloeobacter violaceus* PCC 6501 or parietal, e.g. *Synechocystis* sp. PCC 6803 and *S.* sp. PCC 7002, or radial, e.g. *Coleofasciculus chthonoplastes* PCC 7420, or fascicular as *Synechocystis* sp. PCC 7509, or parallel such as *S. elongatus* PCC 7942 etc. (Mareš et al., 2019). It has been found that the distances between thylakoid membranes are associated with the size of the phycobilisome antenna and can be adjusted reversibly under photosynthetic regulation, e.g., between light and dark (Liberton et al., 2013). Small-angle neutron scattering (SANS) data showed that the distance between thylakoid membrane layers among different cyanobacteria strains is not consistent, ranging from 630 Å, which can accommodate phycobilisomes, to 110 Å, which is very stacked with constricted interval space (Liberton et al., 2013). High-resolution inelastic neutron scattering experiments revealed that the thylakoid membrane in cyanobacteria has greater flexibility in the dark than in the light, and it was proposed that the repelling of excess protons from photosynthesis on the thylakoid lumen side could lead to constriction of the membrane in the light (Stingaciu et al., 2016).

1.4.4 Grana and quinone diffusion

Much uncertainty still exists about the functions of grana, which have been the subject of intense debate within the field of photosynthesis. Some researchers argued that the formation of granal stacks acts as a physical separation of PSI and PSII to prevent energy spillover, therefore avoiding the fast energy trapper PSI to trap disproportionately excess energy, leading to an imbalance within electron transfer (Trissl and Wilhelm, 1993). Other investigators suggested that the existence of grana facilitates the regulation of light harvest by manipulating the phosphorylation of LHCII and thus controlling the detaching and attaching of LHCII between PSII and PSI (Allen and Forsberg, 2001). These two possibilities have been precluded from the primary function of the grana (Mullineaux, 2005), as both purposes have been already fulfilled in cyanobacteria. Hence, the development of the novel grana seems to be a waste. The author proposed that the chief reason for grana formation is to offer enough space in lipid for the diffusion of plastoquinone, which is the electron receptor of type 2 reaction centres including PSII in cyanobacteria and plants, and reaction centres in purple and green bacteria (Heathcote et al., 2002).

Photosynthetic organisms have different mechanisms to acquire enough space for plastoquinone diffusion, as depicted in Figure 1-5. The reaction centre of the purple bacterium *Rhodobacter sphaeroides* has light-harvesting complex LH1 surrounding it, but a gap is left by the protein PufX (Siebert et al., 2004, Qian et al., 2013). While the light-harvesting complex LH2 leaves lipid membrane spaces from the core that consists of LH1 and reaction centre, which is favourable for quinone diffusion (Liu et al., 2009b). The green filamentous bacterium *Chloroflexus aurantiacus* and cyanobacteria have light-harvesting antennae on top of their reaction centres rather than around them in the lipid bilayer, allowing capacious room for quinone to travel. In plants, the grana are proposed to perform a similar function—they bring close light-harvesting LHCII without allocating all of them around PSII, thus leaving space for quinone diffusion (Mullineaux, 2005).

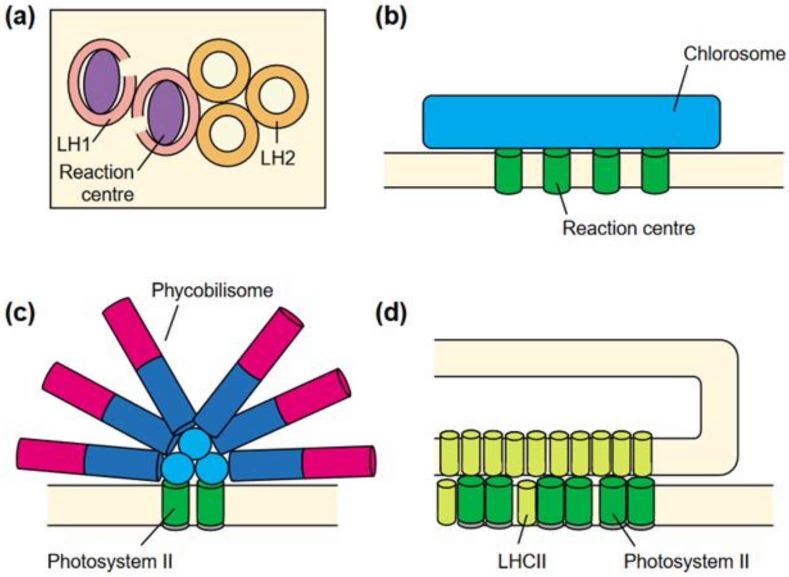

Figure 1-5 Four strategies to build light-harvest antenna allowing plastoquinone diffusion (Mullineaux, 2005).

(A) The purple bacterium *Rhodobacter sphaeroides* has LH1 rings with gaps and isolated LH2 to allow quinone diffusion.

(B) The light-harvesting antenna in the green filamentous bacterium is not embedded in the membrane; instead, it sits on the top of the reaction centre.

(C) The light-harvesting antenna phycobilisome is attached to the top of PSII.

(D) A hypothetic model of the PSII harvesting more light from light-harvesting antenna LHCII without having all of them surrounding it, leaving enough space for the diffusion of plastoquinone.

1.4.5 Heterogeneous distribution of thylakoid membrane complexes

In plants, lateral heterogeneity is used to characterise the non-homogeneous distribution of photosynthetic apparatus in the thylakoids, as discussed in Section 1.4. In cyanobacteria, different approaches were developed to study the heterogeneous distribution of thylakoid membrane complexes. Using immuno-gold and transmission electron microscopy, a report showed that PSI and ATPase were dominantly found in the outer layer of *S. elongatus* PCC 7942 (Sherman et al., 1994). On the contrary, with *in vivo* hyperspectral confocal fluorescence in *Synechocystis* 6803, it has been proposed that short-wavelength chlorophyll fluorescence attributed to PSII was found concentrated near the periphery of the cell. In contrast, long-wavelength chlorophyll originated from PSI was observed in the inner thylakoid (Vermaas et al., 2008). Membrane fractions isolated using ultracentrifugation combined with mass spectrometry showed that thylakoid membrane in *Synechocystis* 6803 pelleted at 40,000 g, 90,000 g, or 150,000 g demonstrated different absorption spectra and contained different proteins (Agarwal et al., 2010). *In vivo* confocal fluorescence microscopy of *S. elongatus* PCC 7942 revealed that PSI, PSII, cytochrome b_6f and ATPase all had a certain level of distributional heterogeneity; among these complexes, PSII had the most uniform fluorescence along the thylakoid membranes (Casella et al., 2017). Further studies with fluorescence microscopy in the same species showed that the intracellular localisation of photosynthetic complexes, especially of PSI, was evidently uneven during thylakoid membrane generation (Huokko et al., 2021). Still, in *S. elongatus* PCC 7942, atomic force microscopy directly visualised the complex compartmentalisation and lateral heterogeneity in thylakoid membranes (Zhao et al., 2020). Different studies also found that photosynthetic complexes sometimes form supercomplexes among PSI, PSII and phycobilisomes (Liu et al., 2013), PSI and phycobilisomes (Watanabe et al., 2014), PSI and PSII (Bečková et al., 2017) as well as PSI and NADH dehydrogenase-like complex type-1 (NDH-1) (Gao et al., 2016) (discussed in detail in Chapter 3). In precis, the thylakoid membranes are a complicated compartment in which there has been a paucity of evidence about the distribution and coordination of photosynthetic and respiratory complexes.

1.5 Model organisms

A few organisms have been used extensively as model organisms in photosynthesis research. A great deal of previous research into enhancing crop yield has focused on cereal model organisms such as maize (*Zea mays* L.) and rice (*Oryza sativa*). Compared to other cereal plants, maize has been a model organism for the longest time because of the convenience to cross and separate male and female flowers, and mutations can be easily observed on their copious, aligned seeds. Rice has a small, sequenced genome size of 387.14 Mb (Goff et al., 2002, Zhou et al., 2007). Due to the fact that plants typically have a large genome size, relatively long life cycle, and require a large space to grow, *Arabidopsis thaliana* was adopted as the most amenable model plant, and it was the first plant to have its genome sequenced. Likewise, *Physcomitrella patens* is also a prevalent model due to the possibility of generating knockout strains by recombination (Reski, 1998); and its sequenced genome was the first for a non-vascular plant (Rensing et al., 2008).

Nevertheless, higher plants generally have a much longer generation time, and their cultivation is relatively labour intensive. Compared to *A. thaliana,* which has a life cycle of several months, and *P. patens* which takes several weeks, cyanobacteria such as *Synechocystis* [7~10 h doubling time under optimal light conditions (Yu et al., 2013)] and *S.* [optimal 6~7 h doubling time (Mori et al., 1996)] only need less than one day (Jensen and Leister, 2014). They can grow in a liquid, standardised medium. As shown in Figure 1-6A and 6B, *S.* sp. PCC 6803 is a spherical, unicellular freshwater cyanobacterium species that is able to conduct both photoautotrophic and heterotrophic growth. Their nutrition comes from oxygenic photosynthesis in the light and the organism can also live on energy from glycolysis and oxidative phosphorylation (Heidorn et al., 2011). By contrast, *S. elongatus* PCC 7942 is a rod-shaped unicellular, freshwater cyanobacterium (Figure 1-6C and 1-6D). Once maintained in the stationary phase, it has prolonged growth without division (Goclaw-Binder et al., 2012). The genome copy number is highly correlated with the size of cells (Sugita et al., 2007). Given the elongated shape and regular thylakoid membrane structures, it is a good model for thylakoid membrane studies. *S. elongatus* PCC 7942 only lives on oxygenic photosynthesis, making it an ideal system to carry out photosynthetic studies on. Furthermore, *S. elongatus* PCC 7942 has the natural capacity of taking up heterologous genes. A comparison of the genome sequences between *S. elongatus* PCC 6301 and *S. elongatus* PCC 7942 revealed that the major difference was a 188.6 kb inversion that contributes to mutated porin-like proteins (Figure 1-7), which might lead to the natural transformation capacity of *S. elongatus PCC 7942* (Sugita et al., 2007).

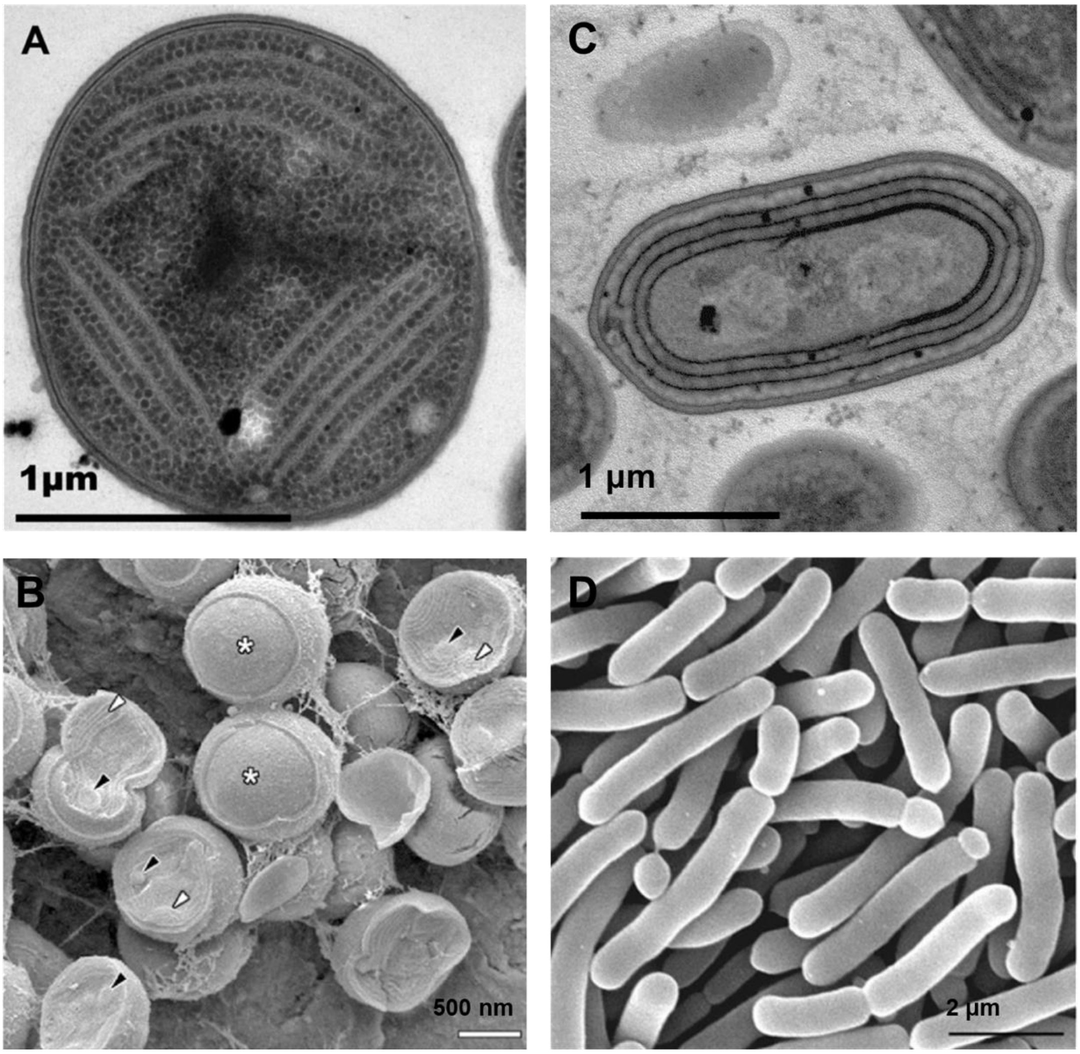

Figure 1-6 Morphology of *Synechocystis* sp. PCC 6803 and *S. elongatus* PCC 7942.

(A) Transmission electron microscopy of *Synechocystis* PCC 6803 wild-type cells (Welkie et al., 2016).

(B) Cryo-Scanning electron microscopy of *Synechocystis* sp. PCC 6803, freeze-fractured with revealed cytoplasmic membrane (asterisks), thylakoid membranes (white arrows) and inclusions (black arrows) (Van De Meene et al., 2006).

(C) Transmission electron microscopy of *S. elongatus* PCC 7942.

(D) Scanning electron microscopy *S. elongatus* PCC 7942 (Gorelova et al., 2013).

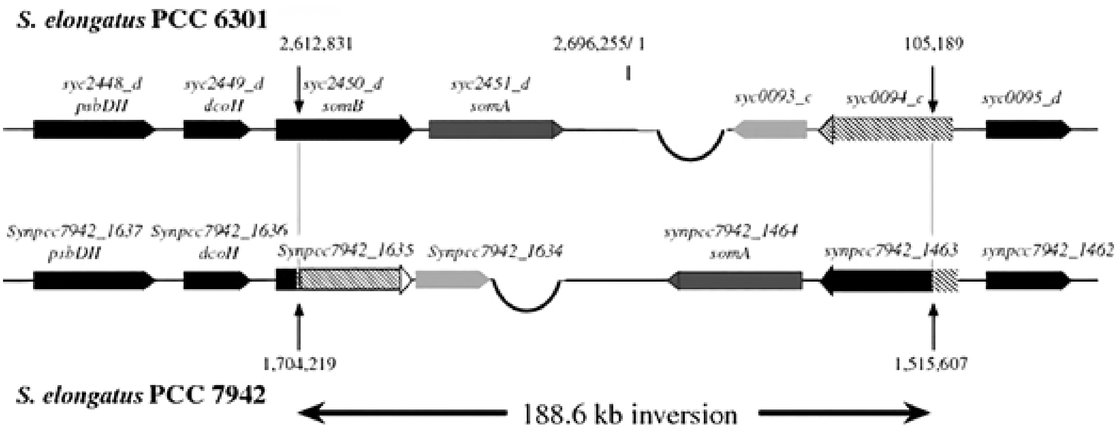

Figure 1-7 The major genetic difference between *S.* PCC 6301 and *S. elongatus* PCC 7942 (Sugita et al., 2007).

The 188.6 kb inversion results in mutations in porin-like proteins, and those in *S. elongatus* PCC 7942 are believed to facilitate the natural transformation ability.

The 2.7 Mb genome of *S. elongatus* PCC 7942 has been sequenced (Holtman et al., 2005) (Gene bank GCA_000012525.1). Flow cytometry data demonstrated that the average genome number per cell varies between 4 to 7, which is highly correlated to division events (Mori et al., 1996). Furthermore, later research revealed that in a fluorescent repressor-operator system, labelled DNA-binding proteins provide a visualisation of the cyanobacterial genome distributing along the long axis of the cell (Chen et al., 2012, Jain et al., 2012). Multiple genome sets lead to a longer time of gene segregation during transformation. In 2015, the proteomic data of *S. elongatus* PCC 7942 with coverage as high as 68% of the nucleotide sequence was published (Yu et al., 2015b), which provides information about protein expression and posttranslational modifications, which further helps with future studies.

1.6 Aims of this PhD project

Numerous studies have attempted to reveal the thylakoid membrane structures and the organisation of the protein complexes within the membranes. A considerable amount of the literature has focused on the visualisation of the thylakoid membranes and their embedded proteins by atomic force microscopy (AFM), which is a powerful tool to distinguish protein complexes with a conspicuous shape at high-resolution and under near-physiological conditions (MacGregor-Chatwin et al., 2019, MacGregor-Chatwin et al., 2017, Zhao et al., 2020, Liu and Scheuring, 2013). What is known about the thylakoid membrane protein distribution *in vivo* is largely based upon empirical studies with fluorescence microscopy (Casella et al., 2017, Mullineaux et al., 1997, Liu et al., 2012). Publications that concentrate on the structure of the thylakoid membranes more frequently adopt cryogenic electron microscopy (cryo-EM) techniques and neutron scattering, as stated before. However, much of the research up to now has not been able to resolve the interaction between different proteins on the thylakoid membrane and shows inadequacies in the regulation of the thylakoid membrane *in vivo*.

This thesis aims to provide insights into the interactions between thylakoid protein complexes and explore the factors that determine the structure and constitution of the thylakoid membranes with the model cyanobacterium *S. elongatus* PCC 7942. Using a combination of immunoprecipitation and mass spectrometry, this study identified the composition of strongly-interacting protein pairs in the electron transport chain. Further, it investigated the colocalisation with fluorescent dual-labelling and confocal microscopy in living cyanobacterial cells. In addition, by employing a combination of physiological measurements, fluorescent microscopy, protein purification and structural analysis, this study illuminates how the thylakoid membrane and protein complexes are regulated by the Curvature Thylakoid 1 (CURT1) protein.

2 Chapter 2 Methods

2.1 Strains and cell culture

Synechococcus elongatus PCC 7942 strain (pre-existing in this lab) was used in this research. All cell cultures were incubated in BG11 medium (Rippka et al., 1979) at 30°C under 40 μmol·m^{-2}·s^{-1} white illumination in Nunc™ Cell Culture Treated TripleFlasks^{TM} with constant shaking. For a longer-term, strains were kept on BG-11 plates with 1.5% bacteriological agar (Agar bacteriological LP0011B ThermoFisher Scientific). Long-term strains storage was achieved by mixing cells with 8% DMSO as a cryoprotectant, snap freezing with liquid nitrogen, and keeping them at -80 °C.

2.2 Generation of transgenic cyanobacterial strains

GFP, CFP, YFP labelling and knockdown/knockout strains were generated using the Redirect strategy (Gust et al., 2002, Gust et al., 2004). In brief, the fluorescently labelled strains were generated by inserting GFP/CFP/YFP/KO cassettes into the 3' end of genes as stated in previous studies (Huang et al., 2020, Sun et al., 2019, Huang et al., 2019, Faulkner et al., 2017, Casella et al., 2017). Firstly, the target gene was cloned to the pGEM-T easy vector (ampicillin) (Promega) using an optimal condition selected from gradient PCR (primers: F: 20 bp at 800 bp upstream of the gene; R: 20 bp at 800 bp downstream of the gene) (Table 2-1).

Table 2-1 The PCR programme for target gene cloning.

Cycle 1 × 1	94°C, 2 min
Cycle 2 × 15	94°C, 45 s; 45–55°C, 45 s; 72.0°C, 4 min
Cycle 3 × 15	94°C, 45 s; 55–65°C, 45 s; 72.0°C, 1 min 30 s
Cycle 4 × 1	72°C, 10 min

The plasmid was then transferred to the *E. coli* strain DH5α to achieve a higher copy number of the plasmids. The transfer was completed with the heat shock strategy described before (Froger and Hall, 2007). The plasmids were subsequently extracted with GeneJET Plasmid Miniprep Kit (Thermo Fisher) and transferred to BW25113 competent cells (Grenier et al., 2014) by electroporation with a pre-existing pIJ790 plasmid (chloramphenicol) carrying the homologous recombination system. Next, the GFP/CFP/YFP/KO cassette specific for this certain gene was cloned from either pIJ786 plasmid (GFP: apramycin; CFP: kanamycin; YFP: apramycin) or PIJ778 plasmid (KO, spectinomycin) using REDIRECT programme (Table 2-2) (primers: F: 39 bp before stop codon + 20 bp plasmid linker region for GFP/CFP/YFP and 39 bp before start codon + 20 bp plasmid linker region for KO/KD; R: 39bp after stop codon + 20 bp plasmid linker region)

Table 2-2 The REDIRECT PCR programme.

Cycle 1 × 1	94°C, 2 min
Cycle 2 × 15	94°C, 45 s; 50°C, 45 s; 72.0°C, 1 min 30 s
Cycle 3 × 15	94°C, 45 s; 55°C, 45 s; 72.0°C, 1 min 30 s
Cycle 4 × 1	72°C, 10 min

The cassette was transferred to BW25113 cells through the second electroporation. After homologous recombination, 100 ng plasmids were extracted and transferred to 1.5 mL (OD_{750} = 1.0–2.0, resuspended to 100 µL) cyanobacteria by mixing and overnight incubation. Cells were then plated on BG-11 agar plates and refreshed every week until the target gene had segregated. Segregation was verified with segregation primers (20 bp at 100–150 bp upstream of the 39 bp redirect F for F primers and 20 bp at 100–150 bp downstream of the 39 bp redirect R for R primers) using the REDIRECT programme (Table 2-2). The GFP-labelled strains in Chapter 3 (psaE of

PSI, psbB of PSII, petA of Cyt b_6f and atpB of ATPase) were generated in a previous study (Casella et al., 2017). Other strains were generated in this study.

2.3 Thylakoid membrane isolation and solubilisation for pull-down assays

WT and GFP-labelled Syn7942 cells were harvested when the OD_{750} reached between 0.6 and 1.0. Cells were then pelleted by centrifugation at 4,000 g for 10 mins at 4°C (Sorvall, SS-34 rotor) and washed with buffer A (50 mM MES-NaOH, pH 6.5, 5 mM $CaCl_2$, and 10 mM $MgCl_2$). Cell pellets were resuspended in buffer A containing 25% glycerol and were broken by glass bead (212–300 µm in diameter, Sigma-Aldrich) at 4°C with a vortex at 2,700 rpm 5 times, 1 min on and 1 min off, and then 10 times, 30 s on and 30 s off. Crude thylakoid membrane fractions were prepared by centrifugation (Zhang et al., 2004). They were resuspended in membrane resuspension buffer (10 mM Tris pH 6.8, 200 mM NaCl, 1 mM EDTA) to obtain a 200 $\mu g \cdot mL^{-1}$ chlorophyll (Chl) concentration. The thylakoid membrane fractions were then solubilised with 1% digitonin (Sigma-Aldrich) for 30 min at room temperature, shaking on a vortex at 600 rpm. The solubilised thylakoid membrane proteins were extracted by centrifugation at 40,000 g for 30 min (Sorvall, SS-34 rotor) followed by centrifugation at 21,100 g for 20 min (Thermo Scientific™ Fresco™ 21 Microcentrifuge).

To ensure both membrane solubilisation and intactness of membrane complexes, pre-experiments with different treatment conditions [different detergents—digitonin and n-dodecyl β-D-maltoside (DDM), different detergent concentration (1–10%), different solubilisation time (10–30 min), different centrifugation force (21.1 kg–40 kg) and centrifugation time (10–120 min)] were examined by transmission electron microscopy. The above-described protocol was found to be the most efficient for thylakoid complex isolation (discussed in Section 3.2.1).

2.4 GFP pull-down assays

GFP pull-down assays were carried out using µMACS and MultiMACS GFP Isolation Kits (Miltenyi Biotec). Thylakoid membrane protein samples with 10 µg Chl *a* were incubated with 50 µL beads, and membrane resuspension buffer was added to reach a total volume of 200 µL. The columns were prewashed with lysis buffer from the kit. After the samples were loaded, the columns were further washed five times with the membrane resuspension buffer mentioned above before elution. For SDS-PAGE analysis, proteins were eluted with 50 µL elution buffer following the instructions provided by the manufacturer, and 10 µL of samples were loaded onto a 12% SDS gel with 4× sample buffer [1.57% Tris-HCl pH 6.8, 4% SDS (w/v), 20% glycerol, 0.1% bromophenol blue (w/v), 1.5% dithiothreitol (w/v)]. For mass spectrometry, bound proteins and beads were collected by taking the column out of the magnetic field and were washed with 50 µL membrane resuspension buffer; 10 µL was used for SDS-PAGE, and 40 µL was used for proteomic analysis.

2.5 Thylakoid membrane isolation

Thylakoid membranes were isolated when the cyanobacterial culture reached the exponential phase (OD_{750}=0.8). Cultures of 40 mL culture were pelleted at 5000 g, 4 °C for 10 min (Sorvall, SS-34 rotor) and washed in 10 mL washing buffer [50 mM HEPES (NaOH, pH 7.5), 30 mM $CaCl_2$]. Pellets were resuspended in 200–300 µL resuspension buffer [50 mM HEPES (NaOH, pH 7.5), 30 mM $CaCl_2$, 800 mM sorbitol, 1 mM 6-aminohexanoic acid] with the same volume of glass beads (150–212 microns, Sigma G-1145), and broken by vortexing 1 min 6 times at 4 °C, with a cooling time of 1 min in between. After a spin at 3000 g, 4 °C for 2 min (Thermo Scientific™ Fresco™ 21 Microcentrifuge), the supernatant was collected, and the pellet was vortexed once more with an extra 0.5 mL resuspension buffer. The supernatants were combined and centrifuged at 18,000 g, 4 °C for 30 min (Thermo Scientific™ Fresco™ 21 Microcentrifuge), and the pellet was resuspended again in a resuspension buffer.

2.6 SDS-PAGE

For pull-down experiments, 10 µL of the samples were loaded onto a 12% sodium dodecyl sulfate (SDS) gel with 4 × sample buffer [1.57% Tris-HCl pH 6.8, 4% SDS (w/v), 20% glycerol, 0.1% bromophenol blue (w/v), 1.5% dithiothreitol (w/v)]. For isolated thylakoid membrane samples, total protein was measured using dye binding protein assay (Bradford) and loaded according to Table 2-1. All samples were solubilised with 4 × sample buffer [1.57% Tris-HCl pH 6.8, 4% SDS (w/v), 20% glycerol, 0.1% bromophenol blue (w/v), 1.5% dithiothreitol (w/v)] and heated at 95°C for 10 min before loading. Proteins were separated by 12% denaturing SDS-PAGE.

2.7 Western blot

Gels from SDS-PAGE were electrotransferred to PVDF membrane (GE Healthcare) at 90 V, 45 min in transfer buffer (glycine 0.29% w/v, TRIS 0.58% w/v, SDS 0.037% w/v, methanol 20%). The PVDF membranes were washed in TBS buffer (20 mM Tris-HCl, 0.15 M NaCl, pH 7.5) and blocked with 5% milk powder (w/v) in TBS buffer at room temperature for 60 min. Next, the blocked membranes were washed twice with TTBS buffer (TBS buffer with 0.1% Tween 20) for 5 min on a shaker at 90 rpm. Membranes were incubated with the primary antibody (dilution and loading conditions listed in Table 2-3) diluted with TBS buffer with 1% milk powder (w/v) at room temperature for 3 h with shaking and washed with TTBS buffer 4 times as before. Incubation with the secondary antibody for 1.5 h at room temperature was followed by washing with TTBS three times and TBS two times, 5 min each. The membranes with antibodies were treated with the Clarity Western ECL substrate (Bio-Rad) and imaged with ImageQuant

LAS 4000 (GE Life Sciences). The CURT1 antibody was kindly provided by the group of Jörg Nickelsen (Heinz et al., 2016b).

Table 2-3 Antibody information

Antibody Name	Manufacturer	Dilution	Loading Amount (µg total protein)	Protein size (kDa)
Anti PsaB (rabbit)	Agrisera	1:1000	15	81.48
Anti PsbA1 (rabbit)	Agrisera	1:10000	15	39.97
Anti PsbD (rabbit)	Agrisera	1:5000	15	39.45
Anti PetC (rabbit)	Agrisera	1:5000	40	18.83
Anti AtpB (rabbit)	Agrisera	1:5000	25	51.7
Anti IsiA (rabbit)	Agrisera	1:1000	60	36.98
Anti RbcL (rabbit)	Agrisera	1:1000	30	52.45
Anti CURT1 (rabbit)	Homemade by Group of Jörg Nickelsen (Heinz, Rast et al. 2016)	1:1000	80	16.21
Goat anti-rabbit	Agrisera	1:10000	2nd antibody	2nd antibody

2.8 Blue native polyacrylamide gel electrophoresis

Thylakoid membranes were isolated and washed with washing buffer (330 mM sorbitol, 50 mM BisTris pH 7.0), then resuspended in a buffer containing 50% resuspension buffer (25 mM BisTris-HCl, 20% glycerol, 0.025% Pefabloc w/v, 10 mM $MgCl_2$, 4% DNase) and 50% of solubilisation buffer (25 mM BisTris-HCl, 20% glycerol, 0.025% Pefabloc w/v, 10 mM $MgCl_2$, 4% DNase, 3% n-Dodecyl-beta-Maltoside). Samples were incubated at 4 °C for 30 min for solubilisation and centrifuged at 18,000 g, 4°C for 15 min (Thermo Scientific™ Fresco™ 21 Microcentrifuge), the supernatant was mixed with 10% loading buffer (0.5% servaG, 0.5 M 6-amino-caproic acid, 50 mM

BisTris-HCl pH 7.0, 30% sucrose) and loaded onto 3–12% linear gradient blue native gels (Invitrogen, Nativepage).

2.9 Chlorophyll concentration

Chlorophyll concentration was measured with 1 mL of cyanobacterial culture suspension centrifuged at 15,000 g at room temperature for 7 min (Thermo Scientific™ Fresco™ 21 Microcentrifuge). The pellet was dissolved in 1 mL of methanol precooled at 4 °C and homogenised. Samples were covered with aluminium foil, incubated at 4 °C for 20 min to extract the pigments, then further centrifuged at 15,000 g, 4 °C for 7 min (Thermo Scientific™ Fresco™ 21 Microcentrifuge). Absorbance was measured by spectrophotometer at 665 nm and 720 nm. The concentration of chlorophyll-a was calculated according to equations: Chla (µg/mL)= 12.9447 ($A_{665} - A_{720}$), Chla (µM) = 14.4892 ($A_{665} - A_{720}$), with the molar mass of Chla molar mass estimated to be 893.4890 g/mol (Ritchie, 2006).

2.10 Room temperature absorption spectra

Syn7942 cells were sampled when the OD_{750} reached approximately 0.8. Whole-cell absorption spectra were measured at room temperature using a Cary UV-Vis Spectrophotometer (Agilent Technologies). The concentration of cells was adjusted to OD_{750}=1. The recorded spectra from 400 nm–800 nm were normalised against the absorbance at OD_{750}.

2.11 Room temperature fluorescence spectra

Syn7942 cells were sampled when the OD_{750} reached approximately 0.8. Whole-cell fluorescence emission spectra were measured at room temperature using a Varian Cary Eclipse Spectrofluorometer. The concentration of cells was adjusted to OD750=1.

Cells were excited at 430 nm (for chlorophyll-a excitation) and 580 nm (for phycobilisome excitation), respectively, with the excitation slit (nm) value set to 5. The recorded spectra from 600 nm–780 nm were normalised against the absorbance at OD_{760}.

2.12 Fv/Fm and rapid light curves

Syn7942 cells were sampled when the OD_{750} reached approximately 0.8. Cells were concentrated with a chlorophyll-a level of 20 μM. A total of 4 mL culture aliquots from three biological replications were dark-adapted for 10 min, and then the Fv/Fm and light curves were measured. The PSII activity (Fv/Fm) and light curves were measured with an AquaPen-C fluorometer (Photon Systems Instruments, Brno, Czech Republic) as previously described elsewhere (Cameron et al., 2013). Data were retrieved using the AquaPen-C software package.

2.13 Oxygen evolution and respiratory rates

Syn7942 cells were sampled when the OD_{750} reached approximately 0.8. Each experiment used one millilitre of culture, and the chlorophyll a concentration was adjusted to 20 μM. The oxygen evolution and respiratory rate measurements were carried out in an OXYLAB2 liquid-phase oxygen electrode (Hansatech). The liquid-phase chamber was kept at 30 °C with a circulating water system, and the samples were mixed constantly with a magnetic stirring bar. Prior to measurements, samples were dark-adapted for 2 min. Oxygen evolution was measured with a red LED light source peaking at 650 nm. Respiratory rates were measured in the dark. Data were recorded when the oxygen changing slope remained constant.

2.14 Mass spectrometry

Bound proteins and beads were resuspended in 50 µL of ammonium bicarbonate (AmBic) containing 0.05% Rapigest (w/v) and heated to 80°C for 10 min to facilitate the elution of GFP-labelled proteins and interactants. Cysteine reduction was performed by incubating with 5 µL of a 9.2 $mg \cdot mL^{-1}$ DTT solution at 60°C for 10 min. Subsequent alkylation was carried out by dark incubation with 5 µL of a 33 $\mu g \cdot mL^{-1}$ iodoacetamide for 30 min. In-solution digestion was carried out by incubating with 200 ng of trypsin and at 37°C overnight. The reaction was quenched by adding 0.5 µL of trifluoroacetic acid (TFA) at 37°C for 45 min. RapidGest degradation products and any insoluble material were removed by centrifugation at 16,000 g for 20 min at 4°C. Injected samples (10 µL for each) were analysed using an Ultimate™ 3000 RSLCnano system (Thermo Fisher Scientific, Hemel Hempstead) coupled with a Q Exactive™ HF mass spectrometer (Thermo Fisher Scientific, Hemel Hempstead). The samples were loaded onto a trapping column (Thermo Fisher Scientific, PepMap™ 100, C18, 300 µm × 5 mm) using partial loop injection for 7 min at a flow rate of 4 $\mu L \cdot min^{-1}$ with 0.1% (v/v) formic acid (FA). The samples were resolved on the analytical column (EASY-Spray™ C18 75 µm × 500 mm, particle size 2 µm column) using a gradient of 97% A (0.1% formic acid), 3% B (99.9% ACN, 0.1% formic acid) to 60% A, 40% B over 30 minutes at a flow rate of 300 $nL \cdot min^{-1}$. The data-dependent program used for data acquisition consisted of a 60,000 resolution full-scan MS scan (AGC set to $3e^6$ ions with a maximum fill time of 100 ms); the 10 most abundant peaks were selected for MS/MS using a 30,000 resolution scan (AGC set to $1e^4$ ions with a maximum fill time of 45 ms) with an ion selection window of 1.2 $m \cdot z^{-1}$ and normalised collision energy of 30. To avoid repeated selection of peptides for MS/MS, the program used a 20-second dynamic exclusion window.

Progenesis data analysis: The raw LC-MS files were analysed in Progenesis QI for Proteomics label-free analysis software which aligned the files and peak picks for quantification by peptide abundance. For the comparison, five groups were created (all groups; WT vs PSI; WT vs PSII; WT vs Cyt b_6f; WT vs ATPase) containing the respective replicate samples. The software first aligned the LC-MS files and peak picks the aligned peptides. An aggregate file was generated containing all the peaks from all runs in an experiment so that there were no missing values. At this stage, normalisation was performed using the “normalise against all proteins” option. The software assumed that most proteins were not changing in abundance, and normalisation factors were used to adjust peptide intensities.

The peptide list was exported into Peaks and MASCOT and was searched against the *S. elongatus* PCC 7942 Uniprot database (2,657 proteins), and was then manually searched against a small database containing the sequence of all subunits of photosynthetic complexes (with carbamidomethyl cysteine as a fixed modification and methionine oxidation as a variable mod). The peptide lists were imported back into Progenesis and assigned to features. Peptide matches in peaks were set to a 1% false discovery rate, and peptides were then filtered in Progenesis at the peptide cut-off threshold score for a 1% FDR.

2.15 Mass Spectrometry data analysis

Ratios of complexes involved in supercomplex formation were calculated by comparing the abundance of specific protein subunits between the GFP-labelled strain and other strains in which the specific subunits were not labelled with GFP, using GFP normalised data. Since the GFP abundance of these two groups has already been normalised, theoretically, the copy number of PSI in the PSI-GFP sample is approximately the same as the copy number of PSII in the PSII-GFP samples. If the

100% supercomplexes and 1:1 ratio hypotheses were valid, it would be approximately equal to the copy number of PSI in the PSII-GFP sample. For example, if 100% PSII formed stable supercomplexes with PSI with a ratio of 1:1, the abundance of PSI in the GFP–PSII sample would be similar to the abundance of PSI in the PSI-GFP sample. As mentioned in the result section, the quantities of PSI, PSII, Cyt b_6f and ATPase were presented by the sums of the scores of all observed protein subunits. Then, the sums of value were used to carry on the subsequent ratio calculation. For example, the ratio of PSII that forms supercomplex with PSI was calculated by the sum of PSI subunits' abundance in the PSII-GFP sample divided by the sum of PSI subunits' abundance in the PSI-GFP group. Student's *t*-test was deployed to determine if there was a significant difference between the means of the two samples.

To probe the interacting protein subunits that associate with the GFP-labelled complex, the relative abundance of each subunit was calculated by determining the ratio of the abundance score of the same subunit in a specific sample to that in the sample in which GFP was labelled to the photosynthetic complex that this subunit belongs to, e.g. to determine if PsaA is the interacting subunit in PSI with PSII, PsaA in the PSII-GFP pull-down sample was divided by PsaA in the PSI-GFP sample. Subsequently, statistical analysis was performed using Student's *t*-test to compare the ratio of each subunit with the ratios of other subunits within the same photosynthetic complexes in the same pull-down sample. For example, the ratio of PsaA was compared with those of PsaB, PsaC, PsaD, PsaE, PsaF, PsaJ, PsaK and PsaL as a whole.

2.16 Transmission electron microscopy

Cells were harvested when they reached OD_{750} = 0.8 in liquid BG-11 medium until the culture reached an OD750 of 1. Pellets were washed three times in electron microscopy buffer (0.05 M $(CH_3)_2$ AsO_2H buffer pH = 7.2). Samples were then fixed in

2% glutaraldehyde and 2% paraformaldehyde in EM buffer for 60 min and subsequently post-fixed with 1% osmium tetroxide for 1.5 h and dehydrated with a gradient of ethanol solutions (30%, 60%, 70%, 80%, and 100%). After dehydration, samples were embedded in Transmit EM resin (TAAB Laboratories Equipment, UK) as acetone/Transmit EM resin (1:1) for 20 min and acetone/Transmit EM resin (1:2) for 4 h). After incubation of 6 hours, the pure Transmit was changed three times, and the samples went through polymerisation for 48 h at 70 °C. Thin sections of 70 nm were done with a diamond knife (Diatome 45° ultra, Agar Scientific) and post-stained with 4% uranyl acetate and 3% lead citrate. Images were acquired with an FEI Tecnai G2 Spirit BioTWIN transmission electron microscope.

2.17 Atomic force microscopy

For AFM imaging on pull-down samples, two microlitres of protein samples were adsorbed onto freshly cleaved mica surface with 38 µL of adsorption buffer (10 mM Tris–HCl pH 7.5, 150 mM KCl, 25 mM $MgCl_2$) at room temperature for 1 h. After adsorption, the sample was carefully rinsed with 800 µL imaging buffer (10 mM Tris–HCl pH 7.5, 150 mM KCl). These buffers could ensure the electrostatically balanced interactions between AFM tip and biological samples and thereby high-resolution AFM topographs in an aqueous solution (Müller et al., 1999, Miller et al., 2020a, Liu et al., 2011b, Liu et al., 2011a, Liu et al., 2009b, Casella et al., 2017). AFM imaging was performed in ScanAsyst Air mode in the air at room temperature using a Multimode Nanoscope VIII AFM (Bruker) equipped with a J-scanner and ScanAsyst-Air-HR (0.4 N m^{-1}, Bruker) at a scan frequency of 1 Hz using optimised feedback parameters and a resolution of 512 × 512 pixels. Images were processed with NanoScope Analysis software (Bruker).

For AFM imaging on native thylakoid membranes, crude thylakoid membrane fractions were further purified using a step sucrose gradient (2.0 M, 1.3 M, 1.0 M, 0.5 M) in 50 mM MES-NaOH pH 6.5, 5 mM $CaCl_2$ and 10 mM $MgCl_2$, and were centrifuged at 36,200 rpm in Beckman RPS40 rotor for 1 h at 4°C, as reported previously (Zhao et al., 2020, Casella et al., 2017). The Chl-enriched samples were collected and characterised by high-resolution AFM imaging in liquid at room temperature in AC imaging mode using a NanoWizard 3 AFM (JPK) using Ultra-Short Cantilever probes (0.3 MHz, 0.3 $N \cdot m^{-1}$, NanoWorld) with optimised feedback parameters and a resolution of 512 × 512 pixels (Zhao et al., 2020). Images were processed with JPK SPM Data Processing (JPK) and ImageJ (Schneider et al., 2012). No detergent was added during membrane isolation and AFM imaging to ensure the physiological organisation of isolated thylakoid membranes (Liu et al., 2013).

2.18 Confocal Microscopy

For confocal microscopy, *S. elongatus* PCC 7942 cells from exponentially growing cultures in liquid BG-11 medium were immobilised on a thin film of 1.5% agarose in BG-11 medium and settled for 15 min in air. A 1 cm × 1 cm agar was then excised and placed on a 0.17 mm cover glass. The Petri dishes were covered in aluminium foil during the preparation to avoid photobleaching. All imaging processes took place at 30°C. Images were acquired on a Zeiss LSM710 or LSM780 inverted confocal microscope, using a 100x oil-immersion objective and a 2-μm pinhole. An Argon laser with an excitation wavelength of 488 nm was used for GFP characterisation. Emission was simultaneously detected at 500–520 nm and 670–720 nm for GFP and chlorophyll fluorescence. For CFP and YFP colocalisation, an Argon laser with an excitation wavelength of 458 nm was used for CFP detection at 470–500 nm, and a 514 nm laser was used to excite YFP detected at 520–550 nm. All images were captured using Zen 2010 with all pixels below saturation.

2.19 Image analysis

ImageJ was employed to perform image data analysis. When it was used to quantify the abundance of certain proteins from pictures of Western Blot membranes (Rumbaugh and Miller, 2010), pictures were inverted in ImageJ, the measurements were set to integrated density, and the scale was set to pixel, the background was subtracted with a rolling ball radius of 50 pixels. The integrated density of each band was used for quantification and comparison.

For the measurements of the distance between thylakoid membrane layers, the images were firstly inverted, a plot profile was created for the selected thylakoid membrane, and the distance between the vertices of grey value was measured. Each cell was measured at 3 or 4 spots to avoid bias.

For distribution analysis and fluorescence quantification, thylakoid membranes of cells were selected, and a plot file was generated. The selection started from the midpoint of the thylakoid membranes on one side and continued around the whole cell. Fluorescence intensity was plotted against distance, and then the plot data were extracted and analysed. The standard deviation of fluorescence intensity was calculated and normalised against the mean for heterogeneity characterisation. The CFP and YFP of the same location were plotted for colocalisation, and regression analyses were carried out.

2.20 Regression analysis

The Pearson correlation coefficient was calculated using this formula.

$$r_{xy} = \frac{\sum x_i y_i - n\bar{x}\bar{y}}{(n-1)s_x s_y} = \frac{n\sum x_i y_i - \sum x_i \sum y_i}{\sqrt{n\sum x_i^2 - (\sum x_i)^2}\sqrt{n\sum y_i^2 - (\sum y_i)^2}}$$

Where r_{xy} is the Pearson correlation coefficient; x_i and y_i are the measured values, in this case, CFP intensity and YFP intensity, respectively; $\bar{x}$ is the arithmetic mean of all x_i, the same is true for y; s_x and s_y are the standard deviations of x and y; n denotes the number of data points taken.

The t value was calculated using the following formula.

$$t = \frac{r_{xy}\sqrt{n-2}}{\sqrt{1-r_{xy}^2}}$$

The significance test was done with a two-tailed Student's T distribution, where the degrees of freedom = n - 2.

Fisher's r to z transformation was applied to transform the Pearson correlation coefficient r to z so that it becomes normally distributed. The formula to calculate z is:

$$z = \frac{1}{2}\ln\left(\frac{1+r}{1-r}\right) = \operatorname{arctanh}(r)$$

And the standard deviation is

$$\mathrm{s_z} = \frac{1}{\sqrt{N-3}}$$

The significance analysis was carried out as normally distributed data.

2.21 Heterologous protein expression and purification

All *E. coli* cells were cultured in Lysogeny Broth (LB broth). The full-length wild-type CURT1 gene (Syn7942_1832) was amplified and ligated with an N-terminal Hexa-his tag in the pETDuet vector. This expression plasmid was transformed into BL21 (DE3) *E. coli* by heat shock. Cells were cultured in media with 100 µg/mL of ampicillin. Thirty millilitres of overnight culture was added into 3 L of fresh LB broth and incubated at 37 ºC in a shaker with 160 rpm until the optical density OD_{600} reached 0.6–0.8. IPTG was added to a final concentration of 0.5 mM to induce protein expression, and the cultures were kept at 37 ºC overnight.

Cells were harvested and resuspended in PBS buffer (8 g/L NaCl, 0.2 g/L KCl, 1.44 g/L Na_2HPO_4, 0.24 g/L KH_2PO_4, pH 7.4). They were subsequently broken by disrupting in a French Press (Stansted Fluid Power, UK) at 110 kPa 6 times, and debris was removed by centrifugation at 3,000 g, 4 °C for 10 min (Sorvall, SS-34 rotor). Further centrifugation at 100,000 g, 4 °C, 30 min (Sorvall, SS-34 rotor) was done twice to separate membranes and cytoplasm.

Protein purification was done in ÄKTA pure protein purification system (GE Healthcare Life Sciences). Since CURT1 exist mainly in the cytoplasm, the supernatant was collected, and a final concentration of 1.5% β-DDM was added. This sample firstly went through a HisTrap™ High Performance Column (GE Healthcare), with the binding buffer as 30 mM imidazole, 0.03% β-DDM in PBS buffer, and the elution buffer as 500 mM imidazole, 0.03% β-DDM in PBS buffer. Protein was eluted using a 0–100% elution buffer gradient. Fractions were collected and examined with SDS-PAGE, and then the fractions with the purest CURT1 were purified once more with Sephacryl High

Resolution size exclusion chromatography resins (GE Healthcare). Peaks around the correct elution time were collected and analysed.

The long-term storage of strains was achieved by mixing cells with 25% glycerol as a cryoprotectant, snap freezing with liquid nitrogen, and keeping them at -80 °C.

2.22 Protein crystallisation screening

The protein concentration of CURT1 for crystallisation was 7.288 mg/mL in PBS buffer with 0.03% β-DDM. The crystallisation screening was carried out in five commercial crystallisation trays—Structure, RUBIC, Memgold, Memtrans, and Morpheus. The protein and buffers were dispensed and mixed using Innovadyne Screemaker 96+8. Trays were kept at room temperature and monitored every month.

After the observation of crystallisation formation under one condition (Structure C9: 0.2 M magnesium chloride hexahydrate, 0.1 M Tris, pH 8.5, 30% w/v PEG 4000) during the crystallisation screening, further screening was conducted with manual trays. Different PEG concentrations (5%, 10%, 15%, 20%, 25%, 30%, 35%, 40%, 42.5%), pH values (7.5, 8, 8.5, 9) and protein concentrations (5 mg/mL, 7.288 mg/mL and 9.508 mg/mL) were screened.

2.23 Circular dichroism

Circular dichroism data were acquired with pure CURT1 (7.288 mg/mL) in PBS buffer with 0.03% β-DDM using J-1100 Circular Dichroism Spectrophotometer (JASCO), with a detector PM-539 at 20 °C. The circular dichroism data of CURT1 were searched against the DichroWeb database (Lobley et al., 2002, Whitmore and Wallace, 2004, Whitmore and Wallace, 2008) using CONTINLL algorithms (Provencher and Gloeckner, 1981, Van Stokkum et al., 1990).

2.24 Structure modelling

The structure modelling was performed with the hierarchical protein structure prediction server I-TASSER (Yang et al., 2015, Roy et al., 2010, Zhang, 2008). The confidence score was calculated with the I-TASSER server. Colouring of residues with different hydrophobicity was done in Pymol with the Color h script (Eisenberg et al., 1984).

3 Chapter 3 Characterising the supercomplex association of photosynthetic complexes in cyanobacteria

3.1 Introduction

Photosynthesis is the natural process conducted by plants, algae and cyanobacteria to transform light energy into chemical energy to drive the biochemistry of life on Earth. The estimated average rate of photosynthesis of the whole biosphere is approximately equivalent to a power of 130 terawatts years per year (Steger et al., 2005), which is around three times the energy consumed by human civilisation (Consumption, 2008). Photosynthesis is performed in two steps: light-dependent and light-independent reactions. In most cyanobacteria, light-dependent reactions of photosynthesis occur in the specialised intracellular membranes termed thylakoid membranes. Unlike the thylakoid membranes of higher plants, cyanobacterial thylakoids are not differentiated into grana and stroma regions; instead, they generally form stacks of membrane layers that sit between the cytoplasmic membrane and central cytoplasm (Liu, 2016, Mullineaux and Liu, 2020).

A unique feature of the cyanobacterial thylakoid membrane is that it provides a membrane platform accommodating both photosynthetic and respiratory electron transfer chains (Mullineaux and Liu, 2020, Casella et al., 2017). The physiological functions and coordination of electron transport components are fundamental for efficient electron flow and bioenergetic modulation, enabling cyanobacterial cells to thrive in distinct ecological niches. Over the past decades, the atomic structures of the major photosynthetic membrane complexes from cyanobacteria have been resolved, including PSI (Jordan et al., 2001, Toporik et al., 2019, Cao et al., 2020), PSII (Zouni et al., 2001, Kamiya and Shen, 2003, Ferreira et al., 2004), cytochrome b_6f (Cyt b_6f) (Kurisu et al., 2003, Stroebel et al., 2003), ATP synthase (ATPase) (Abrahams et al., 1994, Groth and Pohl, 2001) and photosynthetic Complex I—NAD(P)H dehydrogenase (NDH-1) (Schuller et al., 2019, Laughlin et al., 2019, Pan et al., 2020, Zhang et al., 2020, Schuller et al., 2020). These studies have provided structural insights into electron transport mechanisms within individual bioenergetic complexes.

Studies on cyanobacteria, algae and plants stated that supercomplexes could form among photosynthetic and respiratory protein complexes. It was demonstrated that in *Synechocystis* sp. PCC 6803, phycobilisomes (PBS), PSI and PSII could form a megacomplexes with each other by interactions that occurred between PBS–PSII and PBS–PSI, while Cyt b_6f was deduced to be out of this megacomplexes (Liu et al., 2013). Another study claimed that besides PSII, PBS was associated with PSI via a connecting component in *Anabaena* sp. PCC 7120 (Watanabe et al., 2014). Studies showed that the association of the PSII assembly factors Psb27 and Psb28 with the PSI–PSII supercomplexes might indicate PSI's involvement in PSII biogenesis (Bečková et al., 2017). For the green alga *Chlamydomonas reinhardtii*, it was stated that the PSI–light-harvesting complex, the PSII–light-harvesting complex, the Cyt b_6f complex and ferredoxin (Fd)–NADPH oxidoreductase formed a supercomplex (Iwai et al., 2010). *Chlamydomonas* sp. UWO 241 produced a 1,000-kD pigment–protein supercomplex that contains PSI and the Cyt b_6f complex; the phosphorylation status of its associated proteins—two PsbP-like polypeptides and an ATP-dependent zinc metalloprotease FtsH helped to regulate between linear and cyclic electron transport (Szyszka-Mroz et al., 2015). NDH-1 was stated to form supercomplex with PSI in the species in barley (*Hordeum vulgare*), which was confirmed by electron microscopy analysis (Kouřil et al., 2014). Blue-native PAGE and subsequent immunoblotting and mass spectrometry analyses of the strain *Synechocystis* sp. PCC 6803 showed the existence of NDH-1L–CpcG2–PSI supercomplexes (Gao et al., 2016). Recent atomic force microscopy (AFM) observations have explicitly revealed the strong lateral associations of different photosynthetic complexes in cyanobacterial thylakoid membranes of Syn7942 (Zhao et al., 2020). The structural and functional associations of different photosynthetic complexes in the thylakoid membrane are crucial for efficient electron transport between complexes. Further studies on the composition and dynamics of the thylakoid membranes will benefit the regulation of photosynthesis and respiration by the optimising electron transport pathways. They may help towards the goal of engineering artificial photosynthetic membranes or novel organisms for biofuel production.

Despite the substantial studies, understanding how photosynthetic complexes interact and cooperate with others to fulfil efficient electron transport is still rudimentary. The inherent challenges are the organisational heterogeneity and dynamics of electron transport chains in cyanobacterial thylakoid membranes, suggesting the transient and flexible interactions between different photosynthetic membrane complexes (Zhao et al., 2020, Mullineaux and Liu, 2020, Liu et al., 2012). This thesis describes an approach that combined immunoprecipitation, mass spectrometry, and AFM to identify the interactions between photosynthetic complexes in thylakoid membranes from a model cyanobacterium *S. elongatus* PCC 7942 (Syn7942), and the specific binding sites involved in inter-complex associations. The results provided insights into the structural interconnections of electron transport complexes in thylakoid membranes, which are pivotal for photosynthetic electron flow and regulation.

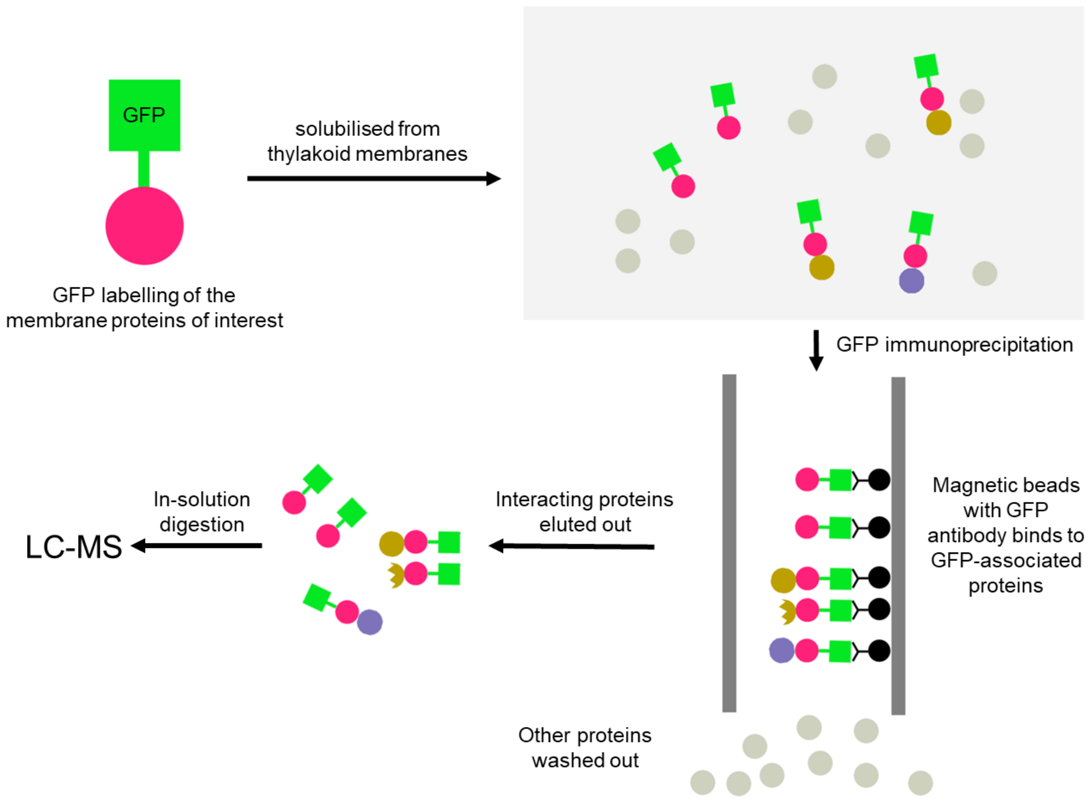

Figure 3-1 Overview of GFP immunoprecipitation methodology.

Crude thylakoid membranes from GFP-labelled PSI, PSII, Cyt b_6f, ATPase and WT strains were prepared by centrifugation and were solubilised by 1% digitonin. Proteins that interact with GFP-labelled proteins are immunoprecipitated with the GFP pull-down assay and subjected to mass spectrometric analysis. Triplicated experiments were conducted for each strain.

3.2 Results and Discussion

3.2.1 Optimisation of pull-down assays

In a previous study, PSI, PSII, Cyt b_6f and ATPase were tagged individually with the enhanced green fluorescent protein (GFP) to visualise the localisation of photosynthetic complexes in Syn7942 (Casella et al., 2017). The subunits labelled with GFP were PsaE for PSI, PsbB (CP47) for PSII, PetA for Cyt b_6f and AtpB (β) for ATPase. To study the inter-complex assembly of photosynthetic complexes in thylakoid membranes, thylakoid membranes from these Syn7942 strains were isolated and solubilised using digitonin at the optimised 1% (see Materials and Methods). The membrane-bound protein complexes tagged with GFP and their associated proteins/complexes were purified using GFP pull-down assays (Kimple et al., 2013, Strašková et al., 2018, Neumüller et al., 2012) (Figure 3-1).

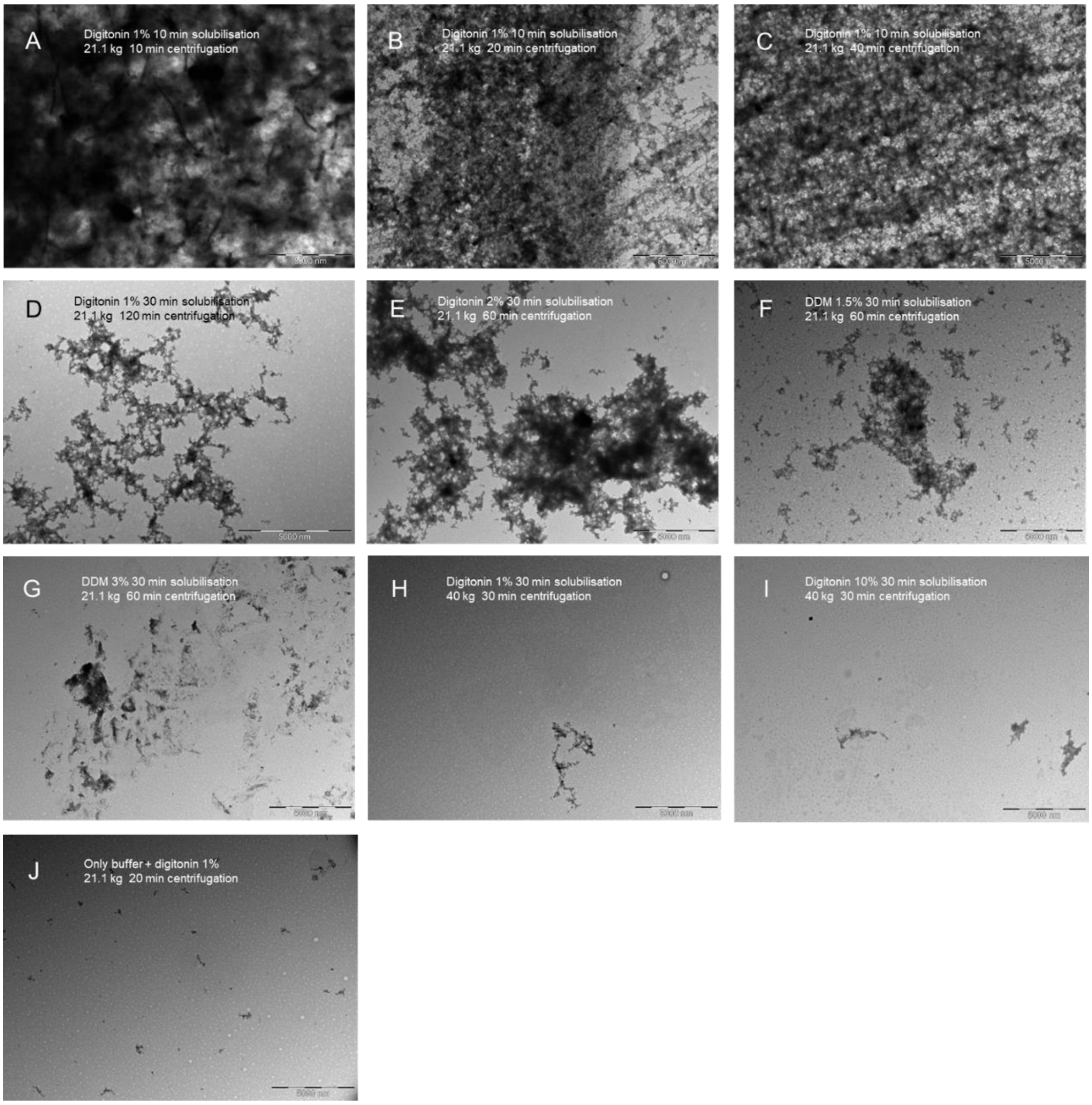

Figure 3-2 Optimisation for isolating membrane complexes by adjusting solubilisation and centrifugation conditions, imaged with transmission electron microscopy.

(A) Digitonin 1%, 10 min solubilisation and 21100g, 10 min centrifugation.

(B) Digitonin 1%, 10 min solubilisation and 21100g, 20 min centrifugation.

(C) Digitonin 1%, 10 min solubilisation and 21100g, 40 min centrifugation.

(D) Digitonin 1%, 30 min solubilisation and 21100g,120 min centrifugation.

(E) Digitonin 2%, 30 min solubilisation and 21100g, 60 min centrifugation.

(F) DDM 1.5%, 30 min solubilisation and 21100g, 60 min centrifugation.

(G) DDM 3%, 30 min solubilisation, 21100g, 60 min centrifugation.

(H) Digitonin 1%, 30 min solubilisation, 40000g, 30 min centrifugation.

(I) Digitonin 10%, 30 min solubilisation, 40000g, 30 min centrifugation.

(J) Only buffer with digitonin 1%, 21100g, 20 min centrifugation.

As the pre-experiment with an old protocol resulted in many shared protein subunits pulled down between all GFP-labelled samples, it was suspected the thylakoid complex isolation was contaminated with insolubilised membrane patches. Therefore, a series of experiments were carried out to optimise the conditions to isolate complexes from thylakoid membranes (Figure 3-2). A combination of different detergents—digitonin and n-Dodecyl β-D-maltoside (DDM), different detergent concentration (1–10%), different solubilisation time (10–30 min), different centrifugation force (21100g–40000g) and centrifugation time (10–120 min) were tested, and the isolated samples were examined with transmission electron microscopy (Figure 3-2). Results indicated that solubilisation with 1% digitonin for 30 min followed by 30 min centrifugation at 40000g removed almost all membrane debris except for very rare impurity (Figure 3-2H); and it used a reasonable concentration of digitonin compared to Figure 3-2I. This procedure followed by an additional centrifugation at 21100g for 20 min was employed as the method used in this study.

3.2.2 AFM topology of isolated thylakoid membrane proteins

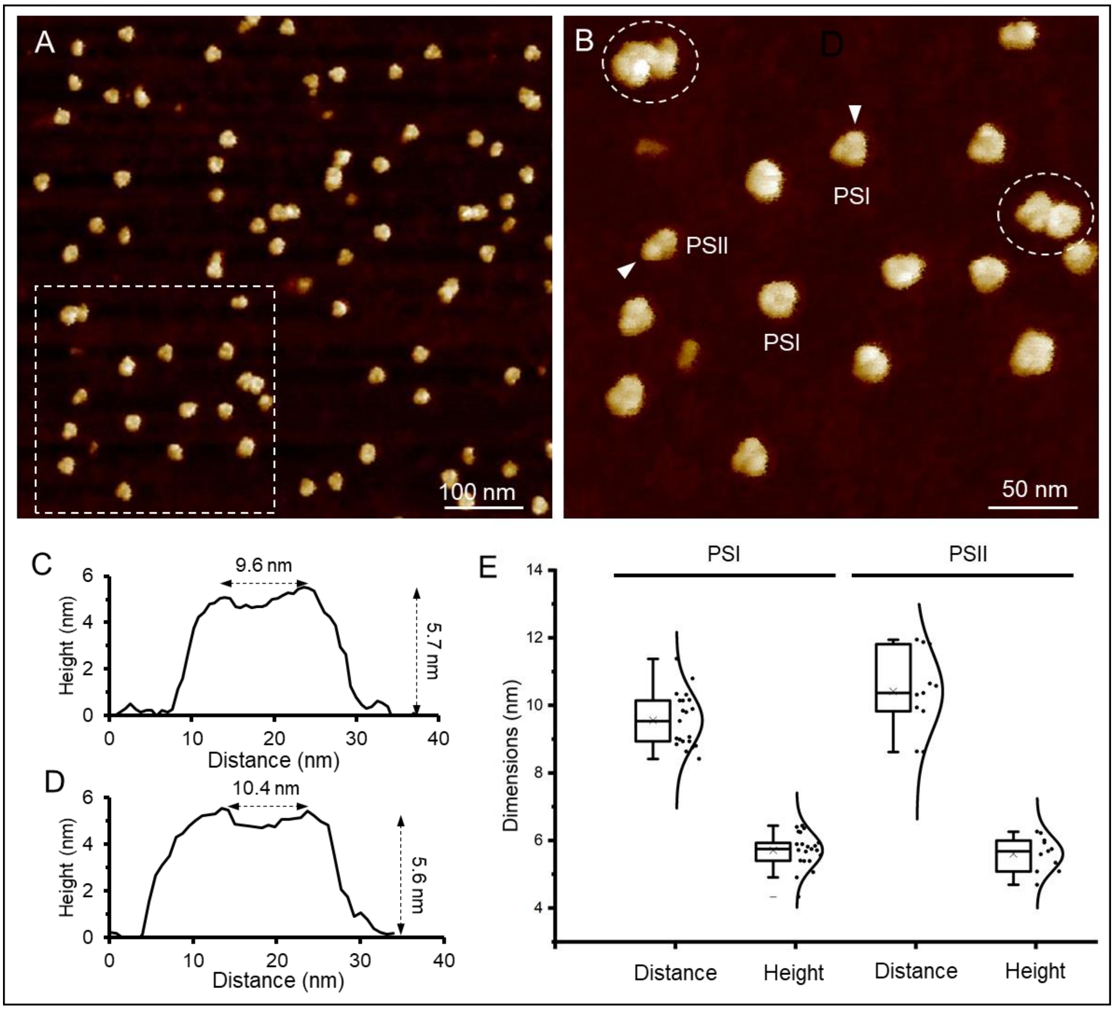

Figure 3-3 AFM imaging of isolated thylakoid membrane complexes from S. elongatus PCC 7942.

(A) Overview AFM image of isolated thylakoid membrane complexes after 1% digitonin membrane solubilisation.

(B) Closer-up AFM image of isolated thylakoid membrane complexes including PSI, PSII and supercomplexes (circles) from (A).

(C) Cross-section profile analysis of the PSI trimer shown in B along the arrow direction.

(D) Cross-section profile analysis of the PSII dimer shown in B along the arrow direction.

(E) Measurement of the vertex distances and heights of assigned PSI and PSII complexes in AFM. The PSI trimer has a height of 5.7 ± 0.5 nm and a distance of 9.6 ± 0.8 nm between its two vertices (n = 21). The PSII dimer exhibits a height of 5.6 ± 0.5 nm and a vertex distance of 10.4 ± 1.16 nm between two protrusions (n = 11).

The resulting protein mixtures were characterised by atomic force microscopy (AFM). AFM revealed that the protein complexes appeared as individual complexes or small assemblies instead of forming large aggregates and membrane fragments (Figure 3-3A, 3-3B). PSI trimers could be readily recognised by AFM, with a height of 5.7 ± 0.5 nm (n = 21) and a distance of 9.6 ± 0.8 nm (n = 21) between its two vertices (Figure 3-3C, 3-3E), consistent with previous studies (Casella et al., 2017, Zhao et al., 2020). The dimeric structures, putatively PSII dimers, possessed a height of 5.6 ± 0.5 nm (n = 11) and a vertex distance of 10.4 ± 1.16 nm (n = 11) between two protrusions (Figure 3-3D, 3-3E). Complex assemblies were often discerned by AFM (Figure 3-3A, 3-3B, white circles), allowing for exploring the interactions of different photosynthetic supercomplexes. However, from AFM, it is difficult to make an absolute proposal about the participant in those interactions. Only a small fraction of thylakoid membrane complexes formed supercomplexes or were located in the proximity of each other, indicating that either the interactions only take place between a few protein complexes, or the formation of supercomplex is transient, in agreement with some previous research regarding supercomplexes (Liu et al., 2013, Watanabe et al., 2014).

3.2.3 Protein interactions among photosynthetic complexes indicated by SDS-PAGE

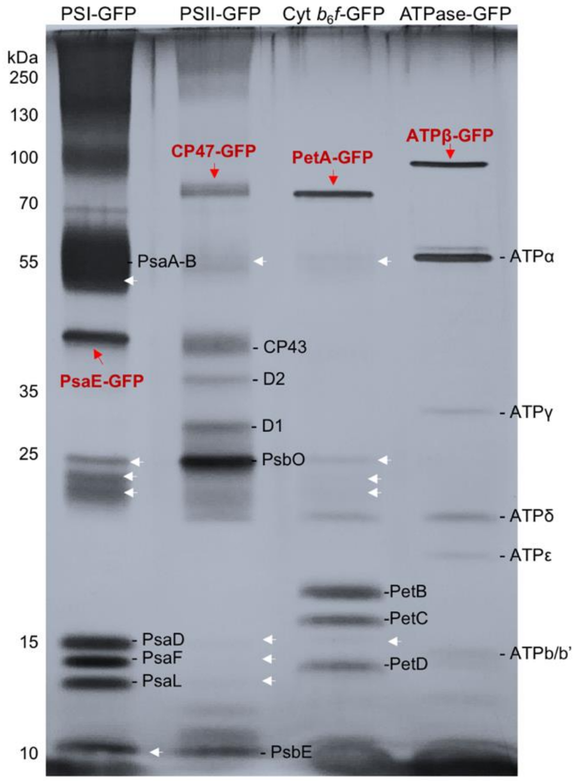

Figure 3-4 SDS-PAGE analysis of the pull-down samples, revealing the subunit composition of GFP-tagged protein complexes and interacting proteins.

Black lines indicate the designated subunits in individual complexes. Red arrows indicate the corresponding subunits tagged with GFP in individual complexes. White arrows indicate the potential interacting proteins to the corresponding GFP-tagged complexes.

SDS-PAGE revealed that the GFP-labelled complexes were unambiguously present at a great abundance in each pull-down sample (Figure 3-4). With the fusion of enhanced GFP, the PsaE, PsbB, PetA, and AtpB bands were up-shifted. It was shown that the PSI and PSII pull-down samples shared some common subunits in the SDS-PAGE. Closer inspection showed that the PSI and PSII pull-down samples included several same proteins, e.g. PsaA, PsaB, PsaD, PsaF, PsaL, CP47 and PsbO. Some of these subunits were also found in the Cyt b_6f pull-down samples. In addition, the putative NDH-1 subunits NdhK and NdhL were also present in both PSI and Cyt b_6f pull-down samples. Overall, the presence of subunits from unlabelled complexes in the GFP-labelled sample indicated the specific association between photosynthetic complexes and, potentially, the formation of supercomplexes.

3.2.4 Mass spectrometry reveals the physical associations of photosynthetic complexes

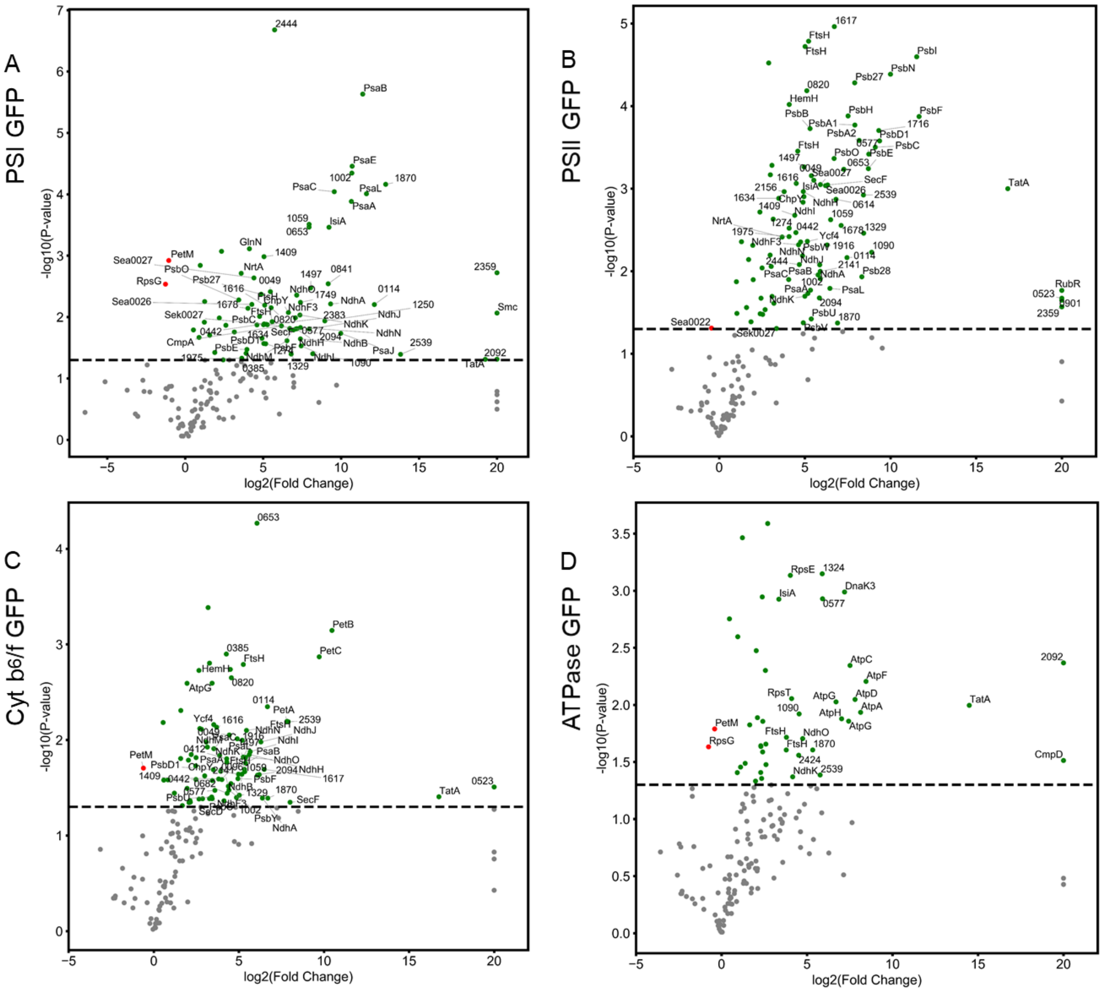

Figure 3-5 Proteins identified by mass spectrometry and comparisons with the WT control.

Proteins in the pull-down samples from PSI-GFP (A), PSII-GFP (B), Cyt b_6f-GFP (C) and ATPase-GFP (D) are compared with the WT control plotted according to their statistical log10 P-value (y-axis) and their relative abundance ratio (log2 fold change). Compared to the WT, proteins that are more abundant in the pull-down samples are coloured in green, and those that are significantly less in the pull-down samples are shown in red. Proteins with more than 20-fold change are labelled with their gene names. Grey dots below the lines (corresponding to P = 0.05) are proteins with no significant difference.

To determine the presence and abundance of protein subunits in the pull-down samples, label-free mass spectrometry and relative quantification were applied. The peak search was conducted within the *S. elongatus* PCC 7942 Uniprot database. A total of 180 protein subunits were detected, of which 38 subunits belong to the four photosynthetic complexes. The GFP abundance varied among the GFP-labelled PSI, PSII, Cyt b$_6$f and ATPase pull-down samples. The GFP abundance was the highest in the PSI pull-down sample, followed by those in the PSII, Cyt b$_6$f and then the ATPase pull-down samples. The variation was consistent with the variation of the content of photosynthetic complexes in Syn7942 as reported previously (Casella et al., 2017). For comparison, the abundance of individual protein subunits was normalised against GFP content in each sample. As a negative control, most of the subunits exhibited a notably low abundance in the WT sample, implicating the specificity of GFP immunoprecipitation (Figure 3-5, green dots).

3.2.5 Percentage of complexes involved in supercomplex formation

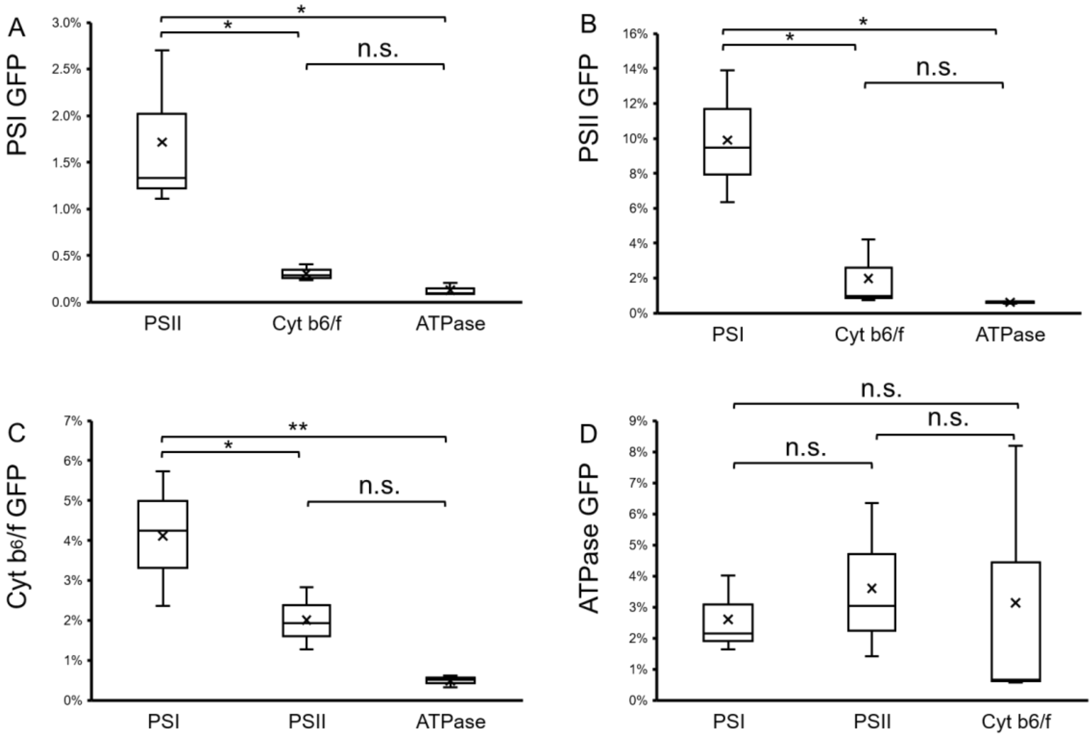

Figure 3-6 Ratios of complexes that tend to associate with other complexes.

After normalizing protein content by the GFP content in individual pull-down samples, the percentages of the photosynthetic complexes that associate with other complexes were calculated by dividing the sum of the subunit abundance of a specific photosynthetic complex detected in the pull-down samples for another GFP-labelled complex with the sum of the abundance of the same photosynthetic complex from its corresponding GFP-labelled pull-down sample. For example, the ratio of PSII that associate with PSI is determined by the abundance of PSII in the PSI-GFP pull-down sample divided by the PSII content in the PSII-GFP pull-down sample. The results showed that PSI and PSII possess a higher preference to form supercomplexes than others (1.72% PSI are associated with PSII, n = 3; 9.9% PSII are associated with PSI, n = 3) (A, B). Cyt b_6f has a higher preference to bind with PSI (4.1%, n = 3) than PSII (2.0%, n = 3) (C). All PSI, PSII and Cyt b_6f have a low preference to interact with ATPases, while ATPases exhibit relatively similar tendencies to associate with the other three complexes (D). Box plots display the median (line), the average (cross), the interquartile range (box), and the maximum and minimum (whiskers). Statistical analysis was performed using Student's t-test. *: $0.01 < P < 0.05$; **: $0.001 < P < 0.01$; ns, not significant.

As the photosynthetic complexes PSI, PSII, Cyt b_6f and ATPase are multi-subunit complexes, this study calculated the sum of the abundance of all the protein subunits in one specific complex to represent the quantity of this complex (Perkins et al., 1999). Assuming 100% PSII form stable supercomplexes with PSI with a ratio of 1:1, the abundance of PSI in the GFP–PSII sample would have been identical to the abundance of PSI in the GFP–PSI sample. However, not all PSII form supercomplexes with PSI in reality. For example, the ratio of PSII that form supercomplexes with PSI was calculated by the sum of PSI subunits' abundance in the PSII-GFP sample divided by the sum of PSI subunits' abundance in the PSI-GFP group.

Although some complex-complex associations are likely to disassemble during purification due to their weak inter-complex interactions, the result showed that PSI and PSII had a stronger preference to form supercomplexes (Figure 3-6). Around 1.7% of PSI were associated with PSII (Figure 3-6A), whereas 9.9% of PSII strongly interacted with PSI (Figure 3-6B), presumably owing to a high PSI/PSII ratio of 4.5 in Syn7942 (Casella et al., 2017). AFM imaging on thylakoid membranes from Syn7942 confirmed that a large amount of PSI associated tightly with each other to form PSI enriched membrane regions (Zhao et al., 2020). Around 4.1% Cyt b_6f tended to bind with PSI which accounted for 0.3% of the total PSI, whereas 2.0% Cyt b_6f were associated with PSII complexes that were 1.98% of the total PSII (Figure 3-6C). These results support the supercomplex formation between PSI and PSII (Liu et al., 2013) and between photosystems and Cyt b_6f (Iwai et al., 2010). PSI, PSII and Cyt b_6f all showed a low preference to interact with ATPases, while ATPases exhibited relatively similar tendencies to associate with the other three complexes (Figure 3-6D).

3.2.6 The binding sites of photosynthetic complexes

By determining the relative abundance of peptides that associate with the GFP-labelled protein subunits, this study also evaluated the inter-complex interactions and the binding sites of complex assemblies. The relative abundance of each protein subunit was determined by dividing the abundance of this subunit in a sample by that of the same protein subunit in the GFP-labelled pull-down sample (see methodology, mass spectrometry data analysis). Subsequently, the relative abundance of individual subunits was compared with other subunits in the same protein complex (Figure 3-7).

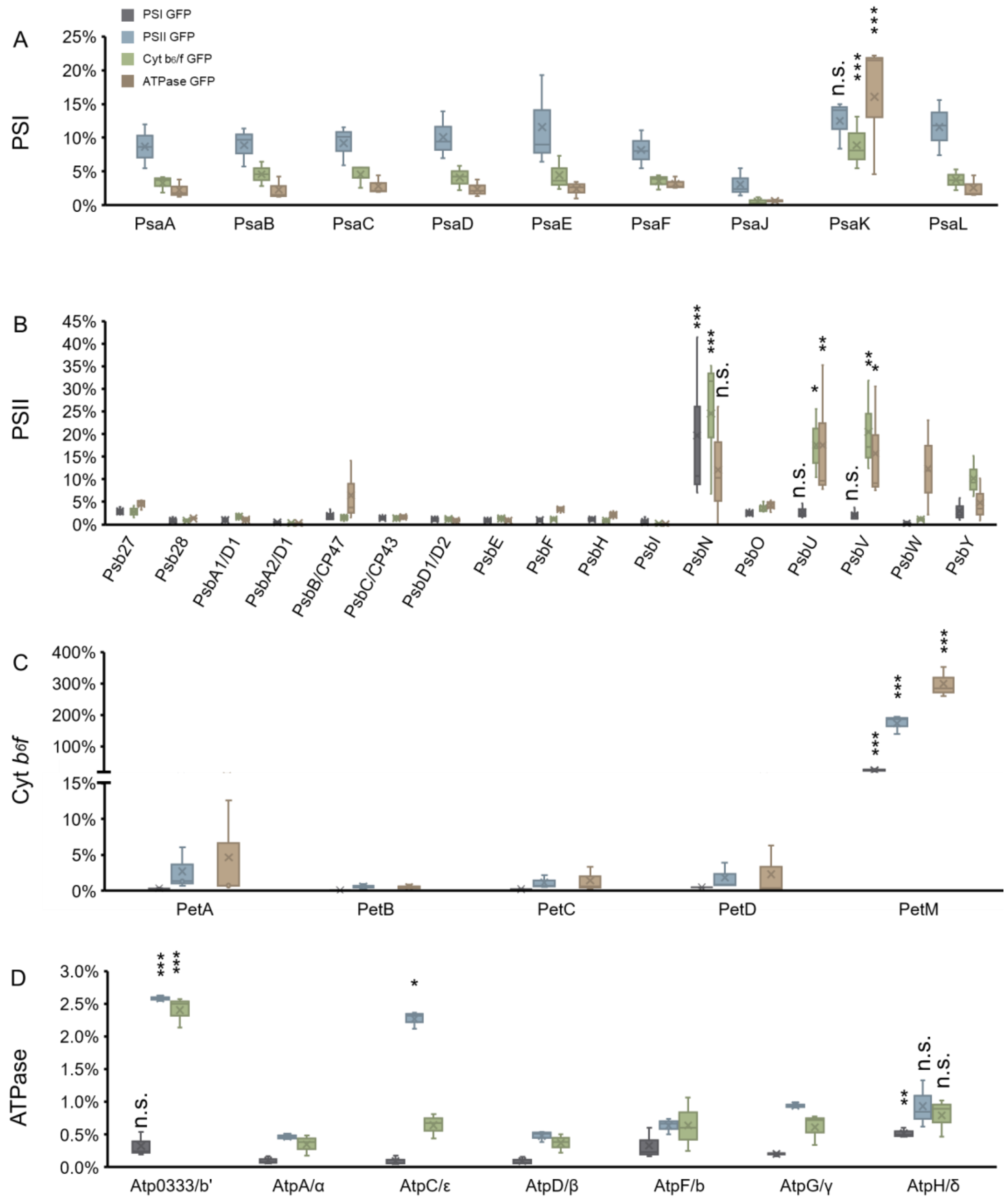

Figure 3-7 Ratios of individual subunits in the corresponding photosynthetic complexes involved in inter-complex associations.

The analysis calculated the ratio of PSI (A), PSII (B), Cyt b_6f (C) and ATPase (D) subunits. The relative abundance of each subunit was calculated by determining the ratio of the abundance score of the same subunit in a specific sample to that in the sample in which GFP was labelled to the photosynthetic complex that this subunit belongs to. Statistical analysis was performed using Student's t-test to compare the ratio of each subunit with the ratios of other subunits within the same photosynthetic complexes in the same pull-down sample. *: $0.01 < P < 0.05$; **: $0.001 < P < 0.01$; ns, not significant. Box plots display the median (line), the average (cross), the interquartile range (box), and the maximum and minimum (whiskers).

Among the PSI subunits, the peripheral subunit PsaK showed a greater relative abundance than other subunits in the PSII, Cyt b_6f and ATPase-GFP pull-down samples, suggesting that PsaK might be the primary binding site of PSI to other photosynthetic complexes (Figure 3-7A). Consistently, PsaK has been found to be involved in PSI−IsiA binding in Syn7942 under iron-stressed conditions (Cao et al., 2020) and Lhca3/Lhca2 binding in *Arabidopsis* (Jensen et al., 2000). Among the PSII subunits, PsbU, PsbV and PsbN showed a higher abundance in other samples than in the PSII-GFP sample (Figure 3-7B). PsbU and PsbV are close to each other and are both extrinsic components of PSII on the lumen side of the thylakoid membrane. They might not have direct interactions with PSI, but the associations with other photosynthetic complexes presumably have impacts on the binding of PsbU and PsbV to PSII, which is important for the regulation of PSII stability and energy transfer (Shen et al., 1998, Veerman et al., 2005, Xiao et al., 2020). PsbN has not yet been identified in the existing PSII structure (Umena et al., 2011, Hellmich et al., 2014); in tobacco, PsbN is not a constituent subunit of PSII but is involved in repair from photoinhibition and assembly of the PSII reaction centre (Torabi et al., 2014). The peripheral transmembrane subunit PsbY of PSII also had a higher ratio than many other PSII subunits. The function of PsbY has not been thoroughly studied. Still, it was proposed that PsbY is required to prevent photodamage to PSII under high light (Biswas and Eaton-Rye, 2018), the conditions that favour the formation of PSI–PSII supercomplexes (Iwai et al., 2010).

The PetM subunit of Cyt b_6f appeared to strongly prefer to interact with other complexes (Figure 3-7C). Indeed, the deletion of petM in *Synechocystis sp.* PCC 6803 could result in the reduced content of PSI and phycobilisomes, and PetM is involved in the regulatory processes of electron transfer pathways (Schneider et al., 2001). In ATPase, the subunit b’ possessed a significant difference in the relative abundance (Figure 3-7D). The long α-helices of the peripheral stalk subunits b′ and b are exposed to the outside of ATPase and clamp the integral membrane subunit a in its position next to the c-ring rotor, connecting F_1 to F_o (Hahn et al., 2018). Moreover, in the rotation of ATPase during ATP production, subunit b’ remains stable, thus making it favourable to bind with other complexes.

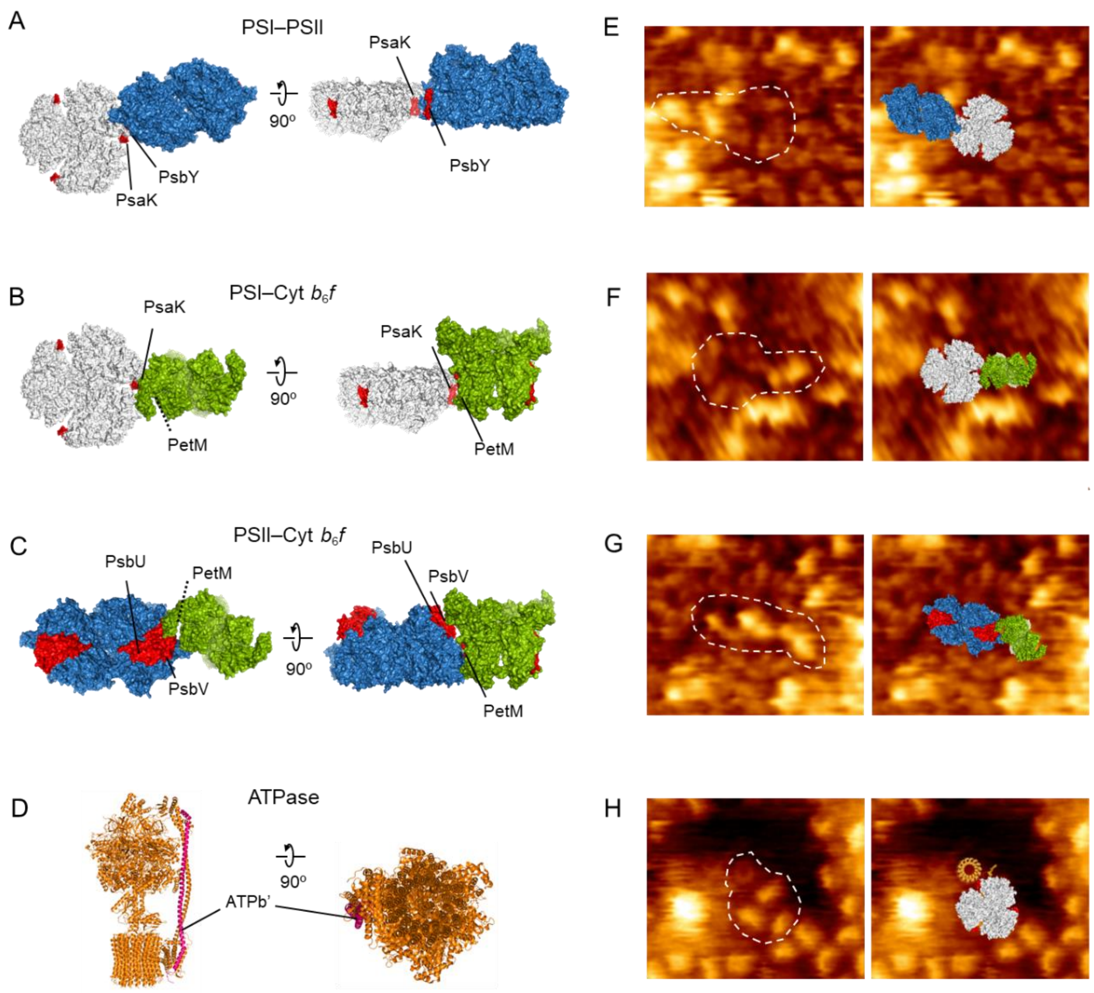

Figure 3-8 Hypothetical models of photosynthetic supercomplex associations.

Protein structures were obtained from PDB (PSI: 1JB0; PSII: 3WU2, Cyt b_6f: 4H13, ATPase: 6FKF).

(A) The hypothetical model of PSI–PSII supercomplex. Possible interacting subunits are PsaK of PSI and PsbY of PSII (red).

(B) The hypothetical model of PSI-Cyt b_6f supercomplex. They interact at PsaK of PSI and PetM of Cyt b_6f (red).

(C) The hypothetical model of PSII-Cyt b_6f supercomplex. They interact at PsbU, PsbV of PSII and PetM of Cyt b_6f (red).

(D) The location of subunit b' (pink) in ATPase.

(E) AFM visualisation of PSI–PSII from the lumenal surface.

(F) AFM visualisation of PSI-Cyt b_6f from the lumenal surface.

(G) AFM visualisation of PSII-Cyt b_6f from the lumenal surface.

(H) AFM visualisation of PSI-ATPase from the cytoplasmic surface. Associations in (E-H) are corresponding to (A-D).

Based on the pull-down assays and mass spectrometry results, the models of photosynthetic complex associations were proposed (Figure 3-8). The peripheral subunit PsaK of PSI, PetM of Cyt b_6f and the subunit b' of ATPase might sit at the interfaces between distinct photosynthetic complexes to facilitate specific associations of photosynthetic complexes in the thylakoid membranes (Figure 3-8A-D). AFM imaging on the native photosynthetic membranes has revealed the structures, lateral distribution and physical associations of photosynthetic complexes (Casella et al., 2017, Zhao et al., 2020). Similar associations of different photosynthetic complexes as the proposed models have been observed in AFM (Figure 3-8E-H), although the structural variability could be due to the intricate properties of supercomplex assemblies in thylakoid membranes (Zhao et al., 2020). The structural variability might be more significant in PSII associations, resulting in unidentified specific binding sites in the PSII complex.

There is increasing experimental evidence as to the formation of electron transport supercomplexes in cyanobacterial and chloroplast thylakoids (Watanabe et al., 2014, Gao et al., 2016, Iwai et al., 2010, Peng et al., 2008, Peng et al., 2009, Kouřil et al., 2014, Liu et al., 2013, Bečková et al., 2017) and mitochondria (Lapuente-Brun et al., 2013). The associations between different photosynthetic complexes in thylakoid membranes appeared to be weak, transient and dynamic (Zhao et al., 2020), given the highly dynamic and regulatable thylakoid membrane environment in cyanobacteria (Mullineaux and Liu, 2020). This makes it challenging to identify and isolate functionally active supercomplexes for subsequent investigation. Further improvement is required to reinforce the inter-complex associations; for example, cross-linking reagents could be used in the future (Liu et al., 2013).

3.2.7 Association between PSI and NDH-1

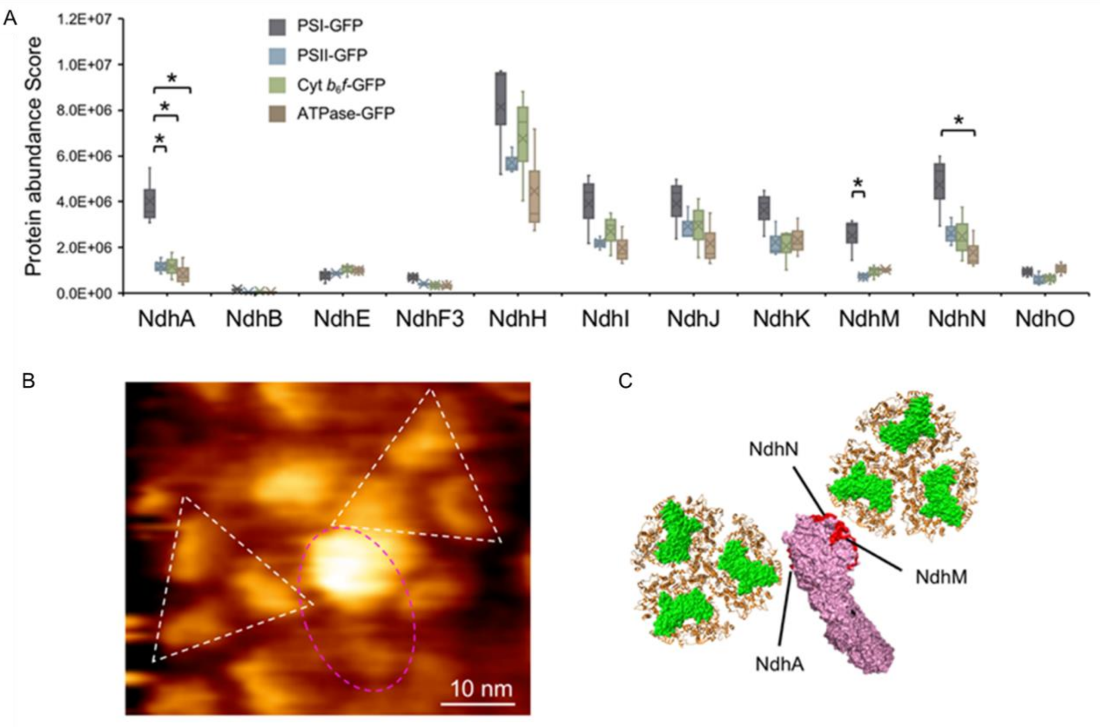

Figure 3-9 NDH-1 subunits detected in four pull-down groups and the hypothetical model of PSI−NDH-1 association.

(A) NDH-1 subunits detected in each GFP-labelled pull-down samples. Box plots display the median (line), the average (cross), the interquartile range (box) and the maximum and minimum (whiskers). Statistical analysis was performed using Student's t-test. *: $0.01 < P < 0.05$.

(B) AFM image of the PSI−NDH-1 associations in native thylakoid membranes from Syn7942.

(C) The hypothetical model of PSI−NDH-1 associations based on the AFM image shown in (B). The potential interacting sites NdhA, NdhN and NdhM of NDH-1 are in red. The protein structures were obtained from PDB (PSI: 1JB0, NDH-I: 6NBQ).

In addition to the supercomplexes formed by photosynthetic complexes, PSI−NDH-1 supercomplexes have also been characterised in cyanobacteria and plants to facilitate cyclic electron transport (Zhao et al., 2020, Gao et al., 2016, Kouřil et al., 2014). The results exhibited that NdhA, NdhM and NdhN had a significantly higher abundance in the PSI-GFP pull-down sample than in other samples (Figure 3-9A). The structure of

NDH-1 revealed that NdhA forms a part of a heel to support a peripheral arm of the complex (Q-module) that comprises photosynthesis-specific subunits NdhM, NdhN, NdhO and NdhS (Schuller et al., 2019, Laughlin et al., 2019, Pan et al., 2020, Zhang et al., 2020, Schuller et al., 2020). The peripheral arm is proven to be the site that interacts with ferredoxin (Fd) to plastoquinone (PQ) (Schuller et al., 2019, Pan et al., 2020). The binding of PSI to this part of NDH-1 appears to be functionally preferable. AFM confirmed that such PSI−NDH-1 associations do exist in native thylakoid membranes from Syn7942 (Figure 3-9BC), resembling the plant PSI−NDH-1 supercomplex observed by cryo-EM (Kouřil et al., 2014). Consistently, higher light can trigger the redistribution of NDH-1 in Syn7942 cells from patches to more even distribution, colocalised with PSI, along the thylakoid membranes (Liu et al., 2012). This suggested the closer proximity of NDH-1 complexes to PSI, which likely correlates with a switch from linear to cyclic photosynthetic electron transport.

3.2.8 Other protein complexes in cyanobacterial thylakoid membranes

Table 3-1 Protein abundance of all detected protein and the percentage of the difference between a certain group and the average of four groups.

Different colours visually present the difference—green marked proteins have a lower abundance than the average, while red means a higher abundance. The more saturated the colour is, the greater the difference is. Significance was calculated both within four photosynthetic complexes and between the group with the highest protein score and WT. *: 0.01 < P < 0.05, **: 0.001 < P < 0.01, ***: P < 0.001.

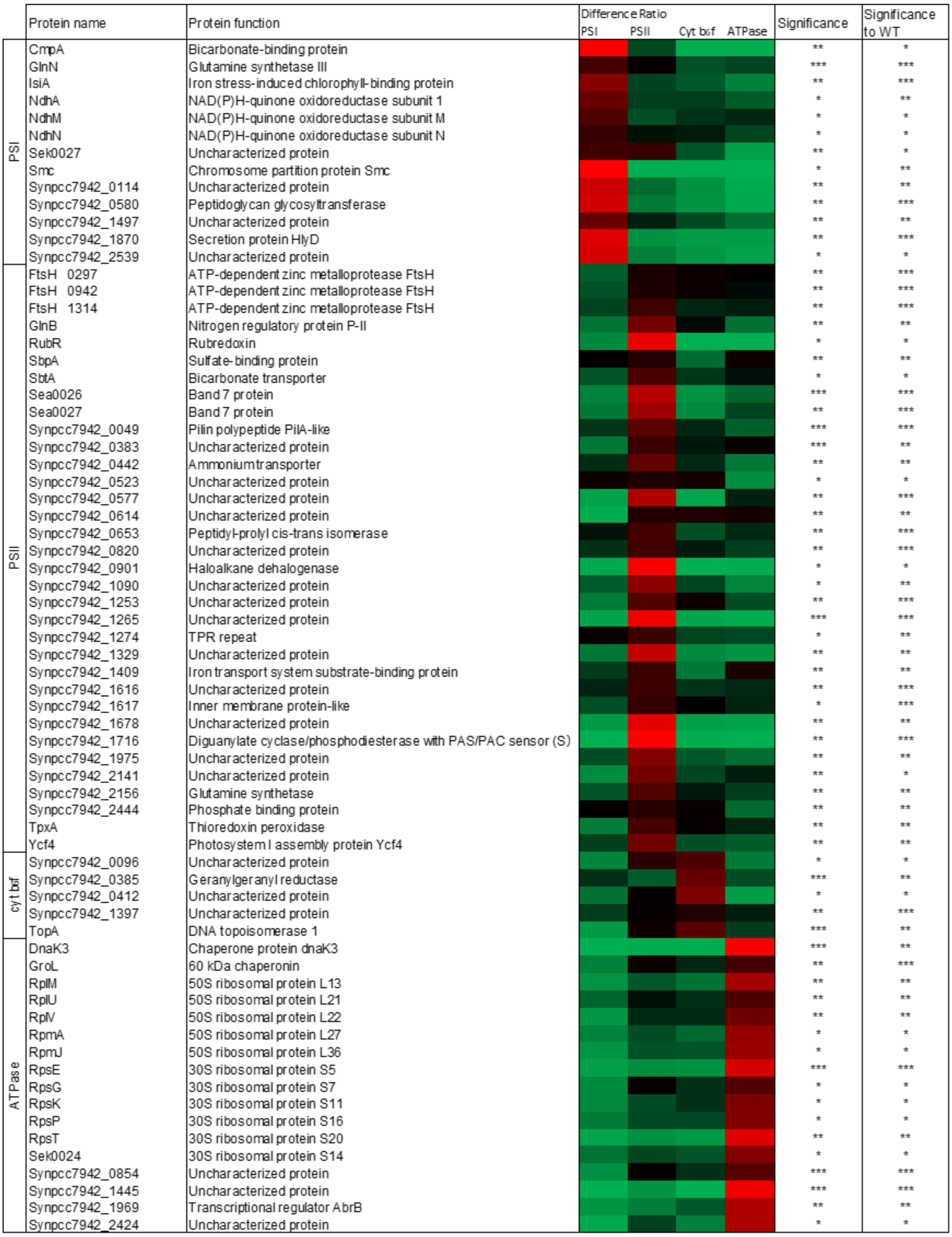

	Protein name	Protein function	Difference Ratio				Significance	Significance to WT
			PSI	PSII	Cyt b$_6$f	ATPase		
PSI	CmpA	Bicarbonate-binding protein	🟥	🟩	🟩	🟩	**	*
	GlnN	Glutamine synthetase III	🟥	⬛	🟩	🟩	***	***
	IsiA	Iron stress-induced chlorophyll-binding protein	🟥	🟩	🟩	🟩	**	***
	NdhA	NAD(P)H-quinone oxidoreductase subunit 1	🟥	🟩	🟩	🟩	*	**
	NdhM	NAD(P)H-quinone oxidoreductase subunit M	🟥	🟩	🟩	🟩	*	*
	NdhN	NAD(P)H-quinone oxidoreductase subunit N	🟥	⬛	⬛	🟩	*	*
	Sek0027	Uncharacterized protein	🟥	🟥	🟩	🟩	**	*
	Smc	Chromosome partition protein Smc	🟥	🟩	🟩	🟩	*	**
	Synpcc7942_0114	Uncharacterized protein	🟥	🟩	🟩	🟩	**	**
	Synpcc7942_0580	Peptidoglycan glycosyltransferase	🟥	🟩	🟩	🟩	**	***
	Synpcc7942_1497	Uncharacterized protein	🟥	⬛	🟩	🟩	**	**
	Synpcc7942_1870	Secretion protein HlyD	🟥	🟩	🟩	🟩	**	***
	Synpcc7942_2539	Uncharacterized protein	🟥	🟩	🟩	🟩	*	*
PSII	FtsH 0297	ATP-dependent zinc metalloprotease FtsH	🟩	⬛	⬛	⬛	**	***
	FtsH 0942	ATP-dependent zinc metalloprotease FtsH	🟩	⬛	⬛	⬛	**	***
	FtsH 1314	ATP-dependent zinc metalloprotease FtsH	🟩	🟥	⬛	⬛	**	***
	GlnB	Nitrogen regulatory protein P-II	🟩	🟥	⬛	🟩	**	**
	RubR	Rubredoxin	🟩	🟥	🟩	🟩	*	*
	SbpA	Sulfate-binding protein	⬛	⬛	🟩	⬛	**	**
	SbtA	Bicarbonate transporter	🟩	🟥	🟩	⬛	*	*
	Sea0026	Band 7 protein	🟩	🟥	🟩	🟩	***	***
	Sea0027	Band 7 protein	🟩	🟥	🟩	🟩	**	***
	Synpcc7942_0049	Pilin polypeptide PilA-like	🟩	🟥	⬛	🟩	***	***
	Synpcc7942_0383	Uncharacterized protein	🟩	🟥	⬛	⬛	***	**
	Synpcc7942_0442	Ammonium transporter	🟩	🟥	🟩	🟩	**	**
	Synpcc7942_0523	Uncharacterized protein	⬛	⬛	⬛	🟩	*	*
	Synpcc7942_0577	Uncharacterized protein	🟩	🟥	🟩	⬛	**	***
	Synpcc7942_0614	Uncharacterized protein	🟩	⬛	⬛	⬛	**	**
	Synpcc7942_0653	Peptidyl-prolyl cis-trans isomerase	⬛	🟥	🟩	⬛	**	***
	Synpcc7942_0820	Uncharacterized protein	🟩	🟥	⬛	🟩	**	***
	Synpcc7942_0901	Haloalkane dehalogenase	🟩	🟥	🟩	🟩	*	*
	Synpcc7942_1090	Uncharacterized protein	🟩	🟥	🟩	🟩	*	**
	Synpcc7942_1253	Uncharacterized protein	🟩	🟥	⬛	🟩	**	***
	Synpcc7942_1265	Uncharacterized protein	🟩	🟥	🟩	🟩	***	***
	Synpcc7942_1274	TPR repeat	⬛	🟥	🟩	🟩	*	**
	Synpcc7942_1329	Uncharacterized protein	🟩	🟥	🟩	🟩	**	**
	Synpcc7942_1409	Iron transport system substrate-binding protein	🟩	🟥	🟩	⬛	**	**
	Synpcc7942_1616	Uncharacterized protein	⬛	🟥	🟩	⬛	**	***
	Synpcc7942_1617	Inner membrane protein-like	🟩	🟥	⬛	⬛	*	***
	Synpcc7942_1678	Uncharacterized protein	🟩	🟥	🟩	🟩	**	**
	Synpcc7942_1716	Diguanylate cyclase/phosphodiesterase with PAS/PAC sensor (S)	🟩	🟥	🟩	🟩	**	***
	Synpcc7942_1975	Uncharacterized protein	🟩	🟥	🟩	🟩	**	**
	Synpcc7942_2141	Uncharacterized protein	🟩	🟥	🟩	⬛	**	*
	Synpcc7942_2156	Glutamine synthetase	🟩	🟥	⬛	🟩	**	**
	Synpcc7942_2444	Phosphate binding protein	⬛	⬛	⬛	🟩	**	**
	TpxA	Thioredoxin peroxidase	🟩	🟥	⬛	⬛	**	**
	Ycf4	Photosystem I assembly protein Ycf4	🟩	🟥	🟩	🟩	**	**
cyt b$_6$f	Synpcc7942_0096	Uncharacterized protein	🟩	⬛	🟥	🟩	*	*
	Synpcc7942_0385	Geranylgeranyl reductase	⬛	🟩	🟥	🟩	***	**
	Synpcc7942_0412	Uncharacterized protein	🟩	⬛	🟥	🟩	*	*
	Synpcc7942_1397	Uncharacterized protein	🟩	⬛	⬛	⬛	**	***
	TopA	DNA topoisomerase 1	🟩	⬛	🟥	🟩	***	**
ATPase	DnaK3	Chaperone protein dnaK3	🟩	🟩	🟩	🟥	***	**
	GroL	60 kDa chaperonin	🟩	⬛	⬛	🟥	**	***
	RplM	50S ribosomal protein L13	🟩	🟩	🟩	🟥	**	**
	RplU	50S ribosomal protein L21	🟩	⬛	⬛	🟥	**	**
	RplV	50S ribosomal protein L22	🟩	⬛	⬛	🟥	**	**
	RpmA	50S ribosomal protein L27	🟩	🟩	🟩	🟥	*	*
	RpmJ	50S ribosomal protein L36	🟩	🟩	🟩	🟥	*	*
	RpsE	30S ribosomal protein S5	🟩	🟩	🟩	🟥	***	***
	RpsG	30S ribosomal protein S7	🟩	⬛	⬛	🟥	*	*
	RpsK	30S ribosomal protein S11	🟩	🟩	⬛	🟥	*	*
	RpsP	30S ribosomal protein S16	🟩	🟩	🟩	🟥	*	*
	RpsT	30S ribosomal protein S20	🟩	🟩	🟩	🟥	**	**
	Sek0024	30S ribosomal protein S14	🟩	🟩	🟩	🟥	*	*
	Synpcc7942_0854	Uncharacterized protein	🟩	⬛	⬛	🟥	***	***
	Synpcc7942_1445	Uncharacterized protein	🟩	🟩	🟩	🟥	***	***
	Synpcc7942_1969	Transcriptional regulator AbrB	🟩	🟩	🟩	🟥	**	**
	Synpcc7942_2424	Uncharacterized protein	🟩	🟩	🟩	🟥	*	*

A motivation for the unbiased analysis of samples from the pull-down assays was to explore the biology of uncharacterised proteins. Besides the photosynthetic complexes and NDH-1 complexes described above, additional proteins were also detected from the GFP pull-down samples (Table 3-1). The iron stress-induced chlorophyll-binding protein IsiA and PSI form supercomplexes to increase the absorption cross-section of PSI (Andrizhiyevskaya et al., 2002, Kouřil et al., 2005, Toporik et al., 2019, Zhao et al., 2020). The bicarbonate-binding protein CmpA may also bind to PSI, which is an interesting finding regarding the possible integration of the light reactions and dark reactions of the photosynthetic system. In addition, the chromosome partition protein Smc, the Secretion protein HlyD, and peptidoglycan glycosyltransferase were shown to bind to PSI.

Proteins associated with PSII include PSI assembly protein Ycf4, three copies of ATP-dependent zinc metalloprotease FtsH (0297: FtsH1, 0942: FtsH2, and 1314: FtsH4), and an uncharacterised protein which is hypothetical PsbQ (Synpcc7942_1678). FtsH protease was implicated in repairing photodamaged PSII (Komenda et al., 2006, Silva et al., 2003). The fact that band 7 proteins Sea0026 and Sea0027 binds to PSII, as two prohibitin homologues, has been reported before in Synechocystis sp. PCC 6803 to prevent the undesirable degradation of newly-synthesised unassembled D1 (Silva and Nixon, 2001), analogous to the process established in mitochondria (Nijtmans et al., 2000). Additional proteins associated with PSII included the PSI assembly protein Ycf4 and the bicarbonate transporter SbtA. Cyt b_6f might interact with DNA topoisomerase TopA and geranylgeranyl reductase, which catalyse the synthesis of phytyl pyrophosphate required for the production of chlorophylls, phylloquinone and tocopherols (Shpilyov et al., 2005). ATPase had a close relationship with the chaperon protein DnaK3 (Palleros et al., 1993), 30S ribosomal protein, 50S ribosomal protein, and a transcriptional regulator, AbrB.

3.3 Concluding remarks

A central question about the cyanobacterial thylakoid membrane is how their photosynthetic and respiratory complexes are distributed and regulated. This chapter presented a method that integrated data derived from GFP pull-down assays, mass spectrometry and AFM for biochemical and structural characterisation of photosynthetic complex assemblies from thylakoid membranes of Syn7942. The specific inter-complex associations and potential binding domains of different photosynthetic complexes were characterised in detail, and the structural models of photosynthetic complex associations were proposed. Moreover, other binding proteins associated with the major photosynthetic complexes were also identified, indicating the highly connecting networks in the thylakoid membrane. This study delivers insight into the physical interplay of photosynthetic complexes and partners in cyanobacterial thylakoid membranes, providing the structural basis for efficient energy transfer. Advanced knowledge of the molecular basis underlying the organisation and interactions of protein complexes in the photosynthetic machinery may inform strategies for the rational design and engineering of artificial photosynthetic membranes and light-driven charge separation systems, with the intent of efficiently capturing and stabilizing solar energy to underpin energy production.

We found that supercomplexes formed between PSI and PSII, PSI and NDH-1, and that cytochrome b_6f could also be involved in those supercomplexes. It is worth mentioning that only a small percentage of complexes form supercomplexes; the association is possibly transient and dynamic. Generally speaking, the regulation of functional photosynthetic and respiratory thylakoid membrane is a highly dynamic process. For instance, PBSs in cyanobacteria have been reported to have great lateral mobility, and this diffusion is necessary for light-state transitions (Joshua and Mullineaux, 2004, Liu et al., 2009a, Van Thor et al., 1998, McConnell et al., 2002). In addition, the redox state change of an electron carrier can lead to the redistribution of respiratory complexes NDH-1 and SDH, further resulting in a change in the electron flow pathways (Liu et al., 2012). Further studies are needed in order to answer when, how, and why those supercomplexes are formed.

However, it would be biased to neglect the limitations of this study. Firstly, and foremostly, mass spectrometry itself is not a quantitative method. Digested proteins end as a complicated mixture of peptides with different mass-to-charge ratios; one must compare each peptide individually between experiments to achieve accurate quantification. Among several different quantification methods, two label-free quantification methods were critically reviewed (Bantscheff et al., 2007, Wang et al., 2008a, Deracinois et al., 2013) and adopted on account of their feasibility. The first one works to measure and compare the MS intensity of peptide precursor ions of a protein. The second one works as counting and comparing the number of fragment spectra. Aside from these, a value namely protein abundance index (PAI) (Rappsilber et al., 2002) was proposed, which is the ratio of observed peptides to observable peptides for a certain protein. It was found that the PAI shows a linear relationship with the logarithm of protein concentration. Thus, exponentially modified protein abundance index (emPAI) was defined as 10^{PAI}-1 to quantify protein content (Ishihama et al., 2005). It could roughly present the comparison of different proteins; but for the same protein in different samples, it is not as accurate as the label-free quantification used in this study. In contrast to these techniques, stable isotope labelling can be employed if one desires to obtain absolute quantification. They are certainly superior in terms of accuracy for a certain protein but not as practical in this study. The reason is that, in label-free quantification, the mass spectrometer is not over-occupied by fragmentation of labelled peptides, therefore can provide better analytical depth and dynamical range, resulting in more peptides being detected (Bantscheff et al., 2007); apart from this, for isotope-labelled methods, only 2-8 experiments can be compared at one time (Bantscheff et al., 2007), which was not suitable for the original purposes. Moreover, apart from the control strain used in this study, which was a wild-type S. elongatus PCC 7942 strain, a control containing free GFP could potentially be induced. In this way, the chance of GFP interacting with random proteins could be considered. If this is achieved by expressing free GFP that is dissociated from any fusion protein, they are almost certainly in the cytoplasm and get eliminated during the thylakoid isolation step. If this is achieved by adding heterologous expressed GFP, it may induce external error and impair the precise determination of the GFP quantity. Either way, a potential improvement would require careful design.

In terms of future work, this study may facilitate the engineering of photosynthetic apparatus. For example, with respect to the goal of stopping the global warming in a CO_2 neutral and eco-friendly way, scientists have been investigating minimal cells and even artificial biological machines, which would potentially allow maximal efficiency in biological processes (Schwille et al., 2018). Artificial photosynthesis is one of the top subjects in synthetic biology (Collings and Critchley, 2007, Eisenberg and Nocera, 2005, Kamat, 2007, Balzani et al., 2008). A recent study successfully created semi-artificial chloroplasts by combining the light-harvesting thylakoid membranes of spinach with synthetic enzymes to make it possible to harvest sunlight and convert carbon dioxide to glycolate; it was proved to be a milestone in synthetic photosynthesis, validating the idea that natural and artificial units can be integrated to perform life functions (Miller et al., 2020b).

4 Chapter 4 Localisation of photosynthetic and respiratory complexes in the thylakoid membrane

4.1 Introduction

The thylakoid membranes are a densely packed subcompartment for photosynthetic activities, where the protein complexes of the photosynthetic electron transfer chain are embedded, including PSI (PSI), PSII (PSII), Cyt b_6f and ATP synthase (ATPase). In cyanobacteria, respiratory electron transport also takes place in the thylakoid membrane, including pieces of the respiratory chain machinery comprising type 1 NADH dehydrogenase (NDH-1), succinate dehydrogenase (SDH), cytochrome oxidase (cyt oxidase/COX), and other small components. Overall, thylakoid membranes are not homogeneous, protein complexes do not distribute evenly in them (Zhao et al., 2020), and the distribution is highly dynamic under different conditions. Back in the last century, the localisation of photosynthetic complexes in *S. elongatus* PCC 7942 (Syn7942) was determined using immunogold labelling, and it was claimed that PSI and the ATPase were found in the outer layer of the thylakoid while PSII and Cyt b_6f existed throughout the thylakoids (Sherman et al., 1994). In *Synechocystis* PCC6803, tightly packed crystalline PSII arrays were observed with electron microscopy after mild detergent treatment, implying the distribution of PSII is not always even (Folea et al., 2008). Atomic force microscopy (AFM) data showed that in *Prochlorococcus*, regions of densely packed PSI complexes were found in the thylakoid membranes, which also suggested an intriguing, uneven dispersal of photosystems (MacGregor-Chatwin et al., 2019). In Syn7942, PSI-enriched domains and PSII arrays have been visualised (Zhao et al., 2020). In the same organism, fluorescent-tagged PSI, PSII, Cyt b_6f, and ATPases appeared to have different distribution patterns and diffusion coefficients (Casella et al., 2017). A paper published in 2012 demonstrated that NDH-1 and SDH had a patchy distribution in the thylakoid membranes under low light conditions, and had a more even distribution after 30 minutes of growth light treatment (Liu et al., 2012).

Despite ample knowledge about the chemical mechanism of photosynthetic electron transfer as well as the structures of individual electron transfer complexes, information about how these protein complexes are regulated and dynamically coordinated to form a functional chain is still basic. Some questions remain unanswered, for example, how the membrane area with densely packed PSI would contribute to the photosynthetic processes with no other adjacent electron transfer complexes. The interaction between these photosynthetic and respiratory protein complexes and their relative position to one another *in vivo* have received scant attention in the research literature. This chapter aimed to unravel some of the mysteries surrounding these questions using the combination of dual-labelling and a well-established confocal fluorescence microscopy investigation method for cyanobacterial thylakoid membrane (Casella et al., 2017, Liu, 2016). We present a direct visualisation of *in vivo* colocalisation of photosynthetic complexes and respiratory complexes in natural thylakoid membranes of the cyanobacterial model strain Syn7942. Due to the rod shape of Syn7942 and its parallel thylakoid membranes, it is a suitable model to visualise the tagged photosynthetic and respiratory complexes with confocal microscopy.

4.2 Results and Discussion

To study the localisation correlation between photosynthetic and respiratory complexes, recombination of fluorescent protein labelling and image analysis were carried out. PSI was tagged with a cyan fluorescent protein (CFP). The reason to choose PSI was that PSI is the most abundant photosynthetic protein (Casella et al., 2017), and CFP emits a weaker signal than yellow fluorescent protein (YFP). Other proteins from the thylakoid membrane, including PSII, ATPase, NDH-1 and Cyt c oxidase, were tagged with YFP. The subunits tagged with YFP were PsaE in PSI, PsbB in PSII, ATP_B in ATPase, NdhM in NDH-1 and CtaE in cytochrome c oxidase. PCR verifications confirmed the full segregation of the mutant strains (Figure 4-1A).

Another photosynthetic complex, Cyt b_6f, has been labelled with YFP, but full segregation of this double labelling strain has not been achieved in the experiments. To evaluate the potential differences among those mutant strains, the growth curves of all dual-labelling strains and WT were monitored, and no significant differences were observed (Figure 4-1B). The absorbance spectra of WT and mutant strains (Figure 4-1C) did not demonstrate significant differences in pigment content, including chlorophyll a, which absorbs blue light at around 440 nm and red light at around 680 nm, phycocyanin plus phycobilisomes that absorbs orange light at 600-640 nm, and the minor peak at 400-550 nm ascribed to carotenoids.

In the experiments, two conditions of cells were compared. Cells were all grown in moderate light (ML) / growth light of 40 $\mu E \cdot m^{-2} \cdot s^{-1}$. Light condition samples were constantly in ML, while dark condition samples were grown in ML and examined with microscopy after dark-adaption of 15 min. To avoid CFP to YFP fluorescence resonance, CFP and YFP channels were recorded separately within a very short time. Argon laser with an excitation wavelength of 458 nm was used for CFP detection at 470-500 nm, and a 514 nm laser was used to excite YFP detected at 520-550 nm CFP.

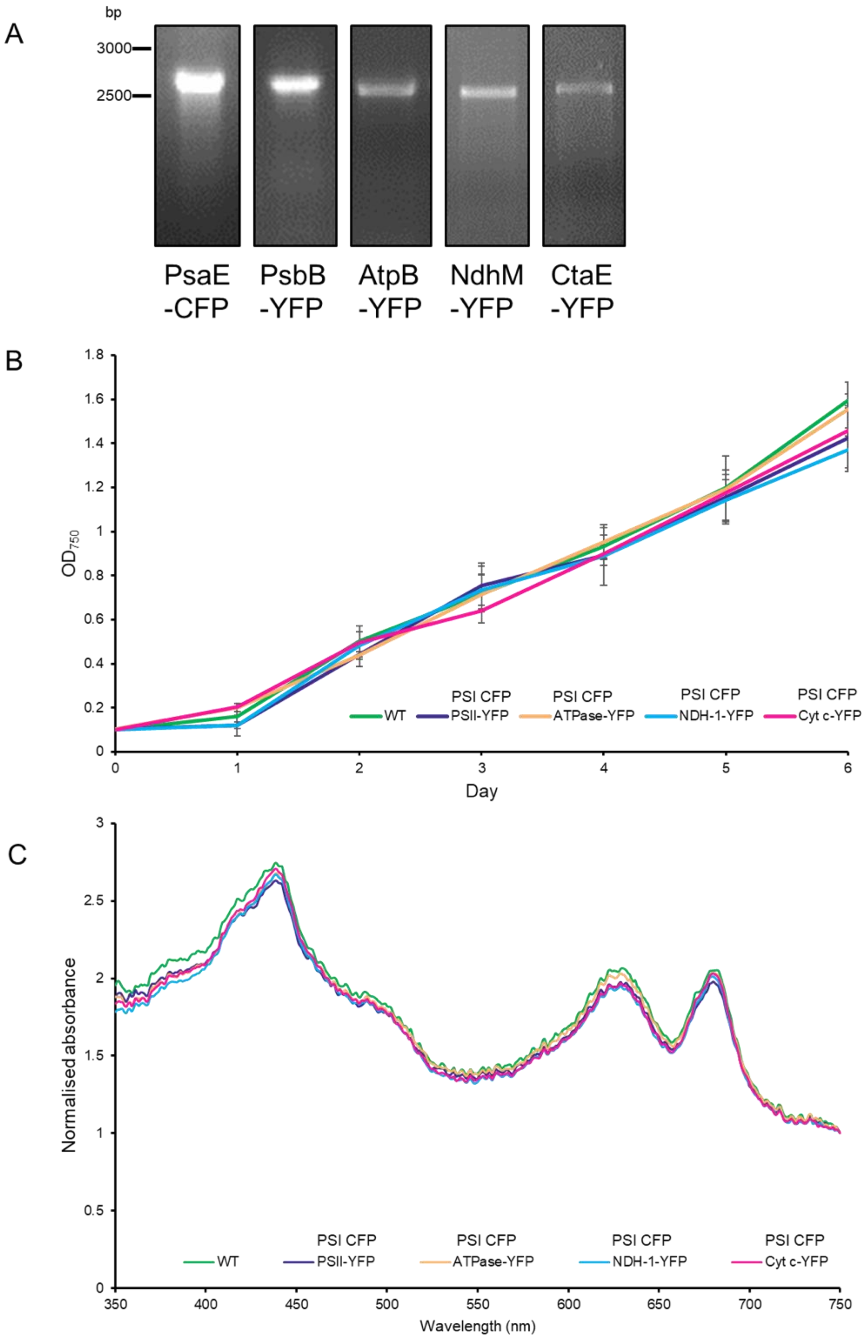

Figure 4-1 Verification of photosynthetic complex dual-labelling strains.

PsaE in PSI is labelled with CFP. PsbB in PSII, AtpB in ATPase, NdhM in NDH-1 and CtaE in cytochrome c oxidase are labelled with YFP, respectively.

(A) Growth curves of wild type and mutant strains at 30°C with constant 40 $\mu E \cdot m^{-2} \cdot s^{-1}$ white illumination.

(B) Absorption spectra of wild type and mutant strains from 350 nm to 750 nm normalised at OD_{750}.

4.2.1 Co-localisation of PSI and PSII

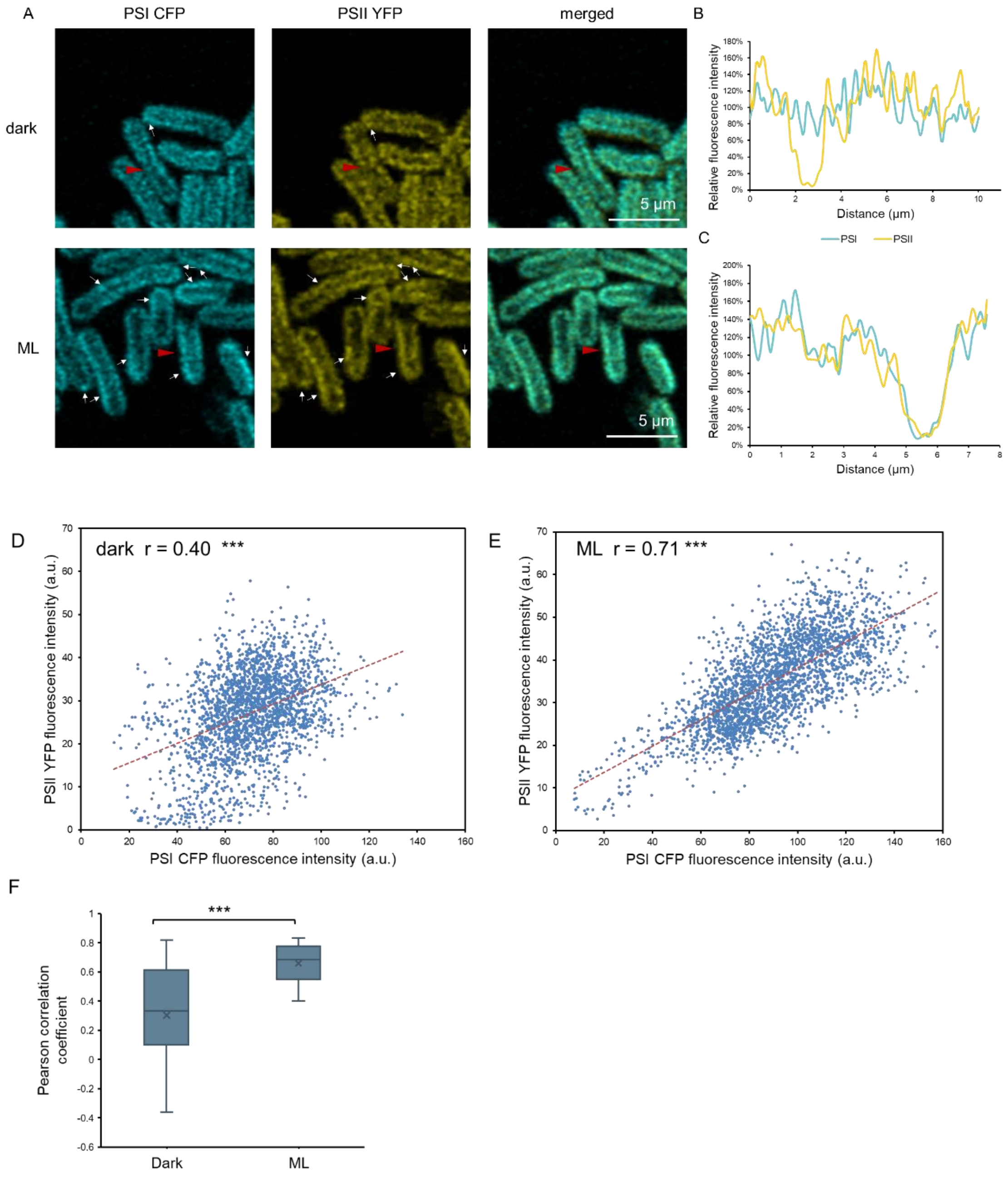

Figure 4-2 Confocal microscopy of co-localisation of PSI and PSII.

(A) Confocal microscopy imaging of PSI-CFP and PSII-YFP distributions observed in the dark-adapted samples and ML (40 µE·m^{-2}·s^{-1}) samples. White arrows indicate similar protein distributions between PSI-CFP and PSII-YFP.

(B) Plot profile of PSI-CFP and PSII-YFP of a typical cell indicated with red triangles in the dark-adapted sample.

(C) Plot profile of PSI-CFP and PSII-YFP of a typical cell indicated with red triangles in ML sample.

(D) Regression analysis of the correlation between PSI-CFP and PSII-YFP in the dark-adapted sample (N = 2284 data points of 20 cells). Pearson correlation coefficient r value is calculated for all data points. Statistical significance is determined with two-tailed Student’s T distribution. *: $0.01 < P < 0.05$, **: $0.001 < P < 0.01$, ***: $P < 0.001$ (see methods).

(E) Regression analysis of the correlation between PSI-CFP and PSII-YFP in ML sample (N = 2655). Pearson correlation coefficient r value is calculated for all data points. Statistical significance is determined with two-tailed Student’s T distribution. *: $0.01 < P < 0.05$, **: $0.001 < P < 0.01$, ***: $P < 0.001$.

(F) Distribution of Pearson correlation coefficient of each cell in a group of 20, presenting the heterogeneity (N = 20 cells).

The first pair of protein complexes studied were PSI and PSII. Figure 4-2A shows confocal microscopic images of fluorescent PSI-CFP and PSII-YFP under dark and light conditions, excited with a laser of 458 nm and 514 nm, respectively. By plotting CFP signals and YFP signals of measured data points, the normalised fluorescence profiles of both samples demonstrated PSI and PSII tended to correlate on a larger scale, especially under moderate light (Figure 4-2BC). To comprehensively evaluate the relationship between PSI and PSII, quantitative linear regression analyses were performed on PSI CFP and PSII YFP fluorescent intensity. Scatterplots showed that light treatment leads to a higher covariance than dark treatment. 0.71 in ML ($p = 0$) (Figure 4-2D and Figure 4-2E). The large sample size gave a certain validity to these relations. By comparing Pearson’s correlation coefficient of individual cells in two groups of 20 cells, it was found that the tendency was homogeneous among the population (Figure 4-2F). The colocalisation of PSI and PSII in ML is reasonable since electrons are passed from PSII to PSI in the transfer chain; and PSI and PSII have been proved to form supercomplexes (Bečková et al., 2017), as discussed in Chapter 3. AFM data have shown PSI and PSII can coexist in the same area (Zhao et al., 2020, Casella et al., 2017). However, in a much earlier study, it was shown that in Syn7942, PSI complexes were mostly detected in the inner thylakoid membrane layers while PSI complexes were found mostly in the outer layers (Sherman et al., 1994), probably owing to the evolutionary pressure to avoid quenching of PS II by PS I because they have distinct exciton trapping kinetics (Trissl and Wilhelm, 1993). A conflicting study with *in vivo* hyperspectral confocal fluorescence in *Synechocystis* 6803 stated that PSII was found concentrated near the periphery of the cell, while PSI was observed in the inner thylakoid (Vermaas et al., 2008). The final answer of whether PSI and PSII distribute throughout all thylakoid membrane layers seems unfathomable by now.

4.2.2 Co-localisation of PSI and ATPase

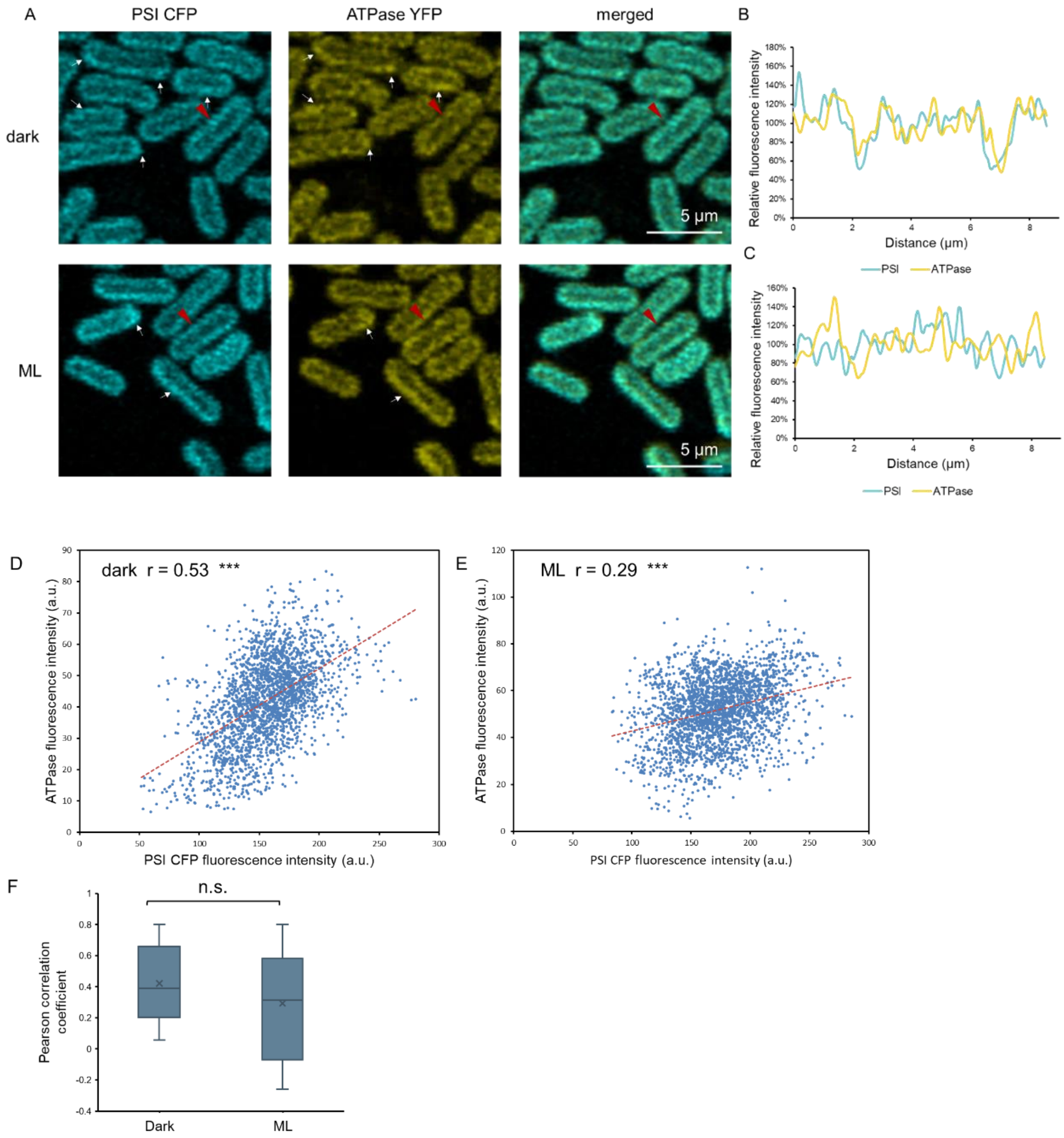

Figure 4-3 Confocal microscopy of co-localisation of PSI and ATPase.

(A) Confocal microscopy imaging of PSI-CFP and ATPase-YFP distributions, observed in the dark-adapted samples and ML (40 µE·m-2·s-1) samples. White arrows indicate similar protein distributions between PSI-CFP and ATPase-YFP.

(B) Plot profile of PSI-CFP and ATPase-YFP of a typical cell indicated with red triangles in the dark-adapted sample.

(C) Plot profile of PSI-CFP and ATPase-YFP of a typical cell indicated with red triangles in ML sample.

(D) Regression analysis of the correlation between PSI-CFP and ATPase-YFP in the dark-adapted sample (N = 2323 data points of 20 cells). Pearson correlation coefficient r value is calculated for all data points. Statistical significance is determined with two-tailed Student's T distribution. *: $0.01 < P < 0.05$, **: $0.001 < P < 0.01$, ***: $P < 0.001$ (see methods).

(E) Regression analysis of the correlation between PSI-CFP and ATPase-YFP in ML sample (N = 2452). Pearson correlation coefficient r value is calculated for all data points. Statistical significance is determined with two-tailed Student's T distribution. *: $0.01 < P < 0.05$, **: $0.001 < P < 0.01$, ***: $P < 0.001$.

(F) Distribution of Pearson correlation coefficient calculated of each cell in a group of 20, presenting the heterogeneity (N = 20 cells).

The dual labelling of PSI and ATPase showed moderate colocalisation in the thylakoid membranes (Figure 4-3). The distributional association between PSI and ATPase has been found in previous publications. Using immunocytochemistry, it was demonstrated that PSI and ATP synthase proteins typically inhabit the outermost layer of the thylakoid membrane, while PSII and cytochrome b6/f were found throughout the thylakoid (Sherman et al., 1994). Similar segregation was observed in higher plants as well (Albertsson, 2001). Nevertheless, it is worth mentioning that locating in the same thylakoid membrane area does not guarantee physical associations, but they may be contiguous on a larger scale. AFM data showed that ATPases were found adjacent to PSI domains (Zhao et al., 2020). Considering that PSI and ATPase are both involved in the photosynthetic electron transport chain, one unanticipated finding is that the correlation between PSI and ATPase was lower in ML. The Pearson correlation coefficient r value decreased from 0.53 in the dark to 0.29 in ML (Figure 4-3DE). The reason remains an open question.

4.2.3 Co-localisation of PSI and NDH-1

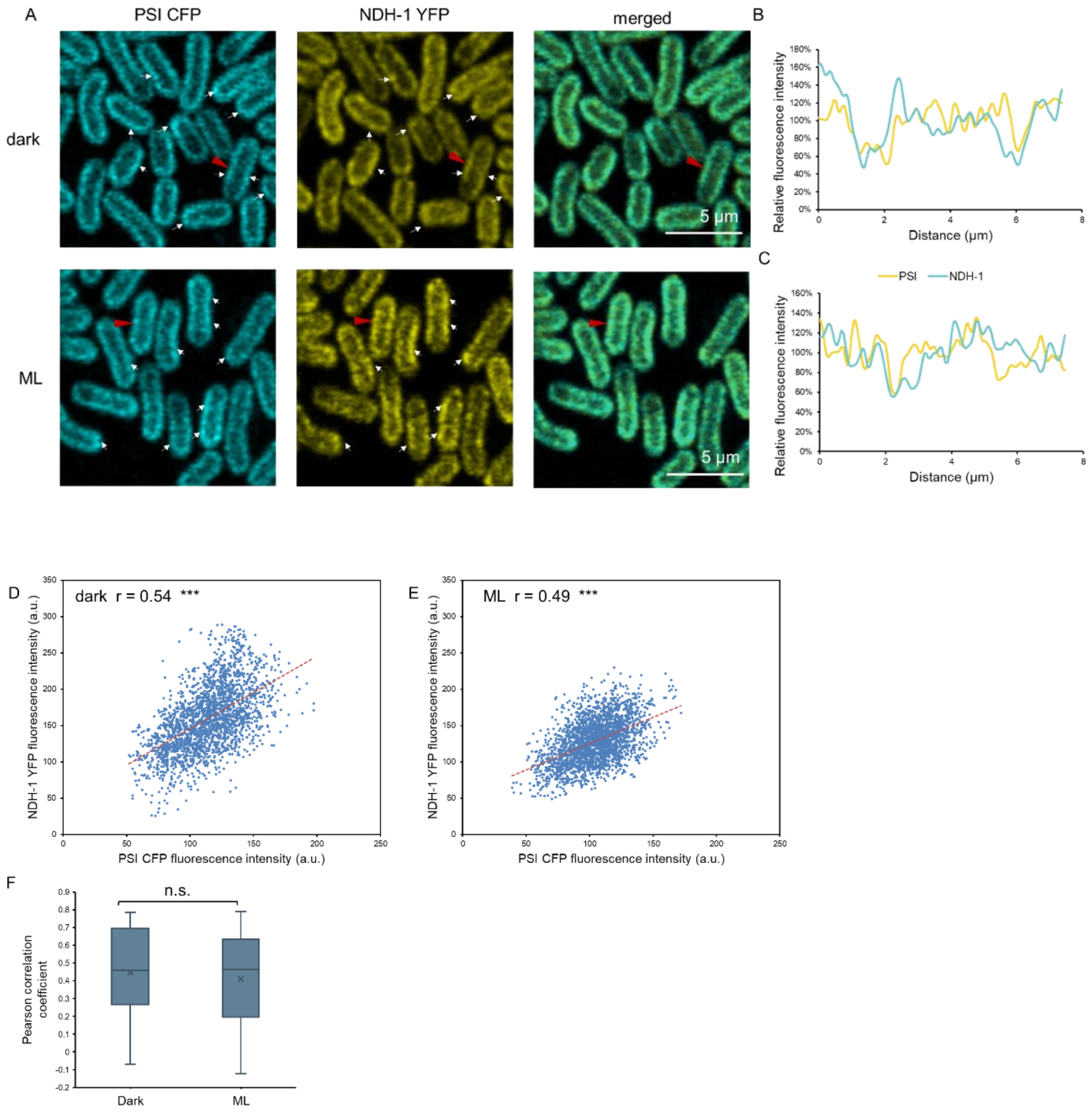

Figure 4-4 Confocal microscopy of co-localisation of PSI and NDH-1.

(A) Confocal microscopy imaging of PSI-CFP and NDH-1-YFP distributions, observed in the dark-adapted samples and ML (40 μE·m-2·s-1) samples. White arrows indicate similar protein distributions between PSI-CFP and NDH-1-YFP.

(B) Plot profile of PSI-CFP and NDH-1-YFP of a typical cell indicated with red triangles in the dark-adapted sample.

(C) Plot profile of PSI-CFP and NDH-1-YFP of a typical cell indicated with red triangles in ML sample.

(D) Regression analysis of the correlation between PSI-CFP and NDH-1-YFP in the dark-adapted sample (N = 2287 data points of 20 cells). Pearson correlation coefficient r value is calculated for all data points. Statistical significance is determined with two-tailed Student’s T distribution. *: $0.01 < P < 0.05$, **: $0.001 < P < 0.01$, ***: $P < 0.001$ (see method).

(E) Regression analysis of the correlation between PSI-CFP and NDH-1-YFP in ML sample (N = 2474). Pearson correlation coefficient r value is calculated for all data points. Statistical significance is determined with two-tailed Student’s T distribution. *: $0.01 < P < 0.05$, **: $0.001 < P < 0.01$, ***: $P < 0.001$.

(F) Distribution of Pearson correlation coefficient calculated of each cell in a group of 20, presenting the heterogeneity (N = 20 cells).

Type-1 NADPH dehydrogenase (NDH-1) is a member of respiratory enzymes and is also involved in cyclic electron flow. Results (Figure 4-4) revealed a close association between the fluorescent signals of PSI and NDH-1; the r value reaches 0.54 in the dark and 0.49 in ML (Figure 4-4D and Figure 4-4E). This strong relation could be due to both complexes dedicating to the cyclic electron transport in the thylakoid membrane (Lea-Smith et al., 2016). A previous paper demonstrated that the redox state was a parameter to affect the redistribution under different light conditions (Liu et al., 2012). The mechanism behind the redistribution in correspondence with PSI requires further studies.

4.2.4 Co-localisation of PSI and cytochrome c oxidase

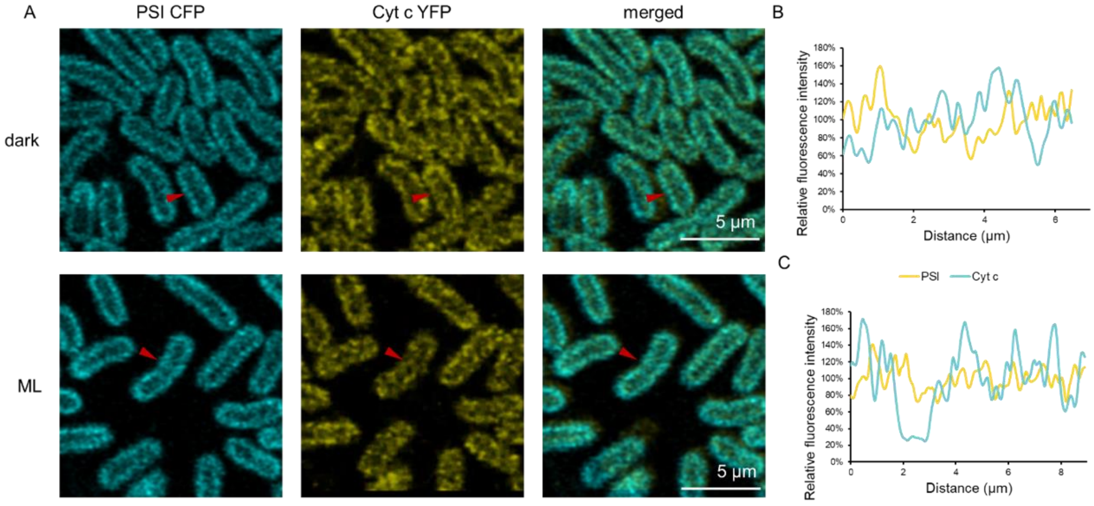

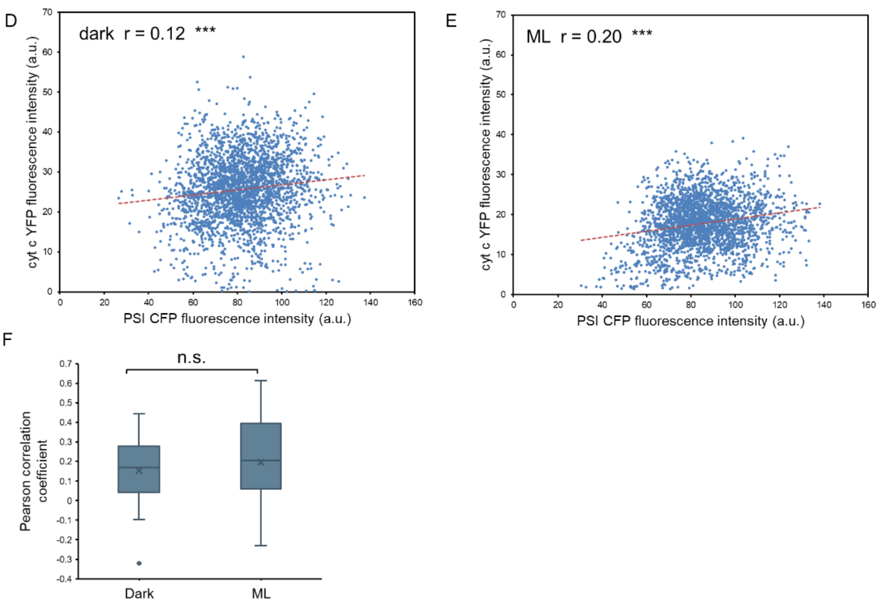

Figure 4-5 Confocal microscopy of co-localisation of PSI and cytochrome c oxidase.

(A) Confocal microscopy imaging of PSI-CFP and cytochrome c oxidase-YFP distributions, observed in the dark-adapted samples and ML (40 μE·m-2·s-1) samples. White arrows indicate similar protein distributions between PSI-CFP and cyt oxidase-YFP.

(B) Plot profile of PSI-CFP and cyt oxidase-YFP of a typical cell indicated with red triangles in the dark-adapted sample.

(C) Plot profile of PSI-CFP and cyt oxidase-YFP of a typical cell indicated with red triangles in ML sample.

(D) Regression analysis of the correlation between PSI-CFP and cyt oxidase-YFP in the dark-adapted sample (N = 2603 data points of 20 cells). Pearson correlation coefficient r value is calculated for all data points. Statistical significance is determined with two-tailed Student's T distribution. *: $0.01 < P < 0.05$, **: $0.001 < P < 0.01$, ***: $P < 0.001$ (see methods).

(E) Regression analysis of the correlation between PSI-CFP and cyt oxidase-YFP in ML sample (N = 2418). Pearson correlation coefficient r value is calculated for all data points. Statistical significance is determined with two-tailed Student's T distribution. *: $0.01 < P < 0.05$, **: $0.001 < P < 0.01$, ***: $P < 0.001$.

(F) Distribution of Pearson correlation coefficient calculated of each cell in a group of 20, presenting the heterogeneity (N = 20 cells).

Cyt c oxidase (COX) is a respiratory terminal oxidase of cyanobacteria that generates water from oxygen and results in ATP synthesis (Hart et al., 2005). It is a member of the respiratory electron transport cycle, with a functional relation to NDH-1 rather than PSI. Figure 4-5 shows the distribution of PSI and COX (Figure 4-5ABC) and regression analysis (Figure 4-5D and Figure 4-5E). As the least related pair, PSI and cyt c oxidase (COX) had the lowest distribution correlation between them. The Pearson correlation coefficient r values were low in both dark and ML, being 0.12 and 0.20 correspondingly, but the individual cell average had no significant difference between these two groups (Figure 4-5E).

4.2.5 Comparisons among complexes

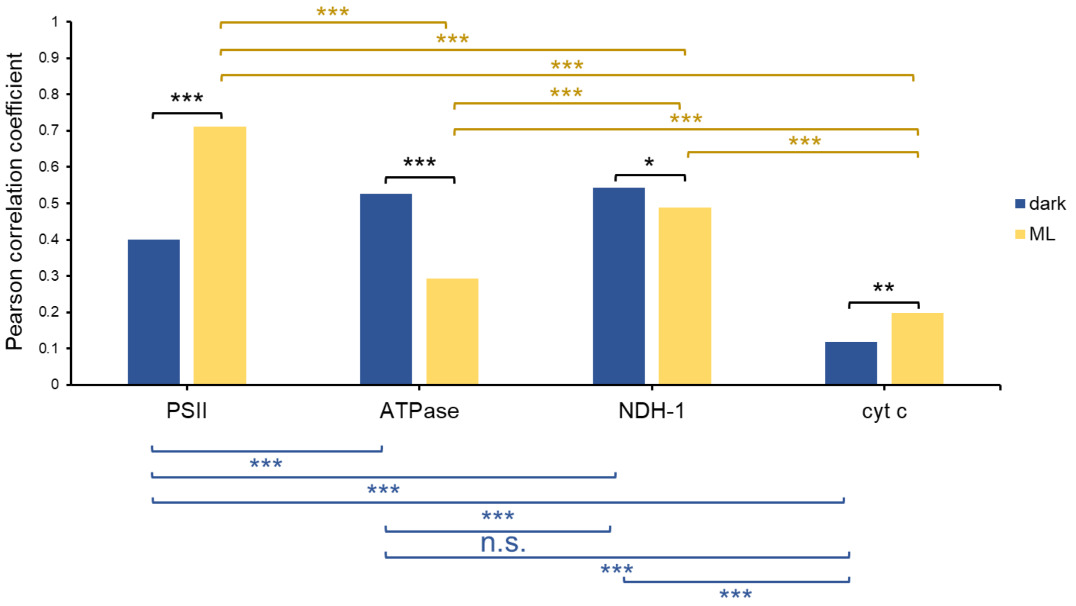

Figure 4-6 Paired comparisons of the correlation with PSI between complexes and between light conditions.

Pearson correlation coefficient is converted to be normally distributed with Fisher's r to z transformation. Then statistical significance is determined between groups. *: 0.01 < P < 0.05, **: 0.001 < P < 0.01, ***: P < 0.001 (see methods).

Overall, all four YFP-labelled thylakoid membrane proteins have a positively related distribution with PSI. Proteins with related functional roles clustering together might be a general rule in the cyanobacterial thylakoid membrane. Pearson correlation coefficients among these four proteins under different conditions were further compared via Fisher’s r to z transformation, revealing that the differences between each pair of proteins or conditions were significant except for the ATPase and NDH-1 in the dark (Figure 4-6). PSII showed a highly positive correlation with PSI in ML, but in the dark, the colocalisation was less strong than those of PSI–ATPase and PSI–NDH-1. Light clearly resulted in a redistribution of this photosynthetic system pair. Moreover, ATPase had a moderate positive correlation in the dark; NDH-1 had a moderate positive correlation with PSI regardless of light conditions; and cyt oxidase had the least correlation.

We have also compared the standard deviation of fluorescence intensity of each protein among different cells to characterise the heterogeneity (Figure 4-7). In general, the standard deviations were similar under two light conditions, meaning that proteins did not incline to change their distribution pattern when transferred between dark and light; patterns considered here are either even distribution or patchy distribution. Overall, the localisation pattern of each protein was more heterogeneous in the dark (a higher SD of the SD/mean), while in ML, different cells tended to behave similarly. What stands out in the chart is that NDH-1 had a lower normalised SD compared to any other complex, implicating a more even distribution. In a previously published study with confocal imaging, it was found that instead of the even distribution in ML, NDH-1 had a discrete, patchy distribution under low light (Liu et al., 2012). Different dark-adaption time could be used to further explore whether this patchy distribution is a common occurrence with a lack of light.

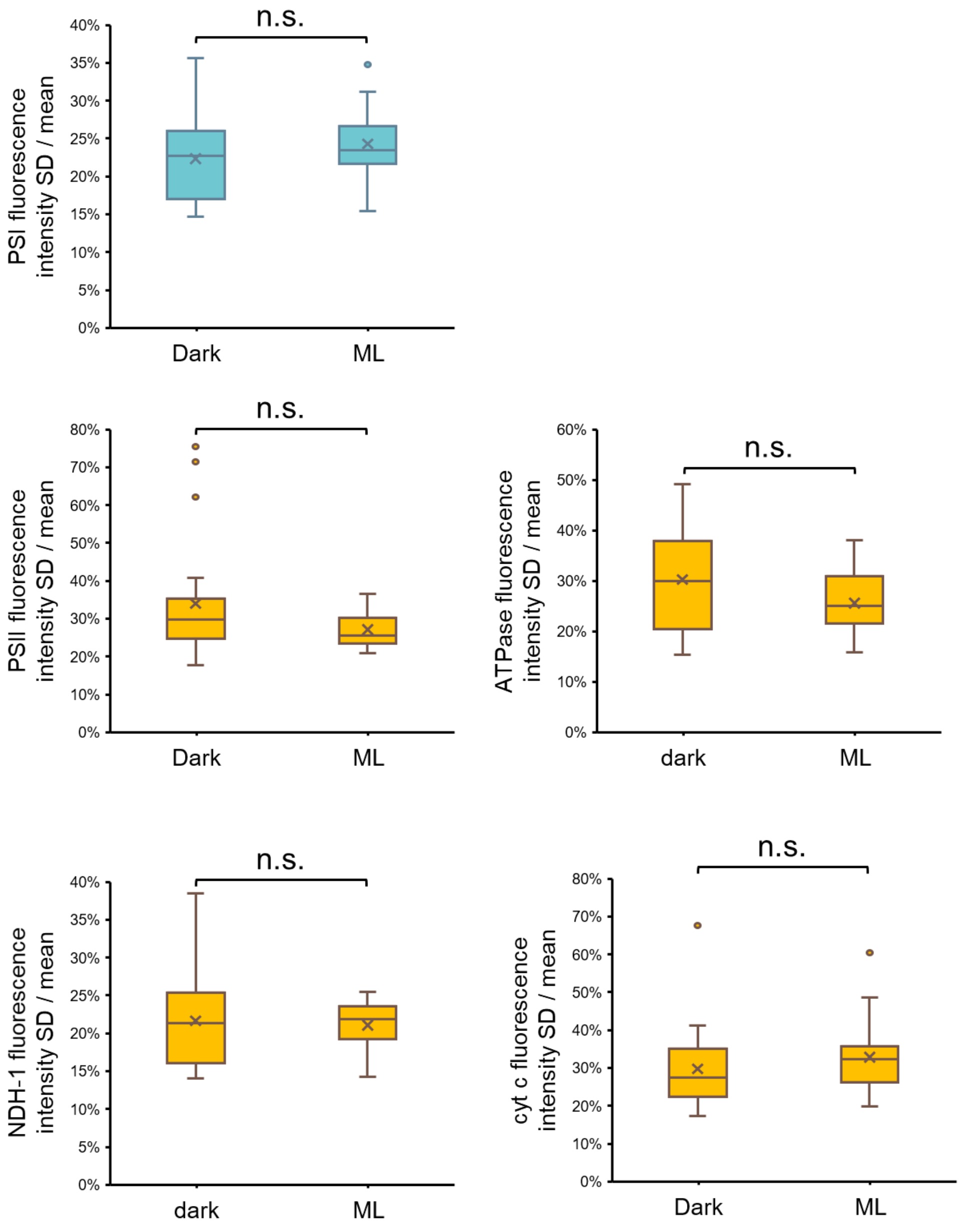

Figure 4-7 Normalised standard deviation of fluorescence intensity of each protein among different cells.

Fluorescence intensity is measured along the thylakoid membrane for each cell. Significance is determined with student t-test. *: $0.01 < P < 0.05$, **: $0.001 < P < 0.01$, ***: $P < 0.001$ (N = 20 for each group).

4.3 Concluding remarks

Using a combination of dual fluorescent labelling, confocal microscopy and regression analysis, this chapter depicts a general tendency of photosynthetic and respiratory complexes to colocalise with PSI in the thylakoid membrane. The level of colocalisation rises when the studied complex is functionally related to PSI. A remarkable example is that PSI and PSII have a striking propensity to colocalise in the light. ATPase and NDH-1 also have a moderate correlation with PSI. It could conceivably be hypothesised that these interactions facilitate electron transport. This finding, while preliminary, has extended knowledge of how these protein complexes are physiologically coordinated and regulated, and might ultimately expedite the design of artificial photosynthetic machinery to boost biofuel production in the far future. In contrast to the thylakoid membrane of higher plants, in which segregation of different photosynthetic proteins into grana and stromal lamella is common (Albertsson, 2001, Dekker and Boekema, 2005), the photosynthetic and respiratory complexes studied from Syn7942 have a relatively even distribution in the thylakoid membrane. The increase in the colocalisation level from dark to light brings attention to the similarities between this finding and an interesting result published in 2019 (Yokono et al., 2019), which found that algae within their natural habitat in higher light had a higher amount of PSI–PSII megacomplexes, e.g. *Dichotomosiphontuberosus* shows 51% of PSII forms PSI–PSII megacomplexes. Whilst the ratio is significantly lower for algae growing in deep water, for example, *Codium fragile* has only 8.8% PSI–PSII magacomplexes accumulated (Yokono et al., 2019).

Compared to previous studies of thylakoid membranes using various techniques, this study provides an *in vivo* and dynamic visualisation of the interaction between photosynthetic and respiratory complexes. AFM delivers a direct visualisation of the natural thylakoid membrane at high resolution (Zhao et al., 2020), but sampling small thylakoid membrane patches leads to lacking a comprehensive understanding of the overall protein distribution within the whole cell, and the designation of proteins in AFM highly depends on the particularity of the shape of protein complexes. However, owing to the optical resolution limitations, this method cannot discern the precise location of complexes as can be achieved by AFM (Casella et al., 2017, Zhao et al., 2020) or cryo-electron tomography (Wietrzynski et al., 2019) etc.

The results presented in this chapter were broadly in agreement with the pull-down results (Chapter 3) in terms of colocalisation on a larger scale. In Chapter 3, PSI are found to form supercomplexes with PSII and NDH-1, and in this chapter, it was presented that their distribution also correlated at a microscopic level. However, data in this chapter must be interpreted with caution because they do not serve as direct evidence of the existence of supercomplexes but rather indicate that the co-localisation of electron transfer complexes on a larger scale, due to the limitation of optical resolution of 180 nm laterally for a confocal microscope (Fouquet et al., 2015). In addition, the resolution along the z-axis was set to 2 μm in this experiment due to the pinhole setting. Therefore, it was also beyond the scope of this study to discern complexes from different layers of the thylakoid membrane, as the thylakoid repeat distance has been measured to be approximately 60–70 nm in a study using small-angle scattering (Jakubauskas et al., 2019).

Fluorescence resonance energy transfer (FRET) is a physical process in which energy will transfer from a donor fluorophore with higher energy to an acceptor fluorophore when the emission spectrum of the donor significantly overlaps the absorption spectrum of the acceptor. With the distance between these two fluorophores increasing, the energy transferred declines dramatically and becomes barely detectable over 10 nm (Siegel et al., 2000). Because CFP and YFP are a pair of such fluorophores, in this experiment, images were acquired separately using different lasers for CFP and YFP excitation (458 nm was used for CFP detection at 470–500 nm, and a 514 nm laser was used to excite YFP detected at 520–550 nm CFP) to eliminate sensitised fluorescence. Choosing CFP and YFP as a pair leaves sufficient room for further progress in determining the distance between each pair of labelled proteins using FRET measurements.

Several questions still retain unanswered. The factors that facilitate the colocalisation of photosynthetic complexes are subject to future studies. Are thylakoid membranes divided into functional subdomains? Are post-translational modifications involved in the transportation of photosynthetic complexes into the thylakoid membranes? Although there is a wealth of knowledge on the existence of light-triggered biological processes in photosynthetic complexes, the mechanisms underlying these processes remain relatively poorly understood. As stated before, in future investigations, it might be possible to determine whether changes in the electron transport activities facilitate the redistribution of protein complexes under different light conditions; as a paper proposed that the redistribution of NDH-1 and SDH is correlated with the redox state of an electron carrier (Liu et al., 2012).

5 Chapter 5 Roles of Curvature Thylakoid 1 protein in mediating thylakoid membrane structure and photosynthetic function

5.1 Introduction

The photosynthetic complexes of both chloroplasts and cyanobacteria, including photosystems and ATP synthases, are located in a unique internal membrane system, the thylakoid membrane. Research to date has not yet determined how the thylakoid membrane structure and functions are maintained (Liu et al., 2012). The structures of thylakoid membranes in chloroplasts and cyanobacteria are strikingly different. Cyanobacterial thylakoid membranes do not stack; the presence of membrane-associated light-harvesting complexes, phycobilisomes, may impose a physical resistance between thylakoid membrane layers (Mullineaux, 2005). However, thylakoid membranes share the characteristic of being able to form curvatures. For example, the thylakoid membranes of higher plants form curvatures at grana margins; the thylakoid membranes of *Synechocystis* PCC 6803 curve towards the cytoplasmic membrane (Heinz et al., 2016b), and *S. elongatus* PCC 7942 are mostly flat but form obtuse membrane curvatures at cellular poles. One of the important thylakoid regulators, which is believed to be able to perform the curving property of cyanobacterial thylakoids, is Curvature Thylakoid 1 (CURT1).

Studies on the CURT1 family have been performed on several organisms, with different protein names. In 2003, a study to identify novel phosphoproteins in thylakoid membranes of *A. thaliana* showed that a nuclear-coded 14-kDa-protein with a chloroplast-targeting peptide was a site of phosphorylation and was therefore named as thylakoid membrane phosphoprotein of 14 kDa (TMP14) (Hansson and Vener, 2003). Later, a paper published in 2005 claimed that the newly found TMP14 in *Arabidopsis* was a new subunit of PSI and named it PSI-P, given its association with

PSI, especially the co-migration with PSI-L (PsaL) in all protein preparations (Khrouchtchova et al., 2005). In *Synechocystis* sp. PCC 6803 (Syn6803), the association of TMP14 and PsaL with a high light-induced protein was confirmed by mass spectrometry (Wang et al., 2008b). In 2013, a study presented a detailed description of this family of proteins that functioned in inducing curvature at the edges of granal stacks and named this family Curvature Thylakoid 1 (CURT1), followed by letters A, B, C, or D for each homologous copy of this protein in the *A. thaliana* genome. TMP14 was then designated as CURT1B (Armbruster et al., 2013). It was proposed that the CURT1 protein adjusted thylakoid architecture by inducing membrane curvature at granal margins. Mutations of the *CURT1* gene led to decreases in thylakoid phosphorylation (Armbruster et al., 2013). Studies on the homolog of CURT1 in *Synechocystis* PCC 6803, CurT, revealed that CurT was crucial for shaping the curvature of thylakoid membranes towards the plasma membrane and thereby ensured the assembly of PSII at the cell periphery (Heinz et al., 2016b). It was stated that CURT1-like proteins were needed to generate an efficient thylakoid system in cyanobacteria and proper response to osmotic stress (Heinz et al., 2016b).

In this chapter, studies were undertaken on the localisation, functions, and mechanisms of CURT1 (Syn_1832) in the rod-shaped unicellular cyanobacterium *S.elongatus* PCC 7942. CURT1 in *S. elongatus* PCC 7942 was found to be essential, in contrast to the CURT1 proteins in *A. thaliana* (Armbruster et al., 2013) and *Synechocystis* sp. PCC 6803 (Heinz et al., 2016b). The data revealed that CURT1 plays roles in inducing thylakoid membrane curvature, modifying the overall pattern of the thylakoid membranes, and the densities of the photosynthetic complexes within the membranes.

5.2 Results and discussion

5.2.1 Generation of a CURT1 knockdown strain in Syn7942

The first goal of this research was to study the functions of the CURT1 protein in *S. elongatus* PCC 7942 (Syn7942). The knockdown mutation of the *CURT1* gene was generated (CURT1-KD) with the natural homologous recombination capacity of Syn7942. The genome copy number of Syn7942 in the exponential phase is normally 3–5 (Griese et al., 2011), or more extremely, 1–10 (Zheng and O'Shea, 2017), which has been shown to correlate with cell size (Comai, 2005, Melaragno et al., 1993). Once mutated, Syn7942 cells might have several copies of the mutated gene and the rest as wild-type, meaning the mutant cells could have different segregation levels. Two segregation methods were adopted during gene deletion; cells were grown with supplemented antibiotics either in liquid or on plates. After transferring to fresh media up to five times, no full segregation was obtained in any subculture. In the PCR verifications for segregation, a wild-type band always appeared in addition to the knockout band (Figure 5-1A). However, by doing a Western Blot using a CURT1 antibody (Heinz et al., 2016b), it was established that under the antibiotic pressure, the level of CURT1 in this knockdown strain was below the detection threshold, while the WT strain produced a clear band (Figure 5-1B) (Loaded the same as Figure 5-4, see Chapter 2 Methods). The results demonstrated that the deletion of the *CURT1* gene in Syn7942 was fatal, yet cells did not need a high level of this protein to survive. Consistently, in a previous study on the essentiality of genes in Syn7942, a library of 246913 transposon insertion mutants was created and the insertions were verified by sequencing; researchers found that 718 of the 2723 genes, including the CURT1 gene, were found to be essential under experimental conditions (Rubin et al., 2015). However, a full knockout of the CURT1 gene (Synpcc7942_1832) was achievable in *Synechocystis* 6803 with the addition of 5 mM glucose (Heinz et al., 2016b).

Synechocystis sp. PCC 6803 is capable of both phototrophic and heterotrophic growth, and the knockout was only possible with extra heterotrophic energy.

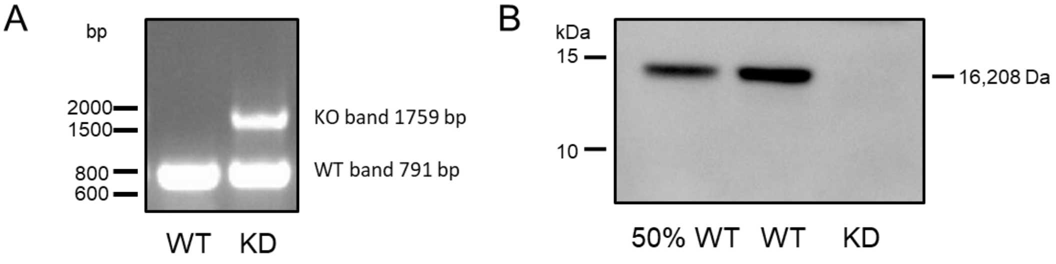

Figure 5-1 Verification of the CURT1 knockdown strains.

The primers used are listed in Supplementary Table 1.

- (A) PCR verification of the CURT1-KD strains shows partial segregation.
- (B) Western blot of extracted thylakoid with α-CURT1 suggests that the knockdown results in a low level of CURT1 that fails to be detected with the corresponding antibody.

5.2.2 Physiological characterisation of the CURT1 knockdown strain

To characterise the functions of CURT1, physiological measurements were performed on the WT and CURT1-KD strain for comparison. In addition to the reduced growth rate (Figure 5-2A), the CURT1-KD strain also had significantly lower chlorophyll concentration compared to that of the WT strain (6.43 ± 0.24 and 3.89 ± 0.33 µM Chl/OD$_{750}$ respectively, $p = 4.23E^{-04}$ n = 3) (Figure 5-2B). The maximum quantum efficiency of PSII (PSII), Fv/Fm, was 0.52 ± 0.00 (n = 3), which was significantly higher than that of CURT1-KD (0.43 ± 0.038, n = 3, p = 0.013) (Figure 5-2C). The lower Fv/Fm indicated that the loss of CURT1 created growth stress for cyanobacterial cells (Kitajima and Butler, 1975, Maxwell and Johnson, 2000). The rapid light response curves for the quantum yield of PSII in control and CURT1-KD are shown in Figure 5-2D, demonstrating that CURT1-KD had a lower quantum yield of PSII compared to WT under high radiance, again implying greater stress, which explained the high level of

CURT1 observed under high light (Figure 5-6). The oxygen evolution rate of CURT1-KD was 9 ± 3.90 µmol O_2 mL^{-1} h^{-1}, compared to WT, which was 6.875 ± 1.89 µmol O_2 mL^{-1} h^{-1}, the difference is not significant ($p = 0.44$, $n = 3$). The variance of respiratory rate was not significant, either, with -1.25 ± 0.57 µmol O_2 mL^{-1} h^{-1} and -0.88 ± 0.57 µmol O_2 mL^{-1} h^{-1} respectively ($p = 0.47$, $n = 3$) (Figure 5-2E). The higher standard deviation in CURT1-KD probably came from the heterogeneity of the CURT1 level due to incomplete segregation.

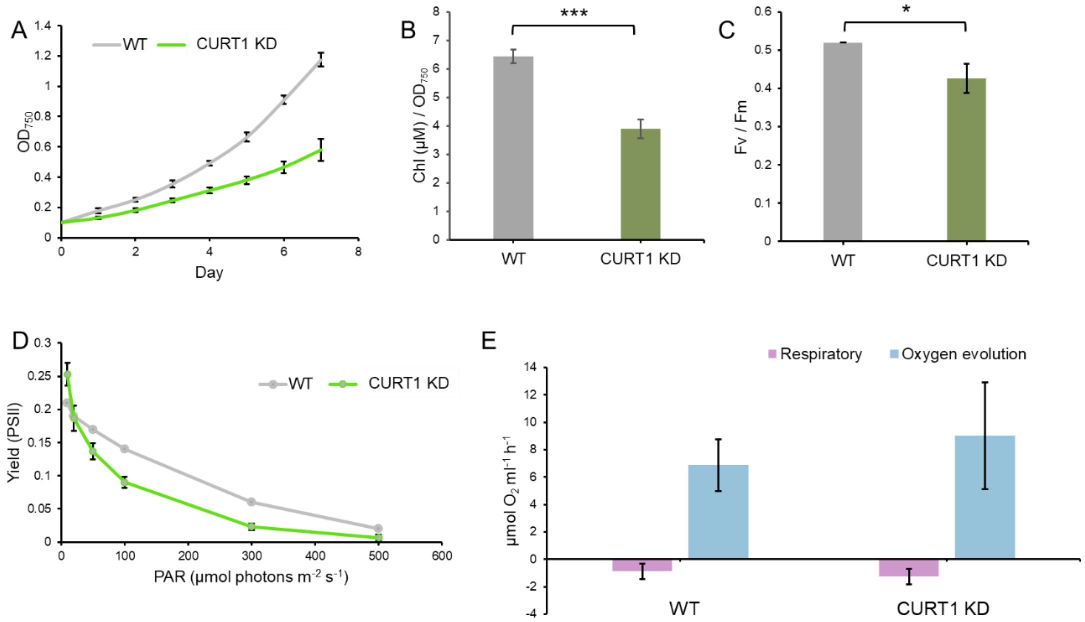

Figure 5-2 Physiological measurements of the CURT1-KD mutant.

Data are shown as means ± SD of three independent experiments. Significant differences were determined with Student's t test. *: $0.01 < P < 0.05$, **: $0.001 < P < 0.01$, ***: $P < 0.001$.

(A) Growth curves of wild-type and CURT1-KD at 30°C with constant 40 µE·m-2·s-1 white illumination.

(B) Chlorophyll-a level comparison between wild-type and CURT1-KD using the methanol extraction method, normalised against OD750.

(C) Fv/Fm measurements (PSII activity) of wild-type and CURT1-KD, with chlorophyll-a level adjusted to 20 mM.

(D) Rapid light curves of wild-type and CURT1-KD under a range of PAR (photosynthetic active radiation), with chlorophyll a level adjusted to 20 mM.

(E) Measurements of oxygen evolution and respiratory rates of wild-type and CURT1-KD, with chlorophyll a level adjusted to 20 mM. The Oxygen evolution was measured with a red LED light source peaking at 650 nm.

The absorbance spectra of the WT and CURT1-KD strains (Figure 5-3A) demonstrated notable differences in pigment content. Chlorophyll a, which absorbs blue light at 440 nm and red light at 680 nm, had a higher content in WT than in CURT1-KD. It is worth mentioning that for the CURT1-KD strain, a blue shift of 5–8 nm from 680 to approximately 673 nm absorption occurred, ascribed to the presence of IsiA (see also Figure 5-4A) (ÖQUIST, 1974, Guikema and Sherman, 1983, Falk et al., 1995, Zhao et al., 2020). Phycobilisomes that absorb light at 600–640 nm also showed a lower level in the CURT1-KD strain (Khanna et al., 1983).

Under excitation at 430 nm (chlorophyll) and 580 nm (phycobilisome), PSI had a fluorescence emission peak at 720 nm (Franck et al., 2002, Vredenberg and Duysens, 1965), and PSII had the typical fluorescence emission at 685 nm at room temperature (Franck et al., 2002). For the fluorescence emission spectra excited at 430 nm (Figure 5-3B), the blue shift of CURT1-KD at 685 nm confirmed the existence of IsiA once more (Andrizhiyevskaya et al., 2002). The lower value of CURT1-KD at 720 nm compared to WT indicated a lower energy transition to PSI. When phycobilisome was excited, IsiA once again brought a higher peak blue-shifted from 685 nm (Figure 5-3C) (Zhao et al., 2020). The fluorescence emission spectra also showed less phycobilisome coupling with PSI at 720 nm. In summary, CURT1 knockdown resulted in more stress in cell growth, the induction of IsiA expression and the reduction in chlorophyll content in cells.

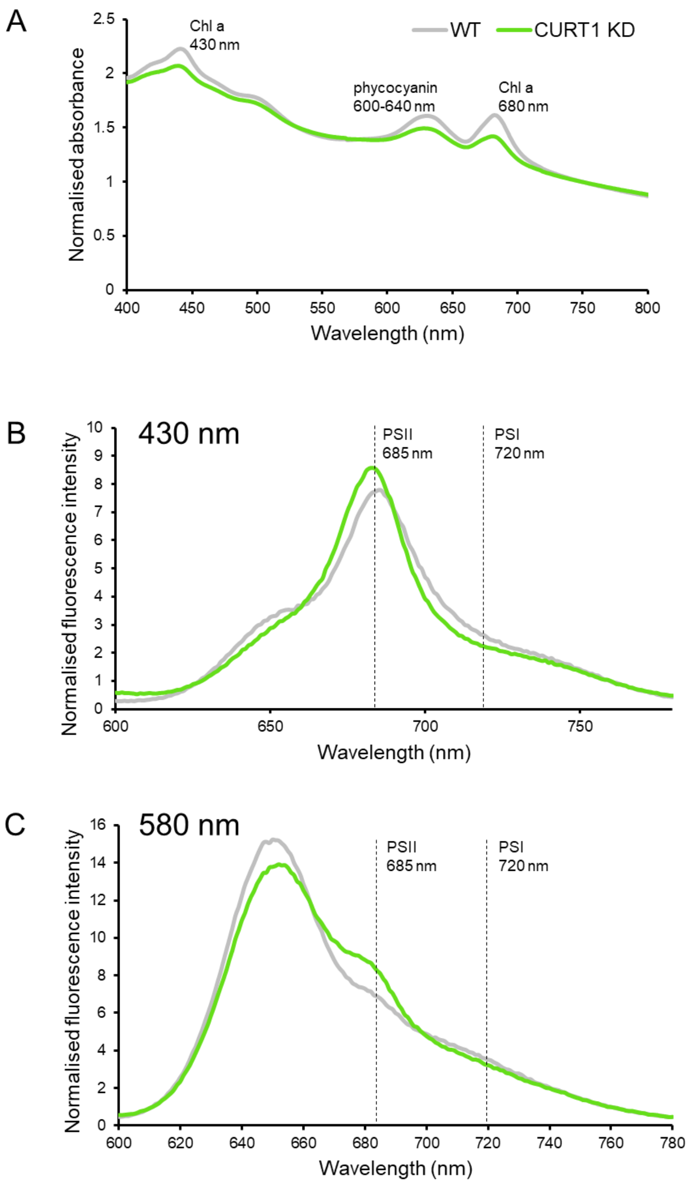

Figure 5-3 Optical spectra of CURT1-KD and wild-type strain.

Data are shown as an average of three independent experiments.

(A) Absorption spectra of WT and CURT1-KD from 400 nm to 800 nm normalised at OD_{750}.

(B) Room temperature fluorescence emission spectra of WT and CURT1-KD, exciting chlorophyll a at 430, detected from 600 nm to 780 nm, normalised at OD_{760}.

(C) Room temperature fluorescence emission spectra of WT and CURT1-KD, exciting phycobilisome at 580, detected from 600 nm to 780 nm, normalised at OD_{760}.

5.2.3 Protein composition of thylakoid membranes was altered by the reduction of the CURT1 level

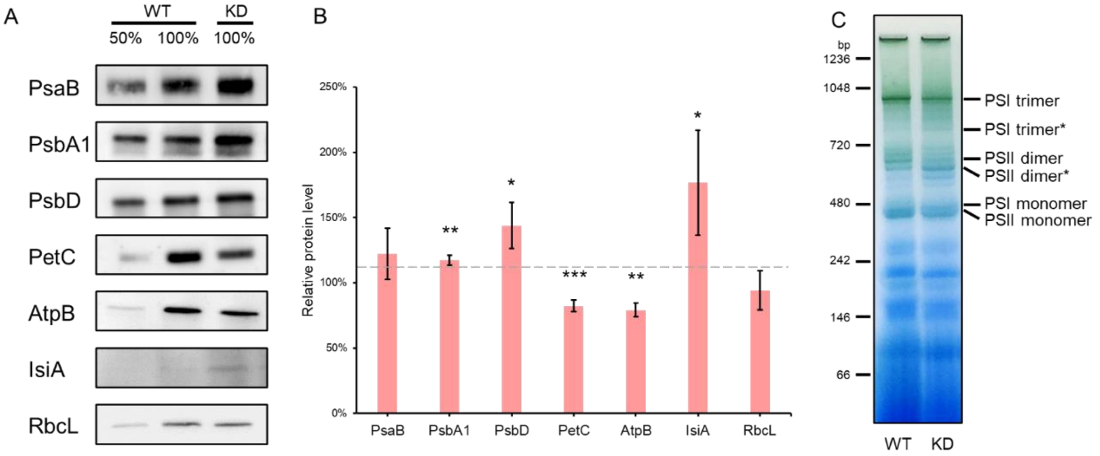

Figure 5-4 Quantification of protein components in the CURT1-KD mutant compared to WT.

(A) Western blots of extracted thylakoid using annotated antibodies (photosynthetic complexes and RbcL, as an internal control).
(B) Quantification of protein abundance from Western blots comparative to WT sample (as indicates with dashed line). Data are shown as means ± SD of three independent experiments. Significant differences are determined with Student's t test. *: $0.01 < P < 0.05$, **: $0.001 < P < 0.01$, ***: $P < 0.001$.
(C) Protein complexes from WT and CURT1-KD separated in a 3-12% linear gradient BN-PAGE. Oligomeric and monomeric forms of photosynthetic complexes are identified. Asterisks designate possible defective complexes.

To understand if the lack of CURT1 affects the protein composition of thylakoid membranes, the abundance of major photosynthetic proteins was determined and compared between the WT and CURT1-KD strains with immunoblotting, normalised by the total protein levels (Figure 5-4). The abundance of PsaB, as a core subunit of PSI, had a higher abundance than that of WT (122.31 ± 19.49%, n = 3, p = 0.058) (Figure 5-4A, B). Two antibodies, α-PsbA1 and α-PsbD, were used to examine the abundance of PSII; both proteins showed a higher abundance in the CURT1-KD strain than in WT. PsbA1 (PSII D1) in the CURT1-KD strain was about 17.45 ± 3.82% higher than WT (n = 3, p = 0.0024). Interestingly, it was found that in *Synechocystis* 6803, CURT1-KO led to the absence of D1 precursor from PSII assembly location, the so-called PratA-defined membranes (Heinz et al., 2016b). If this was a universal rule, it raised the possibility that the assembly of PSII could be incomplete in Syn7942 as well. Another PSII subunit, PsbD, is roughly 143.93 ± 17.71% of the level of WT (n = 3, p = 0.015).

The level of an inner subunit of cyt b_6f, PetC, was significantly lower in CURT1-KD than in WT, as approximately 82.28 ± 4.47% (n = 3, p = $2.76805E^{-06}$). Similarly, AtpB had a lower abundance in CURT1-KD, around 79.13 ± 5.28% (n = 3, p = 0.0064). IsiA as a stress-induced protein (Wilson et al., 2007, Vinnemeier et al., 1998, Bibby et al., 2001, Boekema et al., 2001, Zhao et al., 2020) of which the expression is usually triggered by high light or iron deficiency, had approximately a 2-fold increase (176.70 ± 40.14%, n = 3, p = 0.043). RbcL was used as an internal control protein in the cell's cytosol and showed a 94.19 ± 14.90% (n = 3) of the WT level. There was no significant difference (p = 0.70), indicating that the lack of CURT1 did not have an obvious effect on dark reactions of photosynthesis in the cytoplasm.

This study further used blue native-PAGE to determine the oligomerisation of PSI and PSII. CURT1-KD had fewer fully-assembled but more partially-assembled PSI trimers than WT, and the level of monomers was similar (Figure 5-4C). PSI trimers and monomers were believed to have different functions because under optimal conditions, PSI trimers substantially outnumbered PSI monomers; however, if growth conditions were changed, such as when iron or magnesium is deficient, or growth temperature is altered, the ratio of trimers to monomers decreased (Ivanov et al., 2006, Salomon and Keren, 2011). Therefore, a decline in PSI trimer level might indicate that the cells were suffering from growth stress, consistent with the increase of IsiA mentioned above. Moreover, in CURT1-KD, PSI might form incomplete trimers, shown as several green bands below the correct size. PSII in CURT1-KD had a dimer band with a reduced size compared with that in WT, indicating an incomplete dimer assembly. Altogether, it was concluded that the knockdown of CURT1 impaired the oligomer assembly of PSI and PSII. This means the increased level of individual photosystem subunits shown in Figure 5-4AB could be compensatory.

5.2.4 Subcellular structure of thylakoid membranes in the CURT1-KD strain

We further utilised transmission electron microscopy (TEM) imaging to visualise the cellular morphology of CURT1-KD (Figure 5-5). The first thing noticed was that typical CURT1-KD cells had fewer layers of thylakoid membranes. Under moderate/growth light, WT cells had 3.6 ± 0.5 (n = 12) thylakoid layers, while CURT1-KD had 2.0 ± 0.6 layers on average (n = 21, $p = 5.94E^{-09}$) (Figure 5-5B). It also had a narrower distance between adjacent thylakoid membranes. The distance between thylakoid membranes was typically 0.095 ± 0.013 µm (n = 60) in WT and CURT1-KD0.068 ± 0.012 µm (n = 37) in CURT1-KD ($p = 1.77E^{-16}$) (Figure 5-5C). In 2013, a study on *Synechocystis* 6803 using TEM and small-angle neutron scattering revealed that the distances between thylakoid membranes were under photosynthetic regulations, as both inter-thylakoidal distance and the thickness of lumen increased under the light conditions compared to the dark conditions; the electron transfer chain also had a marginal impact on these distances (Liberton et al., 2013). Taking this into account, CURT1 might affect the thylakoid formation and structure directly or indirectly to manipulate photosynthetic activities. Furthermore, in contrast to WT membranes that were curved smoothly, loss of CURT1 induced rather angular curves, displaying a lack of natural curvature. The lack of curvature was also found in Syn6803 (Heinz et al., 2016b). In summary, CURT1 appeared to affect the thylakoid membrane generation and curvature.

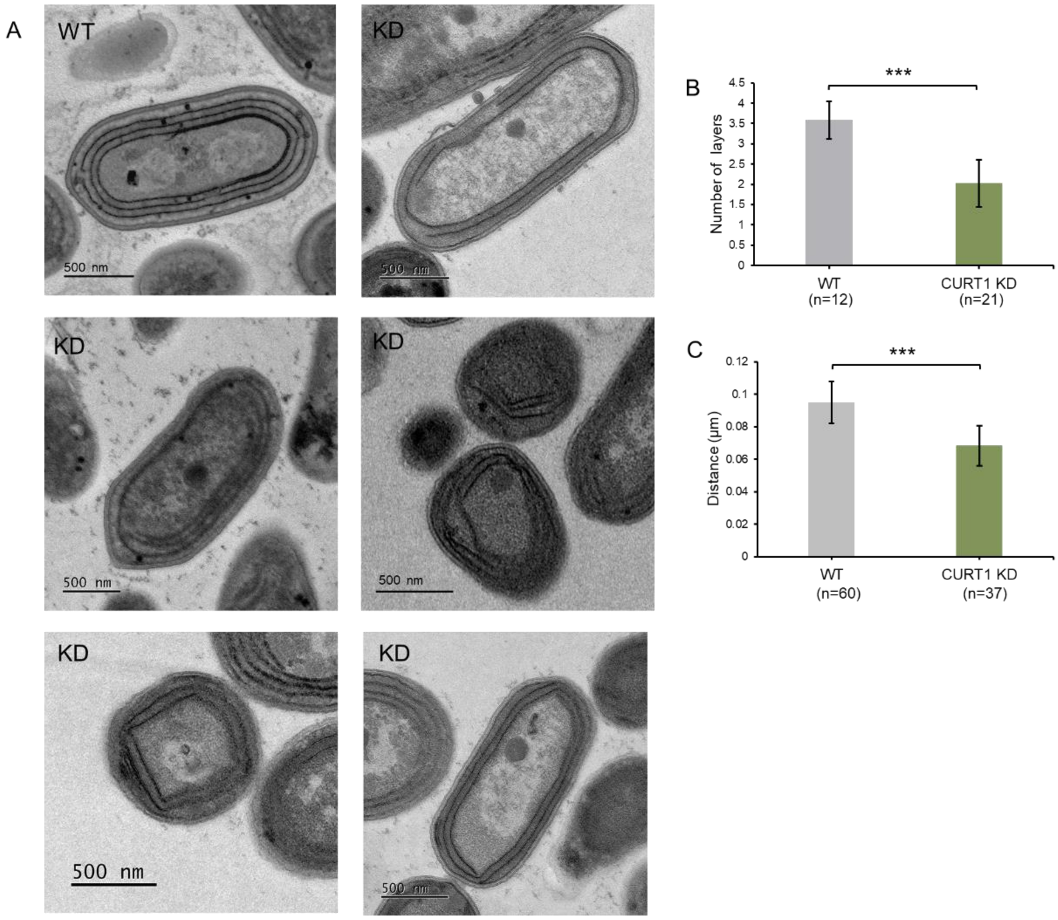

Figure 5-5 Structural analysis of typical wild-type and CURT1-KD cells.

Data are shown as means ± SD. Significant differences are determined with Student's t test. *: $0.01 < P < 0.05$, **: $0.001 < P < 0.01$, ***: $P < 0.001$.

(A) Transmission electron micrographs of wild-type and CURT1-KD cells.

(B) Counts of thylakoid membrane layers in single cells and the comparison between wild-type and CURT1-KD. An incomplete layer of the thylakoid membrane is counted as 0.5.

(C) Measurements of the distance between two adjacent layers of thylakoid membranes of wild-type and CURT1-KD.

5.2.5 The localisation of CURT1 protein

To characterise the *in situ* distribution of CURT1, confocal fluorescence imaging was applied on fluorescently labelled *Syn7942* mutants CURT1-eGFP under three light conditions: low light (LL, 5 $\mu E \cdot m^{-2} \cdot s^{-1}$), moderate/growth light (ML, 40 $\mu E \cdot m^{-2} \cdot s^{-1}$) and high light (HL, 200 $\mu E \cdot m^{-2} \cdot s^{-1}$). The confocal images clearly showed that CURT1 did not distribute evenly across the thylakoid membrane, but particularly at the poles and centre of the cells and along the sides of the cells when light intensity was increased

(Figure 5-6A). In Figure 5-6B, the CURT1 localisation on the thylakoid membrane of a typical dividing cell was demonstrated with the plot profile of GFP and chlorophyll a fluorescence intensity. The localisation of CURT1 also showed heterogeneity under different conditions, with more CURT1 gathering along the side of the cyanobacterial cells under high light (Figure 5-6C).

Different theories proposed that thylakoid membrane elements could be synthesised in the existing thylakoid membrane, plasma membrane or thylakoid centres, and the latter is more conceivable owing to several discoveries about this specialised membrane region (Nickelsen et al., 2011, Rexroth et al., 2011, Kunkel, 1982, Van De Meene et al., 2006). Thylakoid centres are observed as cylinder-shaped structures of 30 nm by 20 nm neighbouring the plasma membrane (Van De Meene et al., 2006). These thylakoid centres are also close to the PratA-defined membrane (PDM), which is defined by the presence of the PSII assembly factor PratA on the plasma membrane (Schottkowski et al., 2009, Frain et al., 2016). Lately, using cryo-focused ion beam (cryo-FIB) and *in situ* cryo-electron tomography (cryo-ET), it has been proved that thylakoids form physical convergence with the plasma membrane at these highly-curved sites in *Synechocystis* spp. PCC 6803 (Rast et al., 2019). In Syn6803, complete knockout of CURT1 led to the disappearance of curvature of the thylakoid membrane towards the PDM (Heinz et al., 2016b). Despite the fact that PDM regions as distinct as those of *Synechocystis* have not been observed in *S. elongatus* PCC 7942, the CURT1-GFP signals apart from the naturally curved poles and centres could possibly indicate more natural curvature, although the physical connections between thylakoid and plasma membrane have not been observed in recent research (Huokko et al., 2021). Moreover, under high light, where the cells get longer and thylakoid membrane layers decline in general (Yu et al., 2015a), CURT1 was expressed much more than the scenario under LL or ML (Figure 5-6). This is consistent with the rapid light curve data (Figure 5-2D), which showed that CURT1-KD bore more pressure than WT under high light.

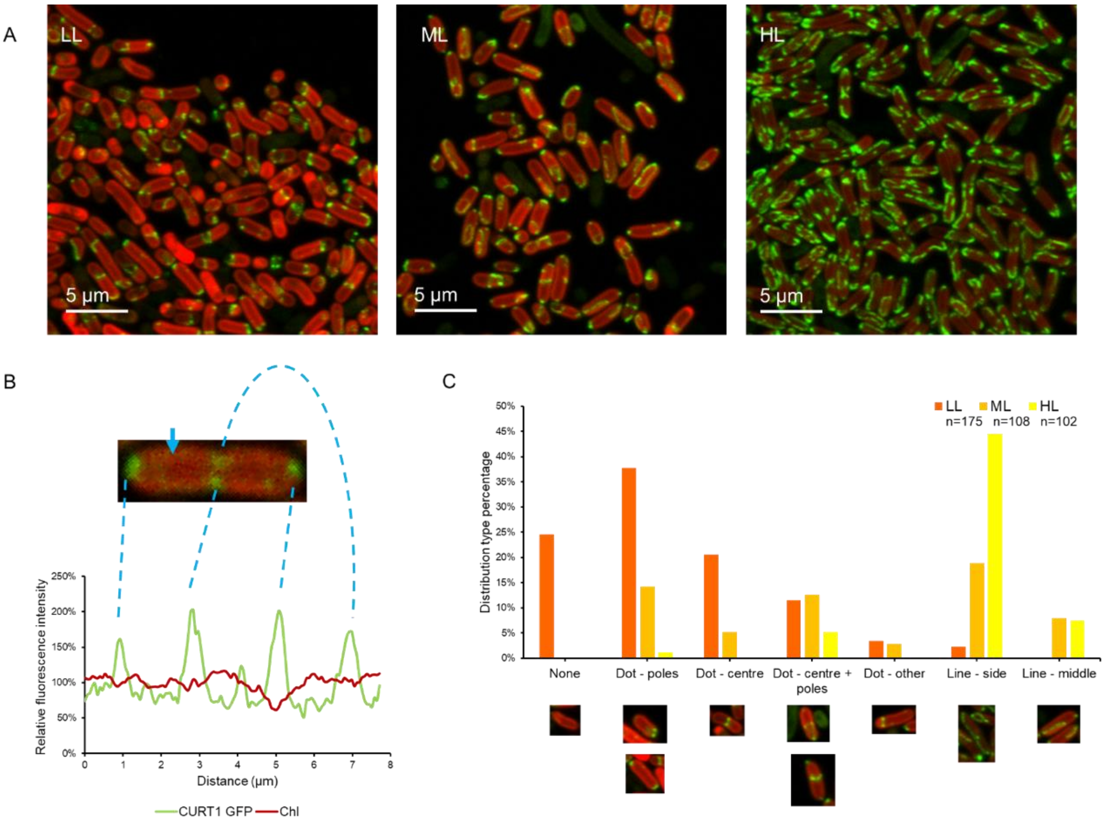

Figure 5-6 Location of CURT1 proteins in *S. elongatus* PCC 7942.

(A) Confocal imaging of the CURT1-GFP strain with fluorescence microscopy under three light conditions—low light—5 µE·m^{-2}·s^{-1}, moderate/growth light—40 µE·m^{-2}·s^{-1} and high light—200 µE·m^{-2}·s^{-1}.

(B) Plot profile of GFP and chlorophyll a fluorescence intensity in a dividing CURT1-GFP cell, normalised with the mean of fluorescence intensity. Each peak of GFP fluorescence intensity corresponds to a spot with strong GFP signals (linked with dashed lines). The measurement starts from the middle of the thylakoid membrane, as the arrow indicates (Distance 0).

(C) Cell counts of each CURT1 distribution type under different light conditions. Cells are categorised into groups based on whether the CURT1-GFP signals formed dots or lines and where the signals are located in each cell. Pictures of typical cells of each group are attached below.

5.2.6 Knockdown of CURT1 affects the abundance and distribution of PSI and PSII

To further characterise how the abundance and distribution of PSI and PSII were affected by the lack of CURT1, PSI and PSII were labelled individually with GFP and analysed with confocal microscopy. Enhanced green fluorescent protein (eGFP) was fused with PsaE in PSI and PsbB (CP47) in PSII. GFP fluorescence and autofluorescence from chlorophyll were measured (Figure 5-7A, 7D and 7F), and the inhomogeneity of these fluorescent intensities was estimated by the standard deviation of data (Figure 5-7E and 7G) as mentioned before (Liu et al., 2012, Casella et al., 2017). Fluorescence intensities of PSI, PSII and chlorophylls were measured in arbitrary units. Compared to a typical PSI-GFP cell that showed great coordination between the PSI-GFP and chlorophyll a fluorescence (Figure 5-7B), some PSI-GFP CURT1-KD cells displayed fluorescence intensities deviated between these two fluorescence signals (Figure 5-7C). The reason remains unknown, but chlorophyll fluorescence comes mainly from PSII at room temperature, and CURT1-KD resulted in the uneven distribution of these two photosystems. From the fluorescence intensity measurements along the thylakoid membrane, it was found that PSI of CURT1-KD strain (6485.85 ± 951.84 a.u., n = 20) was significantly less abundant than PSI in the WT strain (9581.75 ± 1089.43 a.u., n = 20), with a p-value of $1.14E^{-11}$ (Figure 5-7D). This result is consistent with the blue native-PAGE data shown in Figure 5-4C.

We further characterised the homogeneity of such fluorescence distribution by dividing the standard deviation of the fluorescence intensity by the mean value. Distribution of PSI in thylakoids in the CURT1-KD strain (20.26% ± 8.82%, n = 20) exhibited relatively higher heterogeneity than that in the WT background (12.99% ± 6.58%, n = 20), with a p-value of 0.0054 (Figure 5-8E). Though the average chlorophyll a autofluorescence intensity of WT (9132.99 ± 1086.23 a.u., n = 20) was slightly higher than the average chlorophyll a autofluorescence intensity of CURT1-KD (8966.70 ± 1887.47 a.u., n = 20), this difference was not significant (p-value = 0.73) (Figure 5-8F). The inhomogeneity of chlorophyll in the CURT1-KD strain (17.52 ± 7.17%, n = 20) was significantly higher than that of the CURT1-WT strain (12.10% ± 3.86%, n = 20), with p-value equalling to 0.0051 (Figure 5-8G). Altogether, these data imply that CURT1-KD leads to the reduction in PSI abundance and less even distribution of PSI in thylakoids.

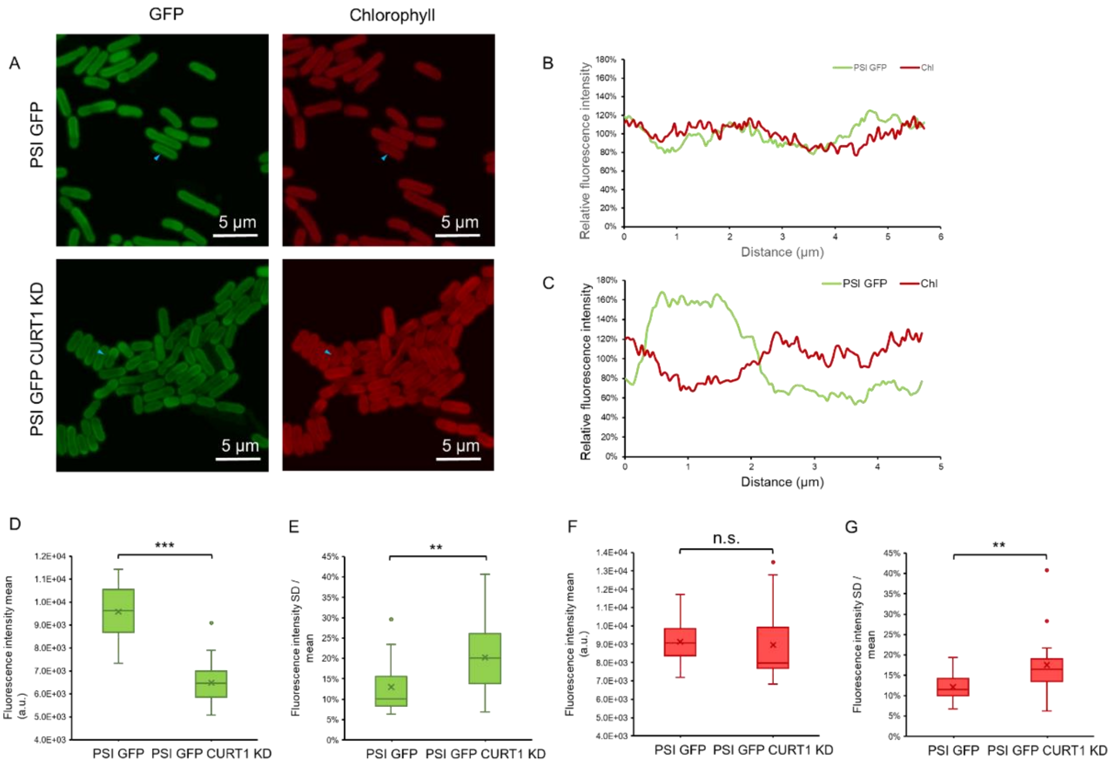

Figure 5-7 Confocal microscopy imaging and characterisation of PSI-GFP cells and PSI-GFP CURT1-KD cells.

Data are shown as means ± SD. Significant differences are determined with Student's t test. *: 0.01 < P < 0.05, **: 0.001 < P < 0.01, ***: P < 0.001.

(A) Confocal microscopy imaging of PSI-GFP and PSI-GFP CURT1-KD cells. Images are taken in two channels—at 500–520 nm for GFP fluorescence (green) and 670–720 nm for chlorophyll a fluorescence (red).

(B) Plot profile of GFP and chlorophyll a fluorescence intensity in the thylakoid membrane of a PSI-GFP cell indicated with the blue triangle, normalised with the mean of fluorescence intensity in each cell.

(C) Plot profile of GFP and chlorophyll a fluorescence intensity in the thylakoid membrane of a PSI-GFP CURT1-KD cell indicated with the blue triangle, normalised with the mean of fluorescence intensity in each cell.
(D) The mean of GFP fluorescence intensity in each cell along the thylakoid membranes with arbitrary units. The values (grey values of fluorescence signals) depend on the sensitivity of the microscope (n = 20 for each group).
(E) The comparison of the standard deviation of GFP fluorescence intensity in each cell between PSI GFP and PSI-GFP CURT1-KD strains. SD values are compared in a ratio to the mean (n = 20 for each group).
(F) The mean of chlorophyll a fluorescence intensity along each side along the thylakoid membranes with arbitrary units. The values (grey values of fluorescence signals) depend on the sensitivity of the microscope (n = 20 for each group).
(G) The comparison of the relative standard deviation of chlorophyll a fluorescence intensity in each cell between PSI-GFP and PSI-GFP CURT1-KD strains. SD values are compared in a ratio to the mean (n = 20 for each group).

To determine the effect of CURT1 on PSII, PSII-GFP was introduced into both wild-type strain and CURT1-KD strain. GFP and chlorophyll a fluorescence intensities were measured as mentioned above, and the mean and standard deviation among the population were calculated. The behaviour of PSII was similar to that of PSI, except that GFP and chlorophyll fluorescence did not show a divergence in the CURT1-KD strain (Figure 5-8A-C). PSII-GFP signal in CURT1-KD strain (8745.73 ± 798.44 a.u., n = 20) was lower than that of the WT strain (9911.62 ± 1034.68 a.u., n = 20), with a significance of p-value = 0.00029 (Figure 5-8D). By calculating the standard deviation of the fluorescence intensity along the thylakoid membranes in whole cells, the distribution of PSII-GFP also demonstrated higher heterogeneity (SD/mean) in CURT1-KD (17.32 ± 6.09%, n = 20) than CURT1-WT strain (11.92 ± 3.28%, n = 20). The p-value was 0.0012 (Figure 5-8E). The chlorophyll a autofluorescence of the PSII labelled strain showed a significant variation between CURT1-KD (10937.72 ± 1050.95 a.u., n = 20) and CURT1-WT (13140.06 ± 1727.81 a.u., n = 20) mutants ($p = 1.99E^{-5}$, Figure 5-8F). In line with what was found in PSI-GFP, the standard deviation of autofluorescence in CURT1-KD (13.85 ± 4.59%, n = 20) was higher than that of CURT1-WT (10.90 ± 3.35%, n = 20), with the significance p-value = 0.026 (Figure 5-

9G). In brief, CURT1-KD resulted in less assembled photosystems in the thylakoid membrane, and the distribution was less even.

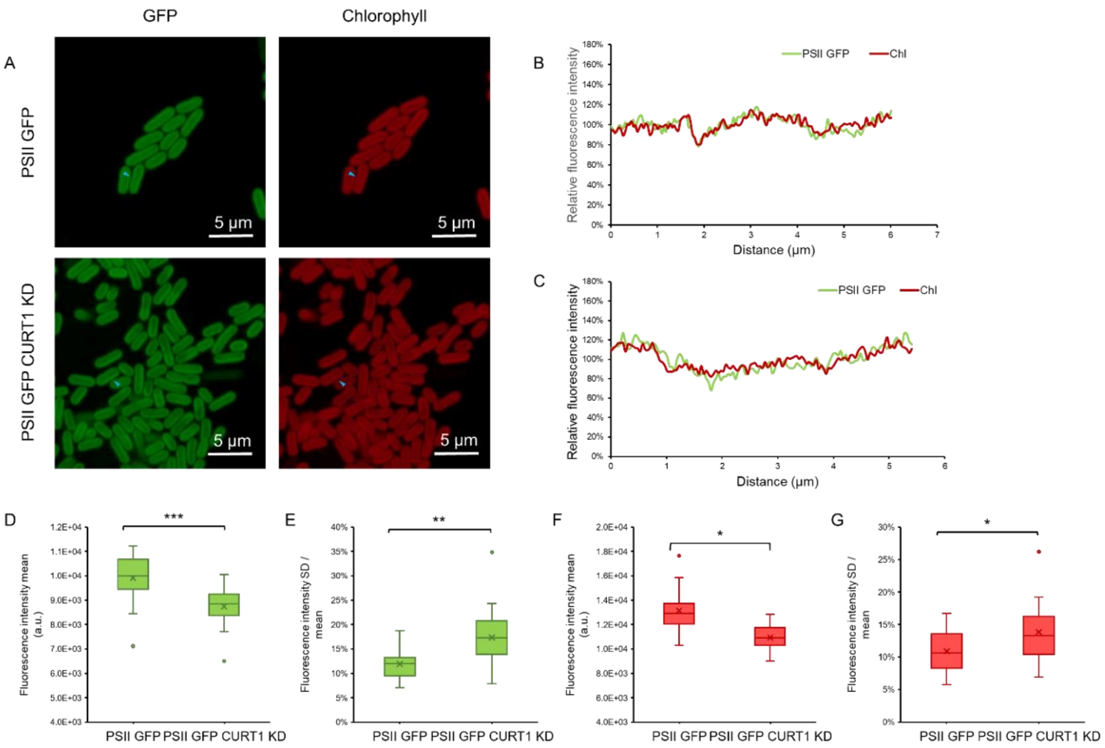

Figure 5-8 Confocal microscopy imaging and characterisation of PSII-GFP cells and PSII-GFP CURT1-KD cells.

Data are shown as means ± SD. Significant differences are determined with Student's t test. *: 0.01 < P < 0.05, **: 0.001 < P < 0.01, ***: P < 0.001.

(A) Confocal microscopy imaging of PSII GFP and PSII-GFP CURT1-KD cells. Images are taken in two channels—at 500–520 nm for GFP fluorescence (green) and 670–720 nm for chlorophyll a fluorescence (red).

(B) Plot profile of GFP and chlorophyll a fluorescence intensity in the thylakoid membrane of a PSII-GFP cell indicated with the blue triangle, normalised with the mean of fluorescence intensity in each cell.

(C) Plot profile of GFP and chlorophyll a fluorescence intensity in the thylakoid membrane of a PSII-GFP CURT1-KD cell indicated with the blue triangle, normalised with the mean of fluorescence intensity in each cell.

(D) The mean of GFP fluorescence intensity in each cell along the thylakoid membranes with arbitrary units. The values (grey values of fluorescence signals) depend on the sensitivity of the microscope (n = 20 for each group).

(E) The comparison of the standard deviation of GFP fluorescence intensity in each cell between PSII-GFP and PSII-GFP CURT1-KD strains. SD values are compared in a ratio to the mean (n = 20 for each group).

(F) The mean of chlorophyll a fluorescence intensity along each side along the thylakoid membranes in c with arbitrary units. The values (grey values of fluorescence signals) depend on the sensitivity of the microscope (n = 20 for each group).

(G) The comparison of the relative standard deviation of chlorophyll a fluorescence intensity in each cell between PSII GFP and PSII-GFP CURT1-KD strains. SD values are compared in a ratio to the mean (n = 20 for each group).

In summary, CURT1 knockdown resulted in the reduction of PSI and PSII content in thylakoid membranes and less even distribution of these photosynthetic complexes. For PSII, the preliminary steps of assembly of PSII dimer—translocation of the D1 protein precursor to the plasma membrane (Ossenbühl et al., 2006, Sachelaru et al., 2013), binding with assembly factor and chlorophyll synthase etc. (Chidgey et al., 2014, Knoppová et al., 2014), all happens at the formerly mentioned PDM region around the thylakoid centre (Heinz et al., 2016a). Less curvature of the thylakoid membrane observed in this study (Figure 5-5) might inhibit protein transportation. The assembly process of PSI, on the other hand, is not as well understood because the assembly happens rapidly (Nellaepalli et al., 2018). Whether or not it is due to a similar reason—less curvature leads to fewer exchange activities on the membrane, eventually less protein and more heterogeneity requires further studies.

5.2.7 Effects of CURT1 knockdown on the lipid composition of thylakoid membranes

The membrane curvature could be attributed to lipids under several scenarios (McMahon and Boucrot, 2015). A typical case is that the structure of a single lipid, determined by its headgroup, length, and saturation of its acyl chains, interferes with the packing of lipids and then influences the shape of membrane monolayers and bilayers (Cooke and Deserno, 2006, McMahon and Gallop, 2005). The lipid constitution of thylakoid membranes in cyanobacteria is highly conserved with that of plants and algae. Monogalactosyldiacylglycerol (MGDG) constitutes approximately half of the thylakoid membrane bilayers, digalactosyldiacylglycerol (DGDG) about 30%, and sulfoquinovosyldiacylglycerol (SQDG) and phosphatidylglycerol (PG) compose 5–12% membrane lipids respectively (Kern et al., 2009).

The lipid composition of the Syn7942 thylakoid membrane regarding these four lipid categories was analysed and compared between WT and CURT1 KD. The overall abundance of the four major classifications of lipids, MGDG, DGDG, SQDG and PD, did not significantly differ between these two groups (Figure 5-9A). Several subcategories of lipids from each major group were surveyed, with varied acyl chain length and saturation (number of double bonds). Most lipid molecules with a specific length and saturation did not present a significant difference between WT and CURT1-KD, except for MGDG (34:2) which has 34 carbons in the fatty acid chain and 2 double bonds. MGDG (34:2) content in CURT1-KD strain was 51.42 ± 13.89% of the WT level ($p = 0.0051$, $n = 3$) (Figure 5-9B). Compared to other lipids in the thylakoid membrane, MGDG has the smallest head group (Coddington et al., 1981). It, therefore, has a conical shape, especially owing to its unsaturated double bonds in its acyl chains. It was further proposed that MGDG stabilised negative curvature (Kollmitzer et al., 2013, Booth and Curnow, 2009). MGDG plays roles in both maintaining concave regions and packing hydrophobic proteins in flat bilayer regions through inverted micelles (Murphy, 1982); and it was stated to help form the highly curved membrane junctions between adjacent bilayers (Seiwert et al., 2018). Based on the effects of CURT1 knockdown on the membrane curvature and this specific MGDG (34:2) abundance, it suggested that MGDG with double bonds might interfere with membrane curvature.

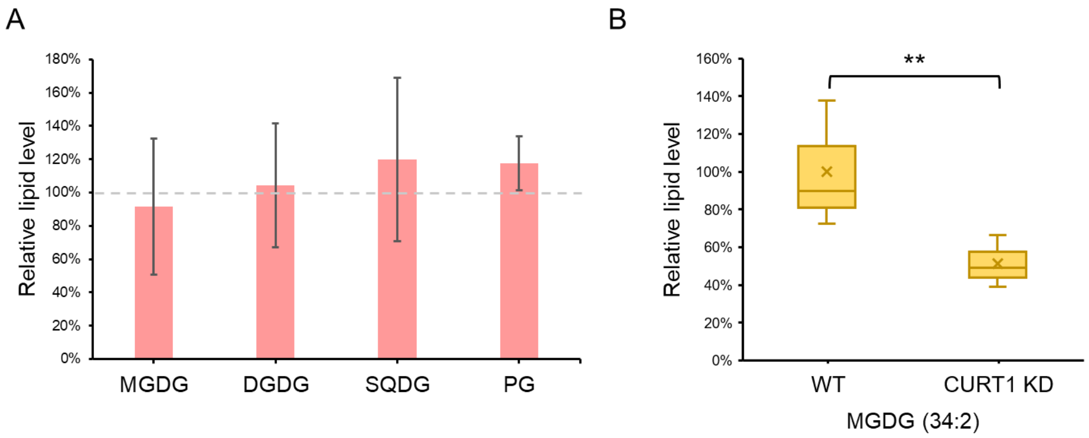

Figure 5-9 Levels of lipids in WT and CURT1-KD thylakoid membranes.

Data are shown as means ± SD of three independent experiments. Significant differences are determined with Student's t test. *: $0.01 < P < 0.05$, **: $0.001 < P < 0.01$, ***: $P < 0.001$.

(A) The summed levels of monogalactosyldiacylglycerol (MGDG), digalactosyldiacylglycerol (DGDG), sulfoquinovosyldiacylglycerol (SQDG) and phosphatidylglycerol (PG) on the thylakoid membranes of CURT1-KD strain did not show significant differences with WT.

(B) The level of a specific lipid type MGDG (34:2) is significantly lowered in the CURT1-KD strain.

5.2.8 Structural characterisation of CURT1

The original goal of structural studies was to resolve the molecular structure with protein crystallography and X-ray diffraction. After trials with different overexpression vectors (pETDuet, pETM-11, pAM2991, pET-26b etc.) and different expression competent cells (BL21(DE)3, Rosetta, C41, C43 etc.), conditions were optimised for IPTG induction of CURT1 overexpression in *E. coli*. with an N-terminal polyhistidine tag. CURT1 was then sampled for purification with different strategies (different buffers, e.g. PBS and Tris, with TEV digestion or without etc.). The final strategy was deploying pETDuet as the vector, BL21(DE)3 as the expression cell, using ÄKTA pure protein purification system (GE Healthcare Life Sciences) with a HisTrap™ High Performance Column and a Sephacryl S-200 High Resolution size exclusion chromatography resin. The concentration of the purified protein was 7.288 mg/mL. The purity of CURT1 was verified with SDS-PAGE and Western blot (Figure 5-10A), and high-performance liquid chromatography (HPLC) detecting at 220 nm (absorption by peptide bonds and most amino acids), 254 nm (phenylalanine) and 280 nm (tyrosine and tryptophan) (Figure 5-10B). During crystallography screenings carried out in five commercial crystallisation trays—Structure, RUBIC, Memgold, Memtrans and Morpheus, crystals formed under one condition (0.2 M magnesium chloride hexahydrate, 0.1 M Tris, pH 8.5, 30% w/v PEG 4000) (Figure 5-10C). To obtain X-ray quality crystals, about 100 conditions were tested around the specific conditions, regarding different protein concentrations, pH, magnesium chloride, and PEG 4000 concentrations (see methodology), but no high-quality crystals were observed in three months.

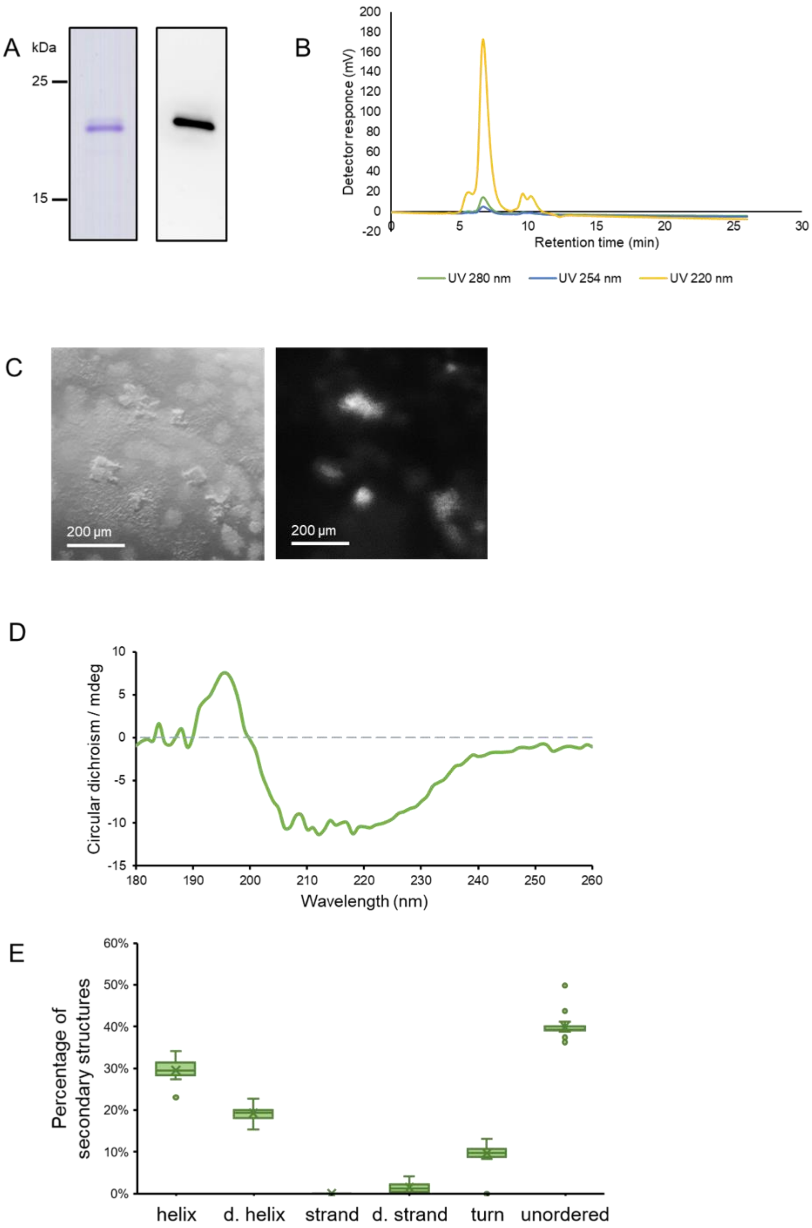

Figure 5-10 Purification and structural characterisation of CURT1.

(A) Purification of CURT1 (with His-tag affinity chromatography and size exclusion chromatography) showed a single band in SDS-PAGE (left) and is detected with anti-His-tag in Western blot (right).
(B) HPLC purity examination of purified CURT1.
(C) Forms of crystals in crystallisation screening with purified CURT1 (left) and UV imaging of crystallisation (right).
(D) Circular dichroism data or purified CURT1.
(E) Percentage of secondary structures, including α-helix—α- and 3_{10}-helices (helix), distorted α-helix (d.helix), β-strand (strand), distorted β-strand (d.strand), turn (turns and bends) and unordered (non-continuous residues assigned to a secondary structure), obtained from the Dichroweb database using COTIN method. Data are shown as means ± SD of the top 35 models.

To characterise the structure, circular dichroism spectroscopy was exploited. CD spectroscopy is a well-studied biophysical tool for the structural analysis of biopolymers such as proteins and nucleic acids; it has advantages for proteins that prove difficult to crystallise. CD signals at around 222 nm represent n → π* transitions, and signals at 190-208 nm indicate π → π* transitions (parallel and perpendicular orientations) (Miles and Wallace, 2016). Alpha-helices produce a minus peak at 208 and 222 nm, while beta-sheets show a minus peak at 216 nm and a plus peak at 195 nm, and random coils are presented as a minus peak at 200 nm and a plus peak at 212 nm. The CD data (Figure 5-10D) of CURT1 was searched against the DichroWeb database (Lobley et al., 2002, Whitmore and Wallace, 2004, Whitmore and Wallace, 2008) using CONTINLL algorithms (Provencher and Gloeckner, 1981, Van Stokkum et al., 1990), and the secondary structures were presented as the average ratios of the top 35 models (Figure 5-10E). The data indicated that the majority of this protein is composed of alpha-helices and a great percentage of random coils (Figure 5-10).

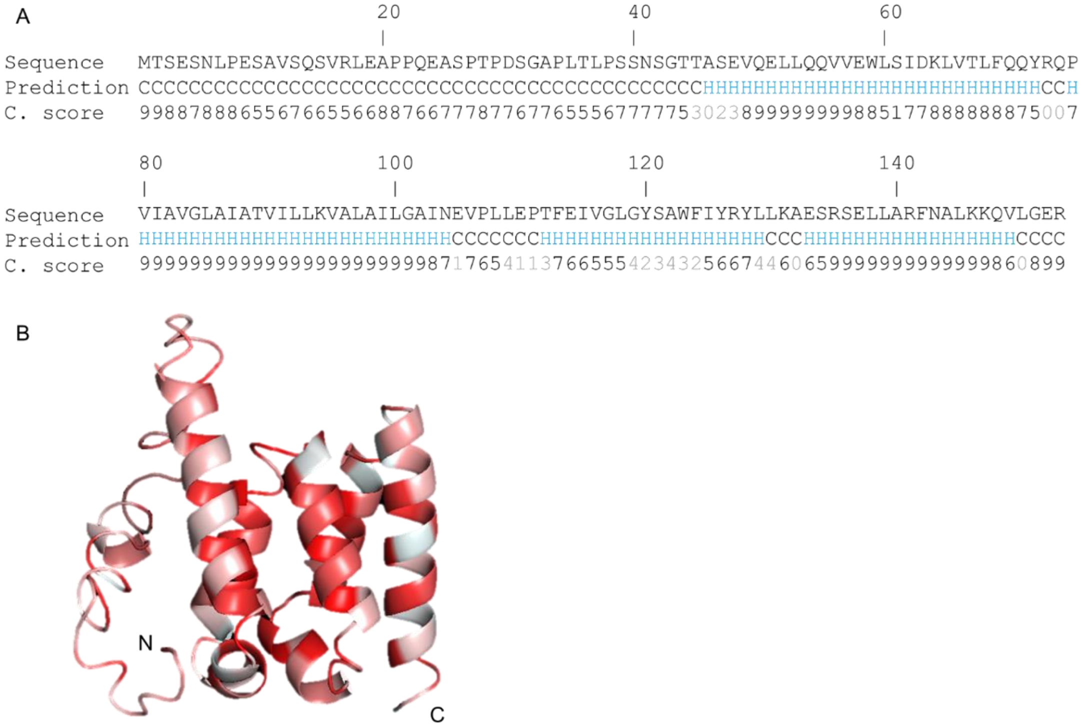

```
                                20                                      40                                      60
                                 |                                       |                                       |
Sequence   MTSESNLPESAVSQSVRLEAPPQEASPTPDSGAPLTLPSSNSGTTASEVQELLQQVVEWLSIDKLVTLFQQYRQP
Prediction CCCCCCCCCCCCCCCCCCCCCCCCCCCCCCCCCCCCCCCCCCCCCCHHHHHHHHHHHHHHHHHHHHHHHHHHHCCH
C. score   9988788865567665566887667778776776555677777530238999999999885177888888875007

           80                                      100                                     120                                     140
           |                                        |                                       |                                       |
Sequence   VIAVGLAIATVILLKVALAILGAINEVPLLEPTFEIVGLGYSAWFIYRYLLKAESRSELLARFNALKKQVLGER
Prediction HHHHHHHHHHHHHHHHHHHHHHHHHCCCCCCCHHHHHHHHHHHHHHHHHHCCCHHHHHHHHHHHHHHHHHCCCC
C. score   99999999999999999999999871765411376655542343256674460659999999999999860899
```

Figure 5-11 Structural predictions of CURT1 using I-TASSER.

(A) Prediction of secondary structure using I-TASSER. H - Helix (blue), C-Coil. C. score is the confidence score from 1–9, with a higher score meaning higher confidence. A score below 5 is coloured in grey.
(B) The confidence score is -2.99 (range [-5,2]). Colouration is based on the hydrophobicity of residues: red designates hydrophobic residues and white designates hydrophilic residues.

In agreement with the CD data, protein structure prediction using the I-TASSER server (Zhang 2008, Roy, Kucukural et al. 2010, Yang, Yan et al. 2015) showed that the alpha helices and random coils made up the majority of CURT1 (Figure 5-11). For proteins that span membranes, individual alpha-helices or beta-sheets tend to be significantly longer than those found in typical soluble proteins; the sizes of these two categories of alpha-helices are 25–30 residues (30–50 nm, ≥7.5 turns), and 10 - 12 respectively (Miles and Wallace 2016). In this model, these alpha-helices are shorter than membrane-span proteins, and they have distinct hydrophilic regions (coloured white in Figure 5-11B), making them likely to be amphipathic proteins. Previous studies have revealed that copious proteins with amphipathic helices could be involved in membrane curvature and vesicular transport through protein motif insertion and regulation of lipid binding; similar proteins include amphiphysin, Arf proteins, epsin, endophilin etc., which act as a wedge and have different lipid binding abilities (Drin and Antonny, 2010, McMahon and Boucrot, 2015). In *Synechocystis*, CURT1 was detected in the convex side of thylakoid membranes (Heinz et al., 2016b). These data together suggested that the shape of CURT1 functioned as a wedge and induced curvatures in the thylakoid membrane.

5.3 Concluding remarks

In summary, these data provided insights into the functions of the CURT1 protein on the thylakoid membrane and Syn7942 cells in terms of physiology and morphology. This study began the process of dissecting the primary structure of CURT1 using circular dichroism and discussed the mechanisms of curvature formation based on CURT1 structural information and lipid data. By using genetic engineering, physiological measurements, protein quantification, transmission electron microscopy, fluorescence microscopy, and structural characterisation, this study of CURT1 suggested that CURT1 is essential for the survival of Syn7942 and a lower level of CURT1 affects the assembly of photosystems and impairs the photosynthetic abilities. Compared to the studies in *Synechocystis* 6803 (Heinz et al., 2016b), where CURT1 was found to be non-essential when cells were supplemented with glucose, it was found that CURT1 was indispensable in Syn7942. Knockdown of the CURT1 gene resulted in changes in the morphology of thylakoid membranes in terms of reduced curvatures and the number of layers. It was also found that lack of CURT1 impaired the photosystem assembly, and the increased level of PSI and PSII subunits in the CURT1-KD strain could be compensatory, which is different from the declined level of photosystem proteins in Syn6803 (Heinz et al., 2016b). The localisation of CURT1 showed that rather than a dispersed distribution, accumulations were found at the poles of cells, centres of dividing cells, and along the sides of cells, especially under high light, designating the positions where thylakoid membrane curvature naturally occurs. Moreover, with circular dichroism and lipid composition data, the primary structure of CURT1 was proposed and the hypothesis about how thylakoid membrane curvatures were formed with CURT1 was suggested (Figure 5-12). CURT1 may induce curvatures into the thylakoid membrane through the interplay between lipid composition and protein structure. Lipidomics showed that a particular MGDG category (34:2, which has 34 carbons in the fatty acid chain and 2 double bonds) is significantly higher in WT than in CURT1-KD, and its conical shape stabilises negative curvatures.

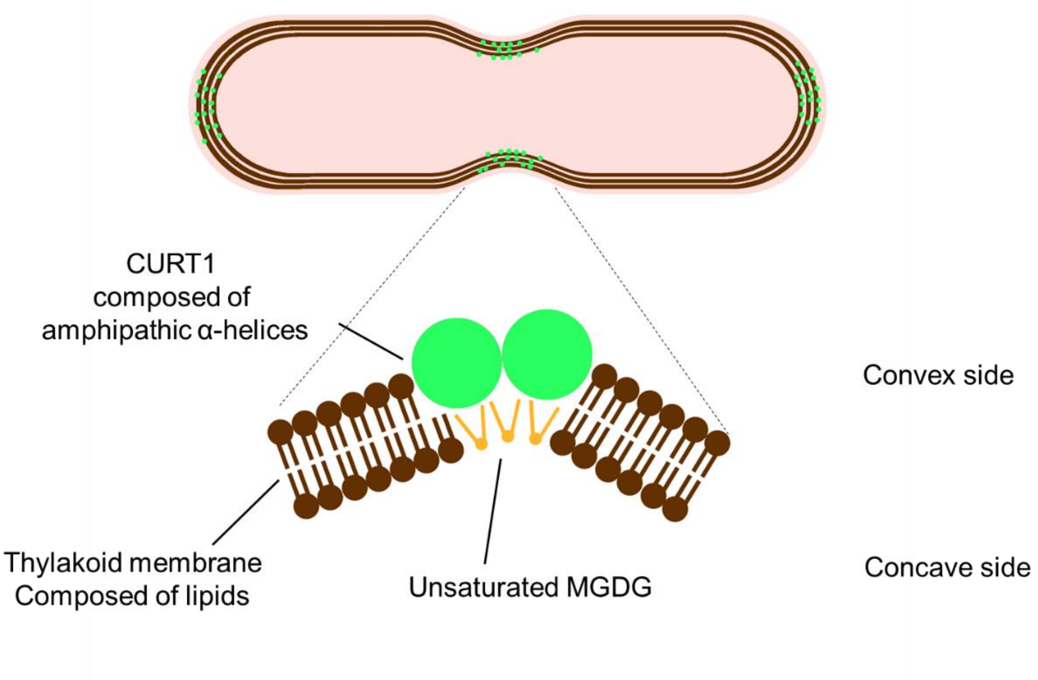

Figure 5-12 The hypothetical mechanism of CURT1 protein inducing curvature in the thylakoid membrane of a dividing Syn7942 cell.

CURT1 proteins inhabit the thylakoid membrane and are commonly found in the middle of dividing cells and at the cellular poles where the natural curves of the thylakoid membrane occur. As a protein made of amphipathic α-helices, CURT1 can act as a wedge on the convex side to induce curvatures in the thylakoid membrane. While one-shaped unsaturated MGDGs stabilise curvature on the concave side of the thylakoid membrane.

In contrast to the results reported in *Arabidopsis* (Khrouchtchova et al., 2005) and *Synechocystis* (Wang et al., 2008b), where CURT1 was proposed to be a newly discovered subunit of PSI, it was shown that CURT1 was not detected in any of the pull-down assays of photosynthetic complex-GFP strains, including PSI-GFP, PSII-GFP, Cyt b_6f-GFP, and ATPase-GFP (Chapter 3). The results suggested that CURT1 is not a permanent component of PSI or any of these four complexes, and it does not form a constant and direct interaction with any of them. Instead, it could affect these photosynthetic complexes in an indirect manner.

The discovered connection between fewer curvatures and fewer numbers of thylakoid membrane layers is intriguing, as the origin of thylakoid membrane biogenesis is still a subject of debate. Whether these curvatures are involved in thylakoid generation remains to be verified. Dual-labelling of CURT1 and PratA with different fluorescence proteins would possibly lead to insights regarding why CURT1 creates curvatures from the thylakoid membrane towards the plasma membrane. However, in a recent paper, direct contact between the plasma membrane and the thylakoid membrane was not detected (Huokko et al., 2021). If the curvatures aid with protein transportation, the flowing rate of proteins could change and be observed under fluorescence recovery after photobleaching (FRAP) analysis, especially at those sites where CURT1-GFP shows a crowded distribution, e.g., at the poles or centres of cells.

Another intriguing experiment could be the overexpression of CURT1. In this study, an IPTG-inducible cloning vector pAM2991 (Ivleva et al., 2005) was deployed for overexpression of CURT1 in both *E. coli* and *S. elongatus* PCC 7942. The transformation of *E. coli* resulted in successful CURT1 expression, but the transformation of cyanobacteria failed several times. This failure in generating the overexpression mutant is similar to that found in *Synechocystis* 6803 (Heinz et al., 2016b). If the overexpression could work in the future, the structure of thylakoid would be examined with TEM and physiological experiments would be conducted to see if the enhancement of CURT1 can be a route to photosynthetic efficiency improvement.

6 Chapter 6 Discussion and concluding remarks

Both the light reactions of photosynthesis and respiration take place in cyanobacterial thylakoid membranes that are densely packed with a series of photosynthetic and respiratory complexes. AFM data disclosed that over 3/4 of the thylakoid membrane surface is occupied by different proteins (Casella et al., 2017). A fundamental question about the cyanobacterial thylakoid membrane is how the photosynthetic complexes are laterally associated and organised. These arrangements, along with the regulation and dynamics of native thylakoid membranes, are vital for efficient light-harvesting and energy transduction. In this study, a combination of techniques was used to enrich the understanding of this information. This work incorporated immunoprecipitation, mass spectrometry and AFM to identify interactions and associations among thylakoid membrane complexes (Chapter 3); with confocal microscopy, the correlations between PSI and other photosynthetic and respiratory complexes were characterised at ~200 nm-scale lateral resolution (Chapter 4); it was further analysed how a thylakoid membrane regulatory factor, Curvature Thylakoid 1 (CURT1) exerts influences on the architecture of the membrane and photosynthetic activities using a combination of physiological characterisation, transmission electron microscopy, confocal microscopy, circular dichroism, and lipid analysis (Chapter 5). In the longer term, advanced knowledge of the protein organisation and interplay of the photosynthetic machinery may help inform the rational design and engineering of artificial photosynthetic systems to supercharge energy production.

6.1 Supercomplex association of photosynthetic complexes in cyanobacteria

The lateral organisation and close association of photosynthetic complexes in native thylakoid membranes are vital for efficient electron transfer and energy transduction.

This study reported a method integrating immunoprecipitation, mass spectrometry and atomic force microscopy to identify the inter-complex associations of photosynthetic complexes in thylakoid membranes from the cyanobacterium *S. elongatus* PCC 7942 (Figure 3-1). In this work, numerous outcomes were achieved. The ratio of photosynthetic complexes participating in supercomplexes (Figure 3-6), the preferable association patterns between individual photosynthetic complexes and binding proteins involved in the complex-complex interfaces were characterised (Figure 3-7). Therefore, it was possible to propose the structural models of photosynthetic complex associations that promote the formation of photosynthetic supercomplexes. Suggested from this work are hypothetical supercomplex models between photosynthetic complexes and between PSI and NDH-1 (depicted in Figure 6-1). Their existences were further validated with AFM (Figure 3-8 and 3-9). This study also identified other potential binding proteins within the photosynthetic complexes, suggesting a highly interconnected network associated with thylakoid membranes (Table 3-1).

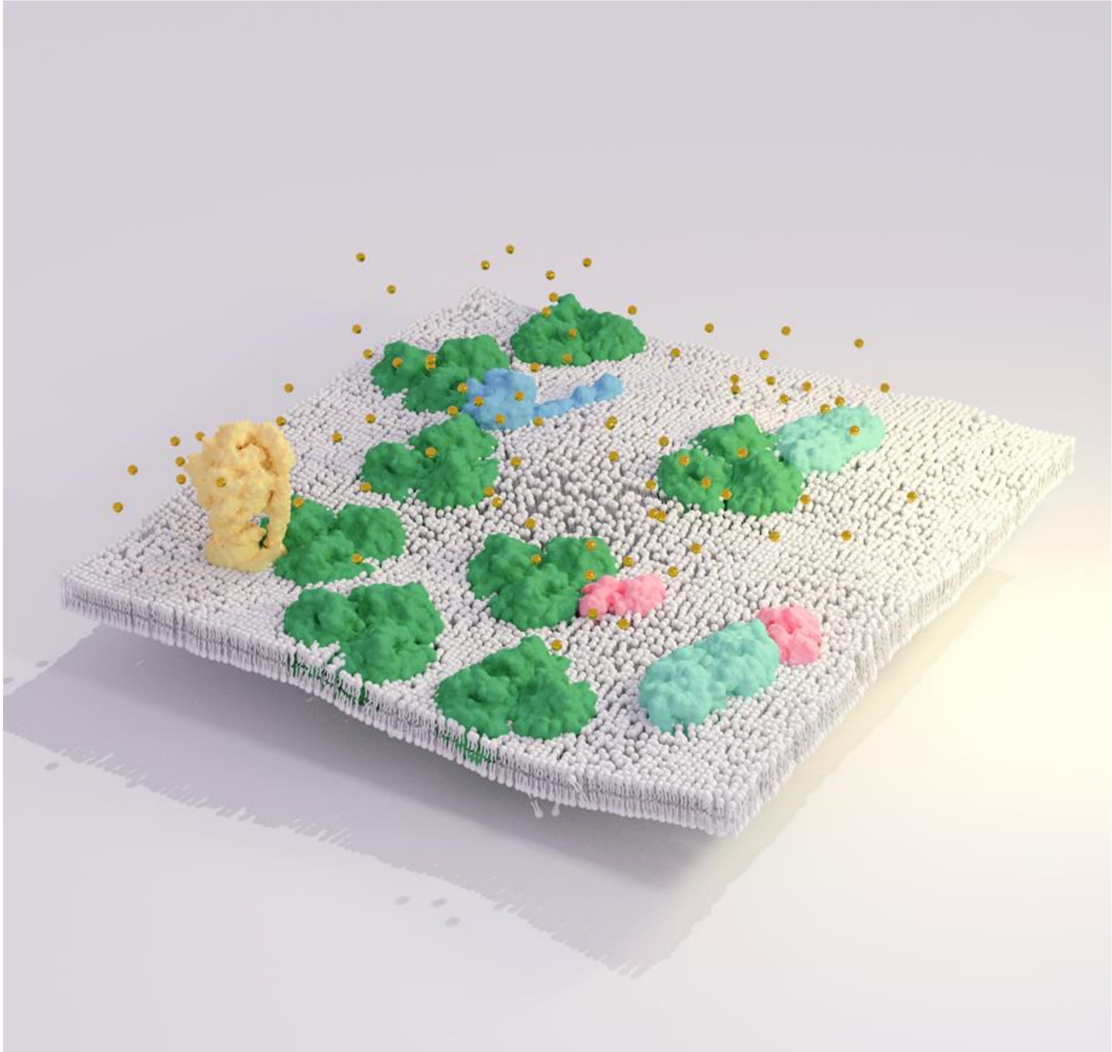

Figure 6-1 Hypothetical 3D model of supercomplex constitutions in the thylakoid membrane.

The most abundant photosynthetic complexes, PSI, are depicted as trimers and coloured deep green; PSII dimers are coloured light cyan. Cytochrome b_6f dimers are coloured light pink; ATP synthases are coloured yellow, and NDH-1 complexes are coloured blue.

Specifically, it was found that a considerable amount of PSI and PSII form supercomplexes, around 9.9% of PSII complexes were found to associate with approximately 1.72% PSI. Similarly, but with lower abundance, cytochrome b_6f formed mega complexes with both PSI and PSII, 4.12% Cyt b_6f formed an association with 0.31% PSI, while 2.01% cytochrome b_6f was associated with 1.98% PSII. It was also found a substantial share of PSI complexes were binding with NDH-1. The composition of the identified supercomplexes is consistent with previous studies about PSI–PSII supercomplexes (Bečková et al., 2017, Liu et al., 2013) and PSI–NDH-1 supercomplexes (Kouřil et al., 2014). This study quantified the ratio of photosynthetic complexes participating in supercomplexes for the first time, verifying the association patterns with AFM. Moreover, other proteins that have potential interactions with PSI, PSII, Cyt b_6f, and ATPase were identified, e.g., the iron stress-induced chlorophyll-binding protein IsiA, the bicarbonate transporter subunit CmpA, the chromosome partition protein Smc, the secretion protein HlyD, and peptidoglycan glycosyltransferase were shown to bind to PSI. Three of the four FtsH proteins, the PSI assembly protein Ycf4, and the bicarbonate transporter SbtA are associated with PSII. Cyt b_6f may interact with DNA topoisomerase TopA and geranylgeranyl reductase, ATPase has a close relationship with the chaperon protein DnaK3, etc. This study provides insights into the interacting network among photosynthetic complexes and other proteins that provide mechanistic understandings of the physical interconnections of photosynthetic complexes and potential partners, which are crucial for efficient energy transfer and physiological adaptation of photosynthetic apparatus.

6.2 Localisation of photosynthetic and respiratory complexes in the thylakoid membrane

The heterogeneity of the cyanobacterial thylakoid membrane has been reported (Sherman et al., 1994, Zhao et al., 2020), and it was found that photosynthetic complexes and respiratory complexes are arranged into functional domains to augment their harmonisation and coordination (Zhao et al., 2020). Those findings raised a question regarding how photosynthetic complexes are organised in the thylakoid membrane and whether those complexes with related functions tend to colocalise. The presented study was designed to determine the distribution of photosynthetic and respiratory complexes, and how it is related to PSI. Dual-labelling, confocal fluorescence imaging, and multiple regression analysis were combined to reveal that the studied thylakoid membrane protein complexes, including PSII, ATPase, NDH-1 and Cyt c oxidase, all appeared to have a tendency to colocalise with PSI. The functionally related pairs, such as PSI–PSII in the light (Figure 5-2), and PSI–NDH-1 (Figure 5-4) showed an even higher covariance in terms of colocalisation.

This is the first work showing the dual labelling of major photosynthetic and respiratory complexes in cyanobacterial thylakoid membranes. Consistent with the literature that observed the PSI could be in the same domains as PSII, Cyt b_6f, ATPase and NDH-1 (Zhao et al., 2020), localisation associations between PSI and other photosynthetic and respiratory complexes were found, and the colocalisation relationships were further characterised with thousands of data points and achieved a calculation of the correlation coefficient of those interactions on a whole-cell level. One open question is how close these complexes are to each other. The choice of dual-labelling tags, CFP and YFP as a pair, leaves ample room for further progress in determining the distance between each pair of labelled proteins using FRET measurements.

These data provide molecular insights into the interactions and dynamics of photosynthetic and respiratory proteins in cyanobacterial thylakoid membranes and will potentially help answer the questions regarding how the thylakoid membrane complexes are coordinated while the fluidity is maintained and at what time and space scale electron transport occurs. Such knowledge will have implications for future studies of photosynthetic optimisation and potential artificial thylakoid membrane designs.

6.3 Roles of Curvature Thylakoid 1 protein in mediating thylakoid membrane structure and photosynthetic function

The formation of membrane curvatures is a prerequisite for the shaping of cells, organelles, and vesicles, and is crucial for cellular activities such as cell division and membrane trafficking. In the thylakoid membrane of higher plants, the generation of curvatures at the grana margins increases the surface area of the appressed membrane region, and this function is ascribed to the protein Curvature thylakoid 1 (CURT1), the loss of which impairs the photosynthesis pleiotropically (Armbruster et al., 2013). Intending to dissect the functions of CURT1 in *S. elongatus* PCC 7942, this study used a series of physiological measurements, protein quantifications, transmission electron microscopy, fluorescence microscopy, lipid mass spectrometry, protein purification and structure analyses to elucidate novel knowledge that improves the understanding of the impact of CURT1 on cellular morphology and photosynthesis, and primarily proposed a hypothetical mechanism for CURT1 causing curvatures in thylakoid membranes.

Syn7942 cells with a low level of CURT1 displayed altered morphology compared to WT, including fewer curves, fewer layers of thylakoid membranes, and narrower space between layers (Figure 5-5). Fluorescence microscopy showed that the preferable localisations of CURT1 are the cellular poles where natural curves occur and in the middle of elongated cells where curves are required for cell division (Figure 5-6). CURT1 could also be found along the thylakoid membrane, perhaps indicating other curvatures that were not clearly shown using the TEM (Figure 5-6, Figure 5-7). CURT1 knockdown diminishes photosynthetic efficiency, probably due to a lower level of fully assembled PSI and PSII observed in blue native gel (Figure 5-4) and confocal microscopy (Figure 5-7 and Figure 5-8). This thesis has proposed a hypothetical mechanism of the CURT1 protein inducing curvatures in the thylakoid membrane, with lipid composition data (Figure 5-9), circular dichroism (Figure 5-10), and structure modelling (Figure 5-11). This research has deepened the understanding of thylakoid membrane curvature generation and the pleiotropic functions of CURT1 underlying the efficiency of photosynthesis, enabling direct interferences and artificial manipulation of the thylakoid membrane curvatures to achieve better photosynthetic efficiency.

Supplementary Table 1 Primer list

PSI GFP, YFP, CFP generation Subunit: PsaE	
FpsaE	CGAGGTAGCGCGACAGATAG
RpsaE	GCCATAGACCCACGCTTGAC
RFpsaEGFP	GAAGCAGAATTACAAGTGGTTGCAGCAGCCGCCAAAAACTGCCGGGCCCGGAGCTGCC
RRpsaEGFP	GTAGCCGTTTCAGGAACCTCTTGTGAAGACAGAAGCAGTATTCCGGGGATCCGTCGACC
FpsaEseg	CGCGTGGTGATAAGGTTCGG
RpsaEseg	GAGTAAGACTTCGCCACCTG
PSII GFP, YFP, CFP generation Subunit: PsbB (CP47)	
FCP47	CTACAAAGCGCTGCGGATGG
RCP47	AATCCCGCACGCCTCGAAAC
RFCP47GFP	CAGAAATTGGGTGACCCGACCACTCGGAAAACAGCCGCTCTGCCGGGCCCGGAGCTGCC
RRCP47GFP	GAATGAGCATCACCCAAACCGCTCTAACCATTCACAACCATTCCGGGGATCCGTCGACC
FCP47seg	GCGTGGCTGGTTCACCTTTG
RCP47seg	GCTGTAGGCCAGTTGTAGCG
Cytochrome b_6f GFP, YFP, CFP generation Subunit: PetA	
FpetA	GTTTGGGCAACTCTATCTGG
RpetA	CCTGCACTAAAGCTCACTAC
RFpetAGFP	AAACAAGTCGAGAAAGTGCAAGCTGCTGAGCTGAACTTCCTGCCGGGCCCGGAGCTGCC
RRpetAGFP	GGCCCGCCCTCTCTCTTGCAACCGTTACTGCAACCAGATATTCCGGGGATCCGTCGACC
FpetCseg	CGCTGACCAACGATCCGAAC
RpetCseg	GAGGCCATACCAACGGATGC
ATPase GFP, YFP, CFP generation Subunit: AtpB (sub β, 7942_2315)	
FatpB	GAAGCGGCTTGACGAATCAG
RatpB	TCTCCACCGATGAGTCCTAC
RFatpBGFP	GAAGCCATCGAAAAAGGCGCCAAGCTGAAAGCTGAATCCCTGCCGGGCCCGGAGCTGCC
RRatpBGFP	GCGGGGCTGCGATCGCAACCCCACCAAAGTCAGCCAAACATTCCGGGGATCCGTCGACC
FatpBseg	CCTTCTTCGTGGCTGAAGTG
RatpBseg	TGACCCGGCAAGATACCGAG
Cytochrome c GFP, YFP, CFP generation Subunit: CtaE	
ctaE F	TCCAGCCTAGCGATTACCTTCCTGA
ctaE R	ACACACAATCTGTCTTAGAGGCTGC
ctaE GFP F	ATCGTCTGGATTGTTTTATTTGTATTGCTTTACTTGATTCTGCCGGGCCCGGAGCTGCC

ctaE GFP R	TCTAGTTCTCTAGTTCTCTAAGATGGGTAATCACTAAACATTCCGGGGATCCGTCGACC
ctaE seg F	CAGAGATAACTTGTTTGCCAGCACT
ctaE seg R	TATTAAGCCAGAGCTCGCACTGCTC
Curt1 GFP, Knockdown, expression synpcc7942_1832	
F 1832	GCGGCAACTTCCTGCATCGA
R 1832	AAGTACAGGCTGCACCGGGG
F 1832 GFP cassette	CGTTTCAACGCCCTCAAAAAACAAGTACTGGGTGAGCGCCTGCCGGGCCCGGAGCTGCC
R 1832 GFP cassette	GGCTGGTTAGCCCCCCAGACAGCGATGACGCCAGAAAAAATTCCGGGGATCCGTCGACC
F 1832 GFP segregation	AACGAAGTTCCGCTGCTCGA
R 1832 GFP segregation	AAGCTCTGCGGACGGTCTTG
F 1832 KO	TGAGTTGCTGGTTTTGTGTCATCCCCCGTACTCGCTATGATTCCGGGGATCCGTCGACC
R 1832 KO	TGGTTAGCCCCCCAGACAGCGATGACGCCAGAAAAATTATGTAGGCTGGAGCTGCTTC
F 1832 KO segregation	AACCTCCCAAAGCGAAGACG
R 1832 KO segregation	AAGCTCTGCGGACGGTCTTG
Curt1 EcoRI F	ACCATCATCACCACAGCCAGATGACTTCCGAATCCAACCT
Curt1 HindIII R	TTAAGCATTATGCGGCCGCATTAGCGCTCACCCAGTACTT

References

ABRAHAMS, J. P., LESLIE, A. G., LUTTER, R. & WALKER, J. E. 1994. Structure at 2.8 A resolution of F1-ATPase from bovine heart mitochondria. *Nature,* 370**,** 621-628.

AGARWAL, R., MATROS, A., MELZER, M., MOCK, H.-P. & SAINIS, J. K. 2010. Heterogeneity in thylakoid membrane proteome of Synechocystis 6803. *Journal of proteomics,* 73**,** 976-991.

ALBERTSSON, P.-Å. 2001. A quantitative model of the domain structure of the photosynthetic membrane. *Trends in plant science,* 6**,** 349-354.

ALLEN, J. F. & FORSBERG, J. 2001. Molecular recognition in thylakoid structure and function. *Trends in plant science,* 6**,** 317-326.

ANDRIZHIYEVSKAYA, E. G., SCHWABE, T. M., GERMANO, M., D'HAENE, S., KRUIP, J., VAN GRONDELLE, R. & DEKKER, J. P. 2002. Spectroscopic properties of PSI–IsiA supercomplexes from the cyanobacterium Synechococcus PCC 7942. *Biochimica et Biophysica Acta (BBA)-Bioenergetics,* 1556**,** 265-272.

ARMBRUSTER, U., PRIBIL, M., VIOLA, S., XU, W., SCHARFENBERG, M., HERTLE, A. P., ROJAHN, U., JENSEN, P. E., RAPPAPORT, F. & JOLIOT, P. 2013. Arabidopsis CURVATURE THYLAKOID1 proteins modify thylakoid architecture by inducing membrane curvature. *The Plant Cell,* 25**,** 2661-2678.

ATAMNA-ISMAEEL, N., FINKEL, O., GLASER, F., VON MERING, C., VORHOLT, J. A., KOBLÍŽEK, M., BELKIN, S. & BÉJÀ, O. 2012. Bacterial anoxygenic photosynthesis on plant leaf surfaces. *Environmental microbiology reports,* 4**,** 209-216.

BALZANI, V., CREDI, A. & VENTURI, M. 2008. Photochemical conversion of solar energy. *ChemSusChem: Chemistry & Sustainability Energy & Materials,* 1**,** 26-58.

BANTSCHEFF, M., SCHIRLE, M., SWEETMAN, G., RICK, J. & KUSTER, B. 2007. Quantitative mass spectrometry in proteomics: a critical review. *Analytical and bioanalytical chemistry,* 389**,** 1017-1031.

BARBER, J. 2006. Photosystem II: an enzyme of global significance. *Biochemical Society Transactions,* 34**,** 619-631.

BAROLI, I. & NIYOGI, K. K. 2000. Molecular genetics of xanthophyll–dependent photoprotection in green algae and plants. *Philosophical Transactions of the Royal Society of London. Series B: Biological Sciences,* 355**,** 1385-1394.

BASAK, N. & DAS, D. 2007. The prospect of purple non-sulfur (PNS) photosynthetic bacteria for hydrogen production: the present state of the art. *World Journal of Microbiology and Biotechnology,* 23**,** 31-42.

BEČKOVÁ, M., GARDIAN, Z., YU, J., KONIK, P., NIXON, P. J. & KOMENDA, J. 2017. Association of Psb28 and Psb27 proteins with PSII-PSI supercomplexes upon exposure of Synechocystis sp. PCC 6803 to high light. *Molecular plant,* 10**,** 62-72.

BIBBY, T. S., NIELD, J. & BARBER, J. 2001. Iron deficiency induces the formation of an antenna ring around trimeric photosystem I in cyanobacteria. *Nature,* 412**,** 743-745.

BISWAS, S. & EATON-RYE, J. J. 2018. PsbY is required for prevention of photodamage to photosystem II in a PsbM-lacking mutant of *Synechocystis* sp. PCC 6803. *Photosynthetica,* 56**,** 200-209.

BOEKEMA, E., HIFNEY, A., YAKUSHEVSKA, A., PIOTROWSKI, M., KEEGSTRA, W., BERRY, S., MICHEL, K.-P., PISTORIUS, E. & KRUIP, J. 2001. A giant chlorophyll–protein complex induced by iron deficiency in cyanobacteria. *Nature,* 412**,** 745-748.

BOOTH, P. J. & CURNOW, P. 2009. Folding scene investigation: membrane proteins. *Current opinion in structural biology,* 19**,** 8-13.

BRYANT, D. A., COSTAS, A. M. G., MARESCA, J. A., CHEW, A. G. M., KLATT, C. G., BATESON, M. M., TALLON, L. J., HOSTETLER, J., NELSON, W. C. & HEIDELBERG, J. F. 2007. Candidatus Chloracidobacterium thermophilum: an aerobic phototrophic acidobacterium. *Science,* 317**,** 523-526.

BUSSI, Y., SHIMONI, E., WEINER, A., KAPON, R., CHARUVI, D., NEVO, R., EFRATI, E. & REICH, Z. 2019. Fundamental helical geometry consolidates the plant photosynthetic membrane. *Proceedings of the National Academy of Sciences,* 116**,** 22366-22375.

CAMERON, J. C., WILSON, S. C., BERNSTEIN, S. L. & KERFELD, C. A. 2013. Biogenesis of a bacterial organelle: the carboxysome assembly pathway. *Cell,* 155**,** 1131-1140.

CAO, P., CAO, D., SI, L., SU, X., TIAN, L., CHANG, W., LIU, Z., ZHANG, X. & LI, M. 2020. Structural basis for energy and electron transfer of the photosystem I-IsiA-flavodoxin supercomplex. *Nat Plants,* 6**,** 167-176.

CARDONA, T., SHAO, S. & NIXON, P. J. 2018. Enhancing photosynthesis in plants: the light reactions. *Essays in biochemistry,* 62**,** 85-94.

CASELLA, S., HUANG, F., MASON, D., ZHAO, G. Y., JOHNSON, G. N., MULLINEAUX, C. W. & LIU, L. N. 2017. Dissecting the native architecture and dynamics of cyanobacterial photosynthetic machinery. *Mol Plant,* 10**,** 1434-1448.

CHEN, A. H., AFONSO, B., SILVER, P. A. & SAVAGE, D. F. 2012. Spatial and temporal organization of chromosome duplication and segregation in the cyanobacterium Synechococcus elongatus PCC 7942. *PloS one,* 7**,** e47837.

CHIDGEY, J. W., LINHARTOVÁ, M., KOMENDA, J., JACKSON, P. J., DICKMAN, M. J., CANNIFFE, D. P., KONÍK, P., PILNÝ, J., HUNTER, C. N. & SOBOTKA, R. 2014. A cyanobacterial chlorophyll synthase-HliD complex associates with the Ycf39 protein and the YidC/Alb3 insertase. *The Plant Cell,* 26**,** 1267-1279.

CODDINGTON, J. M., JOHNS, S. R., LESLIE, D. R., WILLING, R. I. & BISHOP, D. G. 1981. 13C Nuclear magnetic resonance studies of the composition and fluidity of several chloroplast monogalactosyldiacylglycerols. *Biochimica et Biophysica Acta (BBA)-Lipids and Lipid Metabolism,* 663**,** 653-660.

COLLINGS, A. F. & CRITCHLEY, C. 2007. *Artificial photosynthesis: from basic biology to industrial application*, John Wiley & Sons.

COMAI, L. 2005. The advantages and disadvantages of being polyploid. *Nature reviews genetics,* 6**,** 836-846.

CONSUMPTION, E. R. 2008. World Consumption of Primary Energy by Energy Type and Selected Country Groups. December.

COOKE, I. R. & DESERNO, M. 2006. Coupling between lipid shape and membrane curvature. *Biophysical journal,* 91**,** 487-495.

COTTON, C. A., DOUGLASS, J. S., DE CAUSMAECKER, S., BRINKERT, K., CARDONA, T., FANTUZZI, A., RUTHERFORD, A. W. & MURRAY, J. W. 2015. Photosynthetic constraints on fuel from microbes. *Frontiers in bioengineering and biotechnology,* 3**,** 36.

DEKKER, J. P. & BOEKEMA, E. J. 2005. Supramolecular organization of thylakoid membrane proteins in green plants. *Biochimica et Biophysica Acta (BBA)-Bioenergetics,* 1706**,** 12-39.

DERACINOIS, B., FLAHAUT, C., DUBAN-DEWEER, S. & KARAMANOS, Y. 2013. Comparative and quantitative global proteomics approaches: an overview. *Proteomes,* 1**,** 180-218.

DRIN, G. & ANTONNY, B. 2010. Amphipathic helices and membrane curvature. *FEBS letters,* 584**,** 1840-1847.

EISENBERG, D., SCHWARZ, E., KOMAROMY, M. & WALL, R. 1984. Analysis of membrane and surface protein sequences with the hydrophobic moment plot. *Journal of molecular biology,* 179**,** 125-142.

EISENBERG, R. & NOCERA, D. G. 2005. Preface: Overview of the forum on solar and renewable energy. *Inorganic chemistry,* 44**,** 6799-6801.

FALK, S., SAMSON, G., BRUCE, D., HUNER, N. P. & LAUDENBACH, D. E. 1995. Functional analysis of the iron-stress induced CP 43′ polypeptide of PS II in the cyanobacterium Synechococcus sp. PCC 7942. *Photosynthesis Research,* 45**,** 51-60.

FAULKNER, M., RODRIGUEZ-RAMOS, J., DYKES, G. F., OWEN, S. V., CASELLA, S., SIMPSON, D. M., BEYNON, R. J. & LIU, L.-N. 2017. Direct characterization of the native structure and mechanics of cyanobacterial carboxysomes. *Nanoscale,* 9**,** 10662-10673.

FERREIRA, K. N., IVERSON, T. M., MAGHLAOUI, K., BARBER, J. & IWATA, S. 2004. Architecture of the photosynthetic oxygen-evolving center. *Science,* 303**,** 1831-1838.

FOLEA, I. M., ZHANG, P., ARO, E.-M. & BOEKEMA, E. J. 2008. Domain organization of photosystem II in membranes of the cyanobacterium Synechocystis PCC6803 investigated by electron microscopy. *FEBS letters,* 582**,** 1749-1754.

FOUQUET, C., GILLES, J.-F., HECK, N., DOS SANTOS, M., SCHWARTZMANN, R., CANNAYA, V., MOREL, M.-P., DAVIDSON, R. S., TREMBLEAU, A. & BOLTE, S. 2015. Improving axial resolution in confocal microscopy with new high refractive index mounting media. *PloS one,* 10**,** e0121096.

FRAIN, K. M., GANGL, D., JONES, A., ZEDLER, J. A. & ROBINSON, C. 2016. Protein translocation and thylakoid biogenesis in cyanobacteria. *Biochimica et Biophysica Acta (BBA)-Bioenergetics,* 1857**,** 266-273.

FRANCK, F., JUNEAU, P. & POPOVIC, R. 2002. Resolution of the photosystem I and photosystem II contributions to chlorophyll fluorescence of intact leaves at room temperature. *Biochimica et Biophysica Acta (BBA)-Bioenergetics,* 1556**,** 239-246.

FROGER, A. & HALL, J. E. 2007. Transformation of plasmid DNA into E. coli using the heat shock method. *JoVE (Journal of Visualized Experiments)***,** e253.

GALE, J. 2009. *Astrobiology of Earth: the emergence, evolution and future of life on a planet in turmoil*, Oxford University Press.

GAO, F., ZHAO, J., CHEN, L., BATTCHIKOVA, N., RAN, Z., ARO, E. M., OGAWA, T. & MA, W. 2016. The NDH-1L-PSI supercomplex is important for efficient cyclic electron transport in cyanobacteria. *Plant Physiol,* 172**,** 1451-1464.

GOCLAW-BINDER, H., SENDERSKY, E., SHIMONI, E., KISS, V., REICH, Z., PERELMAN, A. & SCHWARZ, R. 2012. Nutrient-associated elongation and asymmetric division of the cyanobacterium Synechococcus PCC 7942. *Environmental microbiology,* 14**,** 680-690.

GOFF, S. A., RICKE, D., LAN, T.-H., PRESTING, G., WANG, R., DUNN, M., GLAZEBROOK, J., SESSIONS, A., OELLER, P. & VARMA, H. 2002. A draft sequence of the rice genome (Oryza sativa L. ssp. japonica). *Science,* 296**,** 92-100.

GORELOVA, O., BAULINA, O., RASMUSSEN, U. & KOKSHAROVA, O. 2013. The pleiotropic effects of ftn2 and ftn6 mutations in cyanobacterium Synechococcus sp. PCC 7942. *Protoplasma,* 250**,** 931-942.

GRENIER, F., MATTEAU, D., BABY, V. & RODRIGUE, S. 2014. Complete genome sequence of Escherichia coli BW25113. *Genome announcements,* 2**,** e01038-14.

GRIESE, M., LANGE, C. & SOPPA, J. 2011. Ploidy in cyanobacteria. *FEMS microbiology letters,* 323**,** 124-131.

GROTH, G. & POHL, E. 2001. The structure of the chloroplast F1-ATPase at 3.2 Å resolution. *Journal of Biological Chemistry,* 276**,** 1345-1352.

GUIKEMA, J. A. & SHERMAN, L. A. 1983. Organization and function of chlorophyll in membranes of cyanobacteria during iron starvation. *Plant Physiology,* 73**,** 250-256.

GUST, B., CHANDRA, G., JAKIMOWICZ, D., YUQING, T., BRUTON, C. J. & CHATER, K. F. 2004. λ Red-mediated genetic manipulation of antibiotic-producing Streptomyces. *Advances in applied microbiology,* 54**,** 107-128.

GUST, B., KIESER, T. & CHATER, K. 2002. REDIRECT technology: PCR-targeting system in Streptomyces coelicolor. *The John Innes Centre, Norwich, United Kingdom*.

HAHN, A., VONCK, J., MILLS, D. J., MEIER, T. & KUHLBRANDT, W. 2018. Structure, mechanism, and regulation of the chloroplast ATP synthase. *Science,* 360.

HANSSON, M. & VENER, A. V. 2003. Identification of three previously unknown in vivo protein phosphorylation sites in thylakoid membranes of Arabidopsis thaliana. *Molecular & Cellular Proteomics,* 2**,** 550-559.

HART, S., SCHLARB-RIDLEY, B., BENDALL, D. & HOWE, C. 2005. Terminal oxidases of cyanobacteria. *Biochemical Society Transactions,* 33**,** 832-835.

HASAN, S. S., YAMASHITA, E., BANIULIS, D. & CRAMER, W. A. 2013. Quinone-dependent proton transfer pathways in the photosynthetic cytochrome b6f complex. *Proceedings of the National Academy of Sciences,* 110**,** 4297-4302.

HAVAUX, M. & NIYOGI, K. K. 1999. The violaxanthin cycle protects plants from photooxidative damage by more than one mechanism. *Proceedings of the National Academy of Sciences,* 96**,** 8762-8767.

HEATHCOTE, P., FYFE, P. K. & JONES, M. R. 2002. Reaction centres: the structure and evolution of biological solar power. *Trends in biochemical sciences,* 27**,** 79-87.

HEIDORN, T., CAMSUND, D., HUANG, H.-H., LINDBERG, P., OLIVEIRA, P., STENSJÖ, K. & LINDBLAD, P. 2011. Synthetic biology in cyanobacteria: engineering and analyzing novel functions. *Methods in enzymology,* 497**,** 539-579.

HEINZ, S., LIAUW, P., NICKELSEN, J. & NOWACZYK, M. 2016a. Analysis of photosystem II biogenesis in cyanobacteria. *Biochimica Et Biophysica Acta (BBA)-Bioenergetics,* 1857**,** 274-287.

HEINZ, S., RAST, A., SHAO, L., GUTU, A., GÜGEL, I. L., HEYNO, E., RENGSTL, B., VIOLA, S., NOWACZYK, M. M. & LEISTER, D. 2016b. Thylakoid Membrane Architecture in Synechocystis Depends on CurT, a Homolog of the Granal CURVATURE THYLAKOID1 Proteins. *The Plant Cell Online***,** tpc. 00491.2016.

HELLMICH, J., BOMMER, M., BURKHARDT, A., IBRAHIM, M., KERN, J., MEENTS, A., MÜH, F., DOBBEK, H. & ZOUNI, A. 2014. Native-like photosystem II superstructure at 2.44 Å resolution through detergent extraction from the protein crystal. *Structure,* 22**,** 1607-1615.

HOHMANN-MARRIOTT, M. F. & BLANKENSHIP, R. E. 2011. Evolution of photosynthesis. *Annual review of plant biology,* 62**,** 515-548.

HOLTMAN, C. K., CHEN, Y., SANDOVAL, P., GONZALES, A., NALTY, M. S., THOMAS, T. L., YOUDERIAN, P. & GOLDEN, S. S. 2005. High-throughput functional analysis of the Synechococcus elongatus PCC 7942 genome. *DNA research,* 12**,** 103-115.

HUANG, F., KONG, W., SUN, Y., CHEN, T., DYKES, G. F., JIANG, Y. L. & LIU, L. N. 2020. Rubisco accumulation factor 1 (Raf1) plays essential roles in mediating Rubisco assembly and carboxysome biogenesis. *Proc Natl Acad Sci USA,* 117**,** 17418-17428.

HUANG, F., VASIEVA, O., SUN, Y., FAULKNER, M., DYKES, G. F., ZHAO, Z. & LIU, L. N. 2019. Roles of RbcX in carboxysome biosynthesis in the cyanobacterium *Synechococcus elongatus* PCC7942. *Plant Physiol,* 179**,** 184-194.

HUOKKO, T., NI, T., DYKES, G. F., SIMPSON, D. M., BROWNRIDGE, P., CONRADI, F. D., BEYNON, R. J., NIXON, P. J., MULLINEAUX, C. W. & ZHANG, P. 2021. Probing the biogenesis pathway and dynamics of thylakoid membranes. *Nature Communications,* 12**,** 1-14.

ISHIHAMA, Y., ODA, Y., TABATA, T., SATO, T., NAGASU, T., RAPPSILBER, J. & MANN, M. 2005. Exponentially modified protein abundance index (emPAI) for estimation of absolute protein amount in proteomics by the number of sequenced peptides per protein. *Molecular & Cellular Proteomics,* 4**,** 1265-1272.

IVANOV, A. G., KROL, M., SVESHNIKOV, D., SELSTAM, E., SANDSTRÖM, S., KOOCHEK, M., PARK, Y.-I., VASIL'EV, S., BRUCE, D. & ÖQUIST, G. 2006. Iron deficiency in cyanobacteria causes monomerization of photosystem I trimers and reduces the capacity for state transitions and the effective absorption cross section of photosystem I in vivo. *Plant physiology,* 141**,** 1436-1445.

IVLEVA, N. B., BRAMLETT, M. R., LINDAHL, P. A. & GOLDEN, S. S. 2005. LdpA: a component of the circadian clock senses redox state of the cell. *The EMBO journal,* 24**,** 1202-1210.

IWAI, M., TAKIZAWA, K., TOKUTSU, R., OKAMURO, A., TAKAHASHI, Y. & MINAGAWA, J. 2010. Isolation of the elusive supercomplex that drives cyclic electron flow in photosynthesis. *Nature,* 464**,** 1210-1213.

JAIN, I. H., VIJAYAN, V. & O'SHEA, E. K. 2012. Spatial ordering of chromosomes enhances the fidelity of chromosome partitioning in cyanobacteria. *Proceedings of the National Academy of Sciences,* 109**,** 13638-13643.

JAKUBAUSKAS, D., KOWALEWSKA, Ł., SOKOLOVA, A. V., GARVEY, C. J., MORTENSEN, K., JENSEN, P. E. & KIRKENSGAARD, J. J. 2019. Ultrastructural modeling of small angle scattering from photosynthetic membranes. *Scientific reports,* 9**,** 1-13.

JALEEL, C. A., MANIVANNAN, P., WAHID, A., FAROOQ, M., AL-JUBURI, H. J., SOMASUNDARAM, R. & PANNEERSELVAM, R. 2009. Drought stress in plants: a review on morphological characteristics and pigments composition. *Int. J. Agric. Biol,* 11**,** 100-105.

JENSEN, P. E., GILPIN, M., KNOETZEL, J. & SCHELLER, H. V. 2000. The PSI-K subunit of photosystem I is involved in the interaction between light-harvesting complex I and the photosystem I reaction center core. *Journal of Biological Chemistry,* 275**,** 24701-24708.

JENSEN, P. E. & LEISTER, D. 2014. Cyanobacteria as an experimental platform for modifying bacterial and plant photosynthesis. *Frontiers in bioengineering and biotechnology,* 2**,** 7.

JORDAN, P., FROMME, P., WITT, H. T., KLUKAS, O., SAENGER, W. & KRAUß, N. 2001. Three-dimensional structure of cyanobacterial photosystem I at 2.5 Å resolution. *Nature,* 411**,** 909-917.

JOSHUA, S. & MULLINEAUX, C. W. 2004. Phycobilisome diffusion is required for light-state transitions in cyanobacteria. *Plant physiology,* 135**,** 2112-2119.

KAMAT, P. V. 2007. Meeting the clean energy demand: nanostructure architectures for solar energy conversion. *The Journal of Physical Chemistry C,* 111**,** 2834-2860.

KAMIYA, N. & SHEN, J.-R. 2003. Crystal structure of oxygen-evolving photosystem II from Thermosynechococcus vulcanus at 3.7-Å resolution. *Proceedings of the National Academy of Sciences,* 100**,** 98-103.

KERN, J., ZOUNI, A., GUSKOV, A. & KRAUß, N. 2009. Lipids in the Structure of Photosystem I, Photosystem II and the Cytochrome b 6 f Complex. *Lipids in photosynthesis.* Springer.

KHANNA, R., GRAHAM, J.-R., MYERS, J. & GANTT, E. 1983. Phycobilisome composition and possible relationship to reaction centers. *Archives of biochemistry and biophysics,* 224**,** 534-542.

KHROUCHTCHOVA, A., HANSSON, M., PAAKKARINEN, V., VAINONEN, J. P., ZHANG, S., JENSEN, P. E., SCHELLER, H. V., VENER, A. V., ARO, E.-M. & HALDRUP, A. 2005. A previously found thylakoid membrane protein of 14 kDa

(TMP14) is a novel subunit of plant photosystem I and is designated PSI-P. *FEBS letters,* 579**,** 4808-4812.

KIMPLE, M. E., BRILL, A. L. & PASKER, R. L. 2013. Overview of affinity tags for protein purification. *Current protocols in protein science,* 73**,** 9.9. 1-9.9. 23.

KIRCHHOFF, H., BORINSKI, M., LENHERT, S., CHI, L. & BÜCHEL, C. 2004. Transversal and lateral exciton energy transfer in grana thylakoids of spinach. *Biochemistry,* 43**,** 14508-14516.

KIRST, H., GABILLY, S. T., NIYOGI, K. K., LEMAUX, P. G. & MELIS, A. 2017. Photosynthetic antenna engineering to improve crop yields. *Planta,* 245**,** 1009-1020.

KITAJIMA, M. & BUTLER, W. 1975. Quenching of chlorophyll fluorescence and primary photochemistry in chloroplasts by dibromothymoquinone. *Biochimica et Biophysica Acta (BBA)-Bioenergetics,* 376**,** 105-115.

KNOPPOVÁ, J., SOBOTKA, R., TICHÝ, M., YU, J., KONIK, P., HALADA, P., NIXON, P. J. & KOMENDA, J. 2014. Discovery of a chlorophyll binding protein complex involved in the early steps of photosystem II assembly in Synechocystis. *The Plant Cell,* 26**,** 1200-1212.

KOLLMITZER, B., HEFTBERGER, P., RAPPOLT, M. & PABST, G. 2013. Monolayer spontaneous curvature of raft-forming membrane lipids. *Soft matter,* 9**,** 10877-10884.

KOMENDA, J., BARKER, M., KUVIKOVÁ, S., DE VRIES, R., MULLINEAUX, C. W., TICHÝ, M. & NIXON, P. J. 2006. The FtsH protease slr0228 is important for quality control of photosystem II in the thylakoid membrane of Synechocystis sp. PCC 6803. *Journal of Biological Chemistry,* 281**,** 1145-1151.

KOUŘIL, R., ARTENI, A. A., LAX, J., YEREMENKO, N., RÖGNER, M., MATTHIJS, H. C., DEKKER, J. P. & BOEKEMA, E. J. 2005. Structure and functional role of supercomplexes of IsiA and Photosystem I in cyanobacterial photosynthesis. *FEBS letters,* 579**,** 3253-3257.

KOUŘIL, R., STROUHAL, O., NOSEK, L., LENOBEL, R., CHAMRÁD, I., BOEKEMA, E. J., ŠEBELA, M. & ILÍK, P. 2014. Structural characterization of a plant photosystem I and NAD (P) H dehydrogenase supercomplex. *The Plant Journal,* 77**,** 568-576.

KUNKEL, D. D. 1982. Thylakoid centers: structures associated with the cyanobacterial photosynthetic membrane system. *Archives of Microbiology,* 133**,** 97-99.

KURISU, G., ZHANG, H., SMITH, J. L. & CRAMER, W. A. 2003. Structure of the cytochrome b6f complex of oxygenic photosynthesis: tuning the cavity. *Science,* 302**,** 1009-1014.

LAPUENTE-BRUN, E., MORENO-LOSHUERTOS, R., ACIN-PEREZ, R., LATORRE-PELLICER, A., COLAS, C., BALSA, E., PERALES-CLEMENTE, E., QUIROS, P. M., CALVO, E., RODRIGUEZ-HERNANDEZ, M. A., NAVAS, P., CRUZ, R., CARRACEDO, A., LOPEZ-OTIN, C., PEREZ-MARTOS, A., FERNANDEZ-SILVA, P., FERNANDEZ-VIZARRA, E. & ENRIQUEZ, J. A. 2013. Supercomplex assembly determines electron flux in the mitochondrial electron transport chain. *Science,* 340**,** 1567-70.

LASARRE, B., KYSELA, D. T., STEIN, B. D., DUCRET, A., BRUN, Y. V. & MCKINLAY, J. B. 2018. Restricted localization of photosynthetic intracytoplasmic membranes (ICMs) in multiple genera of purple nonsulfur bacteria. *Mbio,* 9.

LAUGHLIN, T. G., BAYNE, A. N., TREMPE, J.-F., SAVAGE, D. F. & DAVIES, K. M. 2019. Structure of the complex I-like molecule NDH of oxygenic photosynthesis. *Nature,* 566**,** 411-414.

LEA-SMITH, D. J., BOMBELLI, P., VASUDEVAN, R. & HOWE, C. J. 2016. Photosynthetic, respiratory and extracellular electron transport pathways in cyanobacteria. *Biochimica et Biophysica Acta (BBA)-Bioenergetics,* 1857**,** 247-255.

LIBERTON, M., PAGE, L. E., O'DELL, W. B., O'NEILL, H., MAMONTOV, E., URBAN, V. S. & PAKRASI, H. B. 2013. Organization and flexibility of cyanobacterial thylakoid membranes examined by neutron scattering. *Journal of Biological Chemistry,* 288**,** 3632-3640.

LIU, H., ZHANG, H., NIEDZWIEDZKI, D. M., PRADO, M., HE, G., GROSS, M. L. & BLANKENSHIP, R. E. 2013. Phycobilisomes supply excitations to both photosystems in a megacomplex in cyanobacteria. *Science,* 342**,** 1104-1107.

LIU, L.-N. 2016. Distribution and dynamics of electron transport complexes in cyanobacterial thylakoid membranes. *Biochimica et Biophysica Acta (BBA)-Bioenergetics,* 1857**,** 256-265.

LIU, L.-N., AARTSMA, T. J., THOMAS, J.-C., ZHOU, B.-C. & ZHANG, Y.-Z. 2009a. FRAP analysis on red alga reveals the fluorescence recovery is ascribed to intrinsic photoprocesses of phycobilisomes than large-scale diffusion. *PLoS One,* 4.

LIU, L.-N., BRYAN, S. J., HUANG, F., YU, J., NIXON, P. J., RICH, P. R. & MULLINEAUX, C. W. 2012. Control of electron transport routes through redox-regulated redistribution of respiratory complexes. *Proceedings of the National Academy of Sciences,* 109**,** 11431-11436.

LIU, L.-N., DUQUESNE, K., STURGIS, J. N. & SCHEURING, S. 2009b. Quinone pathways in entire photosynthetic chromatophores of Rhodospirillum photometricum. *Journal of molecular biology,* 393**,** 27-35.

LIU, L.-N. & SCHEURING, S. 2013. Investigation of photosynthetic membrane structure using atomic force microscopy. *Trends in plant science,* 18**,** 277-286.

LIU, L. N., DUQUESNE, K., OESTERHELT, F., STURGIS, J. N. & SCHEURING, S. 2011a. Forces guiding assembly of light-harvesting complex 2 in native membranes. *Proc Natl Acad Sci U S A,* 108**,** 9455-9.

LIU, L. N., STURGIS, J. N. & SCHEURING, S. 2011b. Native architecture of the photosynthetic membrane from *Rhodobacter veldkampii*. *J Struct Biol,* 173**,** 138-45.

LOBLEY, A., WHITMORE, L. & WALLACE, B. 2002. DICHROWEB: an interactive website for the analysis of protein secondary structure from circular dichroism spectra. *Bioinformatics,* 18**,** 211-212.

LONG, S., HUMPHRIES, S. & FALKOWSKI, P. G. 1994. Photoinhibition of photosynthesis in nature. *Annual review of plant biology,* 45**,** 633-662.

LONG, S. P., ZHU, X. G., NAIDU, S. L. & ORT, D. R. 2006. Can improvement in photosynthesis increase crop yields? *Plant, cell & environment,* 29**,** 315-330.

MACGREGOR-CHATWIN, C., JACKSON, P., SENER, M., CHIDGEY, J., HITCHCOCK, A., QIAN, P., MAYNEORD, G., JOHNSON, M., LUTHEY-SCHULTEN, Z. & DICKMAN, M. 2019. Membrane organization of photosystem I complexes in the most abundant phototroph on Earth. *Nature plants,* 5**,** 879-889.

MACGREGOR-CHATWIN, C., SENER, M., BARNETT, S. F., HITCHCOCK, A., BARNHART-DAILEY, M. C., MAGHLAOUI, K., BARBER, J., TIMLIN, J. A., SCHULTEN, K. & HUNTER, C. N. 2017. Lateral segregation of photosystem I in cyanobacterial thylakoids. *The Plant Cell,* 29**,** 1119-1136.

MAREŠ, J., STRUNECKÝ, O., BUČINSKÁ, L. & WIEDERMANNOVÁ, J. 2019. Evolutionary patterns of thylakoid architecture in cyanobacteria. *Frontiers in microbiology,* 10**,** 277.

MAXWELL, K. & JOHNSON, G. N. 2000. Chlorophyll fluorescence—a practical guide. *Journal of experimental botany,* 51**,** 659-668.

MCCONNELL, M. D., KOOP, R., VASIL'EV, S. & BRUCE, D. 2002. Regulation of the distribution of chlorophyll and phycobilin-absorbed excitation energy in cyanobacteria. A structure-based model for the light state transition. *Plant physiology,* 130**,** 1201-1212.

MCCREE, K. 1981. Physiological Plant Ecology I: Responses to the Physical Environment. *OL Lange, PS Nobel, CB Osmond, & H. Ziegler (Eds.)*, 41-55.

MCMAHON, H. T. & BOUCROT, E. 2015. Membrane curvature at a glance. *Journal of cell science,* 128**,** 1065-1070.

MCMAHON, H. T. & GALLOP, J. L. 2005. Membrane curvature and mechanisms of dynamic cell membrane remodelling. *Nature,* 438**,** 590-596.

MELARAGNO, J. E., MEHROTRA, B. & COLEMAN, A. W. 1993. Relationship between endopolyploidy and cell size in epidermal tissue of Arabidopsis. *The Plant Cell,* 5**,** 1661-1668.

MILES, A. J. & WALLACE, B. A. 2016. Circular dichroism spectroscopy of membrane proteins. *Chemical society reviews,* 45**,** 4859-4872.

MILLER, L. C., ZHAO, L., CANNIFFE, D. P., MARTIN, D. & LIU, L. N. 2020a. Unfolding pathway and intermolecular interactions of the cytochrome subunit in the bacterial photosynthetic reaction center. *Biochim Biophys Acta - Bioenergetics,* 1861**,** 148204.

MILLER, T. E., BENEYTON, T., SCHWANDER, T., DIEHL, C., GIRAULT, M., MCLEAN, R., CHOTEL, T., CLAUS, P., CORTINA, N. S. & BARET, J.-C. 2020b. Light-powered CO2 fixation in a chloroplast mimic with natural and synthetic parts. *Science,* 368**,** 649-654.

MONTEITH, J. L. 1977. Climate and the efficiency of crop production in Britain. *Philosophical Transactions of the Royal Society of London. B, Biological Sciences,* 281**,** 277-294.

MORI, T., BINDER, B. & JOHNSON, C. H. 1996. Circadian gating of cell division in cyanobacteria growing with average doubling times of less than 24 hours. *Proceedings of the National Academy of Sciences,* 93**,** 10183-10188.

MÜLLER, D. J., FOTIADIS, D., SCHEURING, S., MÜLLER, S. A. & ENGEL, A. 1999. Electrostatically balanced subnanometer imaging of biological specimens by atomic force microscopy. *Biophys. J,* 76**,** 1101-1111.

MULLINEAUX, C. W. 1999. The thylakoid membranes of cyanobacteria: structure, dynamics and function. *Functional Plant Biology,* 26**,** 671-677.

MULLINEAUX, C. W. 2005. Function and evolution of grana. *Trends in plant science,* 10**,** 521-525.

MULLINEAUX, C. W. & LIU, L.-N. 2020. Membrane dynamics in phototrophic bacteria. *Annual review of microbiology,* 74**,** 633-654.

MULLINEAUX, C. W., TOBIN, M. J. & JONES, G. R. 1997. Mobility of photosynthetic complexes in thylakoid membranes. *Nature,* 390**,** 421-424.

MURPHY, D. J. 1982. The importance of non-planar bilayer regions in photosynthetic membranes and their stabilisation by galactolipids. *Febs Letters,* 150**,** 19-26.

NELLAEPALLI, S., OZAWA, S.-I., KURODA, H. & TAKAHASHI, Y. 2018. The photosystem I assembly apparatus consisting of Ycf3–Y3IP1 and Ycf4 modules. *Nature communications,* 9**,** 1-10.

NEUMÜLLER, R. A., WIRTZ-PEITZ, F., LEE, S., KWON, Y., BUCKNER, M., HOSKINS, R. A., VENKEN, K. J., BELLEN, H. J., MOHR, S. E. & PERRIMON, N. 2012. Stringent analysis of gene function and protein–protein interactions using fluorescently tagged genes. *Genetics,* 190**,** 931-940.

NEVO, R., CHARUVI, D., SHIMONI, E., SCHWARZ, R., KAPLAN, A., OHAD, I. & REICH, Z. 2007. Thylakoid membrane perforations and connectivity enable intracellular traffic in cyanobacteria. *The EMBO journal,* 26**,** 1467-1473.

NICKELSEN, J., RENGSTL, B., STENGEL, A., SCHOTTKOWSKI, M., SOLL, J. & ANKELE, E. 2011. Biogenesis of the cyanobacterial thylakoid membrane system–an update. *FEMS microbiology letters,* 315**,** 1-5.

NIJTMANS, L. G., DE JONG, L., SANZ, M. A., COATES, P. J., BERDEN, J. A., BACK, J. W., MUIJSERS, A. O., VAN DER SPEK, H. & GRIVELL, L. A. 2000. Prohibitins act as a membrane-bound chaperone for the stabilization of mitochondrial proteins. *The EMBO journal,* 19**,** 2444-2451.

ÖQUIST, G. 1974. Iron deficiency in the blue-green alga Anacystis nidulans: Fluorescence and absorption spectra recorded at 77° K. *Physiologia Plantarum,* 31**,** 55-58.

OSSENBÜHL, F., INABA-SULPICE, M., MEURER, J., SOLL, J. & EICHACKER, L. A. 2006. The Synechocystis sp PCC 6803 oxa1 homolog is essential for membrane integration of reaction center precursor protein pD1. *The Plant Cell,* 18**,** 2236-2246.

PALLEROS, D. R., REID, K. L., SHI, L. & FINK, A. L. 1993. DnaK ATPase activity revisited. *FEBS letters,* 336**,** 124-128.

PALMER, J. D. 2003. The symbiotic birth and spread of plastids: how many times and whodunit? *Journal of Phycology,* 39**,** 4-12.

PAN, X., CAO, D., XIE, F., XU, F., SU, X., MI, H., ZHANG, X. & LI, M. 2020. Structural basis for electron transport mechanism of complex I-like photosynthetic NAD (P) H dehydrogenase. *Nature communications,* 11**,** 1-11.

PENG, L., FUKAO, Y., FUJIWARA, M., TAKAMI, T. & SHIKANAI, T. 2009. Efficient operation of NAD(P)H dehydrogenase requires supercomplex formation with photosystem I via minor LHCI in Arabidopsis. *Plant Cell,* 21**,** 3623-40.

PENG, L., SHIMIZU, H. & SHIKANAI, T. 2008. The chloroplast NAD(P)H dehydrogenase complex interacts with photosystem I in Arabidopsis. *J Biol Chem,* 283**,** 34873-9.

PERKINS, D. N., PAPPIN, D. J., CREASY, D. M. & COTTRELL, J. S. 1999. Probability-based protein identification by searching sequence databases using mass spectrometry data. *ELECTROPHORESIS: An International Journal,* 20**,** 3551-3567.

PROVENCHER, S. W. & GLOECKNER, J. 1981. Estimation of globular protein secondary structure from circular dichroism. *Biochemistry,* 20**,** 33-37.

QIAN, P., PAPIZ, M. Z., JACKSON, P. J., BRINDLEY, A. A., NG, I. W., OLSEN, J. D., DICKMAN, M. J., BULLOUGH, P. A. & HUNTER, C. N. 2013. Three-dimensional structure of the Rhodobacter sphaeroides RC-LH1-PufX complex: dimerization and quinone channels promoted by PufX. *Biochemistry,* 52**,** 7575-7585.

RAPPSILBER, J., RYDER, U., LAMOND, A. I. & MANN, M. 2002. Large-scale proteomic analysis of the human spliceosome. *Genome research,* 12**,** 1231-1245.

RAST, A., SCHAFFER, M., ALBERT, S., WAN, W., PFEFFER, S., BECK, F., PLITZKO, J. M., NICKELSEN, J. & ENGEL, B. D. 2019. Biogenic regions of cyanobacterial thylakoids form contact sites with the plasma membrane. *Nature plants,* 5**,** 436-446.

RENSING, S. A., LANG, D., ZIMMER, A. D., TERRY, A., SALAMOV, A., SHAPIRO, H., NISHIYAMA, T., PERROUD, P.-F., LINDQUIST, E. A. & KAMISUGI, Y. 2008. The Physcomitrella genome reveals evolutionary insights into the conquest of land by plants. *Science,* 319**,** 64-69.

RESKI, R. 1998. Physcomitrella and Arabidopsis: the David and Goliath of reverse genetics. *Trends in Plant Science,* 6**,** 209-210.

REXROTH, S., MULLINEAUX, C. W., ELLINGER, D., SENDTKO, E., RÖGNER, M. & KOENIG, F. 2011. The plasma membrane of the cyanobacterium Gloeobacter violaceus contains segregated bioenergetic domains. *The Plant Cell,* 23**,** 2379-2390.

RIPPKA, R., DERUELLES, J., WATERBURY, J. B., HERDMAN, M. & STANIER, R. Y. 1979. Generic assignments, strain histories and properties of pure cultures of cyanobacteria. *Microbiology,* 111**,** 1-61.

RITCHIE, R. J. 2006. Consistent sets of spectrophotometric chlorophyll equations for acetone, methanol and ethanol solvents. *Photosynthesis research,* 89**,** 27-41.

ROY, A., KUCUKURAL, A. & ZHANG, Y. 2010. I-TASSER: a unified platform for automated protein structure and function prediction. *Nature protocols,* 5**,** 725-738.

RUBIN, B. E., WETMORE, K. M., PRICE, M. N., DIAMOND, S., SHULTZABERGER, R. K., LOWE, L. C., CURTIN, G., ARKIN, A. P., DEUTSCHBAUER, A. & GOLDEN, S. S. 2015. The essential gene set of a photosynthetic organism. *Proceedings of the National Academy of Sciences,* 112**,** E6634-E6643.

RUMBAUGH, G. & MILLER, C. A. 2010. Epigenetic changes in the brain: measuring global histone modifications. *Alzheimer's Disease and Frontotemporal Dementia.* Springer.

SACHELARU, I., PETRIMAN, N. A., KUDVA, R., KUHN, P., WELTE, T., KNAPP, B., DREPPER, F., WARSCHEID, B. & KOCH, H.-G. 2013. YidC occupies the lateral gate of the SecYEG translocon and is sequentially displaced by a nascent membrane protein. *Journal of Biological Chemistry,* 288**,** 16295-16307.

SALOMON, E. & KEREN, N. 2011. Manganese limitation induces changes in the activity and in the organization of photosynthetic complexes in the cyanobacterium Synechocystis sp. strain PCC 6803. *Plant physiology,* 155**,** 571-579.

SCHAECHTER, M. 2009. *Encyclopedia of microbiology*, Academic Press.

SCHNEIDER, C. A., RASBAND, W. S. & ELICEIRI, K. W. 2012. NIH Image to ImageJ: 25 years of image analysis. *Nat Methods,* 9**,** 671-5.

SCHNEIDER, D., BERRY, S., RICH, P., SEIDLER, A. & RÖGNER, M. 2001. A regulatory role of the PetM subunit in a cyanobacterial cytochrome b 6 f complex. *Journal of Biological Chemistry,* 276**,** 16780-16785.

SCHNEIDER, D., VOLKMER, T. & RÖGNER, M. 2007. PetG and PetN, but not PetL, are essential subunits of the cytochrome b 6 f complex from Synechocystis PCC 6803. *Research in microbiology,* 158**,** 45-50.

SCHOTTKOWSKI, M., GKALYMPOUDIS, S., TZEKOVA, N., STELLJES, C., SCHÜNEMANN, D., ANKELE, E. & NICKELSEN, J. 2009. Interaction of the periplasmic PratA factor and the PsbA (D1) protein during biogenesis of photosystem II in Synechocystis sp. PCC 6803. *Journal of Biological Chemistry,* 284**,** 1813-1819.

SCHULLER, J. M., BIRRELL, J. A., TANAKA, H., KONUMA, T., WULFHORST, H., COX, N., SCHULLER, S. K., THIEMANN, J., LUBITZ, W. & SÉTIF, P. 2019. Structural adaptations of photosynthetic complex I enable ferredoxin-dependent electron transfer. *Science,* 363**,** 257-260.

SCHULLER, J. M., SAURA, P., THIEMANN, J., SCHULLER, S. K., GAMIZ-HERNANDEZ, A. P., KURISU, G., NOWACZYK, M. M. & KAILA, V. R. 2020. Redox-coupled proton pumping drives carbon concentration in the photosynthetic complex I. *Nature Communications,* 11**,** 1-7.

SCHWILLE, P., SPATZ, J., LANDFESTER, K., BODENSCHATZ, E., HERMINGHAUS, S., SOURJIK, V., ERB, T. J., BASTIAENS, P., LIPOWSKY, R. & HYMAN, A. 2018. MaxSynBio: avenues towards creating cells from the bottom up. *Angewandte Chemie International Edition,* 57**,** 13382-13392.

SEIWERT, D., WITT, H., RITZ, S., JANSHOFF, A. & PAULSEN, H. 2018. The nonbilayer lipid MGDG and the major light-harvesting complex (LHCII) promote membrane stacking in supported lipid bilayers. *Biochemistry,* 57**,** 2278-2288.

ŞENER, M. K., OLSEN, J. D., HUNTER, C. N. & SCHULTEN, K. 2007. Atomic-level structural and functional model of a bacterial photosynthetic membrane vesicle. *Proceedings of the National Academy of Sciences,* 104**,** 15723-15728.

SHARKEY, T. D. 1988. Estimating the rate of photorespiration in leaves. *Physiologia Plantarum,* 73**,** 147-152.

SHEN, J.-R., QIAN, M., INOUE, Y. & BURNAP, R. L. 1998. Functional Characterization of *Synechocystis* sp. PCC 6803 Δ*psbU* and Δ*psbV* Mutants

Reveals Important Roles of Cytochrome c-550 in Cyanobacterial Oxygen Evolution. *Biochemistry,* 37**,** 1551-1558.

SHERMAN, D. M., TROYAN, T. A. & SHERMAN, L. A. 1994. Localization of membrane proteins in the cyanobacterium Synechococcus sp. PCC7942 (radial asymmetry in the photosynthetic complexes). *Plant physiology,* 106**,** 251-262.

SHPILYOV, A. V., ZINCHENKO, V. V., SHESTAKOV, S. V., GRIMM, B. & LOKSTEIN, H. 2005. Inactivation of the geranylgeranyl reductase (ChlP) gene in the cyanobacterium Synechocystis sp. PCC 6803. *Biochimica et Biophysica Acta (BBA)-Bioenergetics,* 1706**,** 195-203.

SIEBERT, C. A., QIAN, P., FOTIADIS, D., ENGEL, A., HUNTER, C. N. & BULLOUGH, P. A. 2004. Molecular architecture of photosynthetic membranes in Rhodobacter sphaeroides: the role of PufX. *The EMBO journal,* 23**,** 690-700.

SIEGEL, R. M., CHAN, F. K.-M., ZACHARIAS, D. A., SWOFFORD, R., HOLMES, K. L., TSIEN, R. Y. & LENARDO, M. J. 2000. Measurement of molecular interactions in living cells by fluorescence resonance energy transfer between variants of the green fluorescent protein. *Science Signaling,* 2000**,** pl1-pl1.

SILVA, P. & NIXON, P. 2001. Identification of possible assembly and repair factors in photosystem two preparations of Synechocystis sp. PCC 6803: A new model for D1 turnover. *Science Access,* 3.

SILVA, P., THOMPSON, E., BAILEY, S., KRUSE, O., MULLINEAUX, C. W., ROBINSON, C., MANN, N. H. & NIXON, P. J. 2003. FtsH is involved in the early stages of repair of photosystem II in Synechocystis sp PCC 6803. *The Plant Cell,* 15**,** 2152-2164.

SINGHAL, G., RENGER, G., SOPORY, S. & IRRGANG, K. 2012. *Concepts in photobiology: photosynthesis and photomorphogenesis*, Springer Science & Business Media.

STEGER, U., ACHTERBERG, W., BLOK, K., BODE, H., FRENZ, W., GATHER, C., HANEKAMP, G., IMBODEN, D., JAHNKE, M. & KOST, M. 2005. *Sustainable development and innovation in the energy sector*, Springer Science & Business Media.

STERN, A. I., SCHIFF, J. A. & EPSTEIN, H. 1964. Studies of chloroplast development in Euglena. V. Pigment biosynthesis, photosynthetic oxygen evolution and carbon dioxide fixation during chloroplast development. *Plant physiology,* 39**,** 220.

STINGACIU, L.-R., O'NEILL, H., LIBERTON, M., URBAN, V. S., PAKRASI, H. B. & OHL, M. 2016. Revealing the dynamics of thylakoid membranes in living cyanobacterial cells. *Scientific reports,* 6**,** 1-6.

STRAŠKOVÁ, A., KNOPPOVÁ, J. & KOMENDA, J. 2018. Isolation of the cyanobacterial YFP-tagged photosystem I using GFP-Trap®. *Photosynthetica,* 56**,** 300-305.

STROEBEL, D., CHOQUET, Y., POPOT, J.-L. & PICOT, D. 2003. An atypical haem in the cytochrome b6f complex. *Nature,* 426**,** 413-418.

SUGITA, C., OGATA, K., SHIKATA, M., JIKUYA, H., TAKANO, J., FURUMICHI, M., KANEHISA, M., OMATA, T., SUGIURA, M. & SUGITA, M. 2007. Complete nucleotide sequence of the freshwater unicellular cyanobacterium Synechococcus elongatus PCC 6301 chromosome: gene content and organization. *Photosynthesis research,* 93**,** 55-67.

SUKENIK, A., ZOHARY, T. & PADISÁK, J. 2009. Cyanoprokaryota and other prokaryotic algae.

SUN, Y., WOLLMAN, A. J. M., HUANG, F., LEAKE, M. C. & LIU, L. N. 2019. Single-organelle quantification reveals the stoichiometric and structural variability of carboxysomes dependent on the environment. *Plant Cell,* 31**,** 1648-1664.

SZYSZKA-MROZ, B., PITTOCK, P., IVANOV, A. G., LAJOIE, G. & HÜNER, N. P. 2015. The Antarctic psychrophile Chlamydomonas sp. UWO 241 preferentially phosphorylates a photosystem I-cytochrome b6/f supercomplex. *Plant physiology,* 169**,** 717-736.

TAVANO, C. L. & DONOHUE, T. J. 2006. Development of the bacterial photosynthetic apparatus. *Current opinion in microbiology,* 9**,** 625-631.

TOPORIK, H., LI, J., WILLIAMS, D., CHIU, P.-L. & MAZOR, Y. 2019. The structure of the stress-induced photosystem I–IsiA antenna supercomplex. *Nature Structural & Molecular Biology,* 26**,** 443-449.

TORABI, S., UMATE, P., MANAVSKI, N., PLÖCHINGER, M., KLEINKNECHT, L., BOGIREDDI, H., HERRMANN, R. G., WANNER, G., SCHRÖDER, W. P. & MEURER, J. 2014. PsbN is required for assembly of the photosystem II reaction center in Nicotiana tabacum. *The Plant Cell,* 26**,** 1183-1199.

TRISSL, H.-W. & WILHELM, C. 1993. Why do thylakoid membranes from higher plants form grana stacks? *Trends in biochemical sciences,* 18**,** 415-419.

UMENA, Y., KAWAKAMI, K., SHEN, J.-R. & KAMIYA, N. 2011. Crystal structure of oxygen-evolving photosystem II at a resolution of 1.9 Å. *Nature,* 473**,** 55-60.

VAN DE MEENE, A. M., HOHMANN-MARRIOTT, M. F., VERMAAS, W. F. & ROBERSON, R. W. 2006. The three-dimensional structure of the cyanobacterium Synechocystis sp. PCC 6803. *Archives of microbiology,* 184**,** 259-270.

VAN STOKKUM, I. H., SPOELDER, H. J., BLOEMENDAL, M., VAN GRONDELLE, R. & GROEN, F. C. 1990. Estimation of protein secondary structure and error analysis from circular dichroism spectra. *Analytical biochemistry,* 191**,** 110-118.

VAN THOR, J., MULLINEAUX, C., MATTHIJS, H. & HELLINGWERF, K. 1998. Light harvesting and state transitions in cyanobacteria. *Botanica Acta,* 111**,** 430-443.

VEERMAN, J., BENTLEY, F. K., EATON-RYE, J. J., MULLINEAUX, C. W., VASIL'EV, S. & BRUCE, D. 2005. The PsbU subunit of photosystem II stabilizes energy transfer and primary photochemistry in the phycobilisome-photosystem II assembly of Synechocystis sp. PCC 6803. *Biochemistry,* 44**,** 16939-48.

VERMAAS, W. F., TIMLIN, J. A., JONES, H. D., SINCLAIR, M. B., NIEMAN, L. T., HAMAD, S. W., MELGAARD, D. K. & HAALAND, D. M. 2008. In vivo hyperspectral confocal fluorescence imaging to determine pigment localization and distribution in cyanobacterial cells. *Proceedings of the National Academy of Sciences,* 105**,** 4050-4055.

VINNEMEIER, J., KUNERT, A. & HAGEMANN, M. 1998. Transcriptional analysis of the isiAB operon in salt-stressed cells of the cyanobacterium Synechocystis sp. PCC 6803. *FEMS microbiology letters,* 169**,** 323-330.

VREDENBERG, W. & DUYSENS, L. 1965. Light-induced changes in absorbancy and fluorescence of chlorophyllous pigments associated with the pigment systems 1 and 2 in blue-green algae. *Biochimica et Biophysica Acta (BBA)-Biophysics including Photosynthesis,* 94**,** 355-370.

WANG, M., YOU, J., BEMIS, K. G., TEGELER, T. J. & BROWN, D. P. 2008a. Label-free mass spectrometry-based protein quantification technologies in proteomic analysis. *Briefings in functional genomics and proteomics,* 7**,** 329-339.

WANG, Q., JANTARO, S., LU, B., MAJEED, W., BAILEY, M. & HE, Q. 2008b. The high light-inducible polypeptides stabilize trimeric photosystem I complex under high light conditions in Synechocystis PCC 6803. *Plant physiology,* 147**,** 1239-1250.

WATANABE, M., SEMCHONOK, D. A., WEBBER-BIRUNGI, M. T., EHIRA, S., KONDO, K., NARIKAWA, R., OHMORI, M., BOEKEMA, E. J. & IKEUCHI, M. 2014. Attachment of phycobilisomes in an antenna–photosystem I supercomplex of cyanobacteria. *Proceedings of the National Academy of Sciences,* 111**,** 2512-2517.

WELKIE, D. G., LEE, B.-H. & SHERMAN, L. A. 2016. Altering the structure of carbohydrate storage granules in the cyanobacterium Synechocystis sp. strain

PCC 6803 through branching-enzyme truncations. *Journal of bacteriology,* 198**,** 701-710.

WHITMORE, L. & WALLACE, B. 2004. DICHROWEB, an online server for protein secondary structure analyses from circular dichroism spectroscopic data. *Nucleic acids research,* 32**,** W668-W673.

WHITMORE, L. & WALLACE, B. A. 2008. Protein secondary structure analyses from circular dichroism spectroscopy: methods and reference databases. *Biopolymers: Original Research on Biomolecules,* 89**,** 392-400.

WIETRZYNSKI, W., SCHAFFER, M., TEGUNOV, D., ALBERT, S., KANAZAWA, A., PLITZKO, J. M., BAUMEISTER, W. & ENGEL, B. D. 2019. Charting the native architecture of thylakoid membranes with single-molecule precision. *bioRxiv***,** 759001.

WILSON, A., BOULAY, C., WILDE, A., KERFELD, C. A. & KIRILOVSKY, D. 2007. Light-induced energy dissipation in iron-starved cyanobacteria: roles of OCP and IsiA proteins. *The Plant Cell,* 19**,** 656-672.

XIAO, Y., ZHU, Q., YANG, Y., WANG, W., KUANG, T., SHEN, J.-R. & HAN, G. 2020. Role of PsbV-Tyr137 in photosystem II studied by site-directed mutagenesis in the thermophilic cyanobacterium *Thermosynechococcus vulcanus*. *Photosynthesis Research,* 146**,** 41-54.

XIONG, J. & BAUER, C. E. 2002. Complex evolution of photosynthesis. *Annual review of plant biology,* 53**,** 503-521.

XIONG, J., FISCHER, W. M., INOUE, K., NAKAHARA, M. & BAUER, C. E. 2000. Molecular evidence for the early evolution of photosynthesis. *science,* 289**,** 1724-1730.

YANG, J., YAN, R., ROY, A., XU, D., POISSON, J. & ZHANG, Y. 2015. The I-TASSER Suite: protein structure and function prediction. *Nature methods,* 12**,** 7-8.

YOKONO, M., TAKABAYASHI, A., KISHIMOTO, J., FUJITA, T., IWAI, M., MURAKAMI, A., AKIMOTO, S. & TANAKA, A. 2019. The PSI–PSII megacomplex in green plants. *Plant and Cell Physiology,* 60**,** 1098-1108.

YU, J., LIBERTON, M., CLIFTEN, P. F., HEAD, R. D., JACOBS, J. M., SMITH, R. D., KOPPENAAL, D. W., BRAND, J. J. & PAKRASI, H. B. 2015a. Synechococcus elongatus UTEX 2973, a fast growing cyanobacterial chassis for biosynthesis using light and CO 2. *Scientific reports,* 5**,** 8132.

YU, J., LIBERTON, M., CLIFTEN, P. F., HEAD, R. D., JACOBS, J. M., SMITH, R. D., KOPPENAAL, D. W., BRAND, J. J. & PAKRASI, H. B. 2015b. Synechococcus elongatus UTEX 2973, a fast growing cyanobacterial chassis for biosynthesis using light and CO 2. *Scientific reports,* 5**,** 1-10.

YU, Y., YOU, L., LIU, D., HOLLINSHEAD, W., TANG, Y. J. & ZHANG, F. 2013. Development of Synechocystis sp. PCC 6803 as a phototrophic cell factory. *Marine drugs,* 11**,** 2894-2916.

ZAKRYŚ, B., MILANOWSKI, R. & KARNKOWSKA, A. 2017. Evolutionary origin of Euglena. *Euglena: biochemistry, cell and molecular biology***,** 3-17.

ZHANG, C., SHUAI, J., RAN, Z., ZHAO, J., WU, Z., LIAO, R., WU, J., MA, W. & LEI, M. 2020. Structural insights into NDH-1 mediated cyclic electron transfer. *Nature communications,* 11**,** 1-13.

ZHANG, P., BATTCHIKOVA, N., JANSEN, T., APPEL, J., OGAWA, T. & ARO, E.-M. 2004. Expression and functional roles of the two distinct NDH-1 complexes and the carbon acquisition complex NdhD3/NdhF3/CupA/Sll1735 in Synechocystis sp PCC 6803. *The Plant Cell,* 16**,** 3326-3340.

ZHANG, Y. 2008. I-TASSER server for protein 3D structure prediction. *BMC bioinformatics,* 9**,** 40.

ZHANG, Z., ZHAO, L.-S. & LIU, L.-N. 2021. Characterizing the supercomplex association of photosynthetic complexes in cyanobacteria. *Royal Society Open Science,* 8**,** 202142.

ZHAO, L.-S., HUOKKO, T., WILSON, S., SIMPSON, D. M., WANG, Q., RUBAN, A. V., MULLINEAUX, C. W., ZHANG, Y.-Z. & LIU, L.-N. 2020. Structural variability, coordination and adaptation of a native photosynthetic machinery. *Nature Plants,* 6**,** 869-882.

ZHENG, X.-Y. & O'SHEA, E. K. 2017. Cyanobacteria maintain constant protein concentration despite genome copy-number variation. *Cell reports,* 19**,** 497-504.

ZHOU, S., BECHNER, M. C., PLACE, M., CHURAS, C. P., PAPE, L., LEONG, S. A., RUNNHEIM, R., FORREST, D. K., GOLDSTEIN, S. & LIVNY, M. 2007. Validation of rice genome sequence by optical mapping. *BMC genomics,* 8**,** 1-18.

ZHU, X. G., ORT, D. R., WHITMARSH, J. & LONG, S. P. 2004. The slow reversibility of photosystem II thermal energy dissipation on transfer from high to low light may cause large losses in carbon gain by crop canopies: a theoretical analysis. *Journal of experimental botany,* 55**,** 1167-1175.

ZOUNI, A., WITT, H.-T., KERN, J., FROMME, P., KRAUSS, N., SAENGER, W. & ORTH, P. 2001. Crystal structure of photosystem II from Synechococcus elongatus at 3.8 Å resolution. *Nature,* 409**,** 739-743.